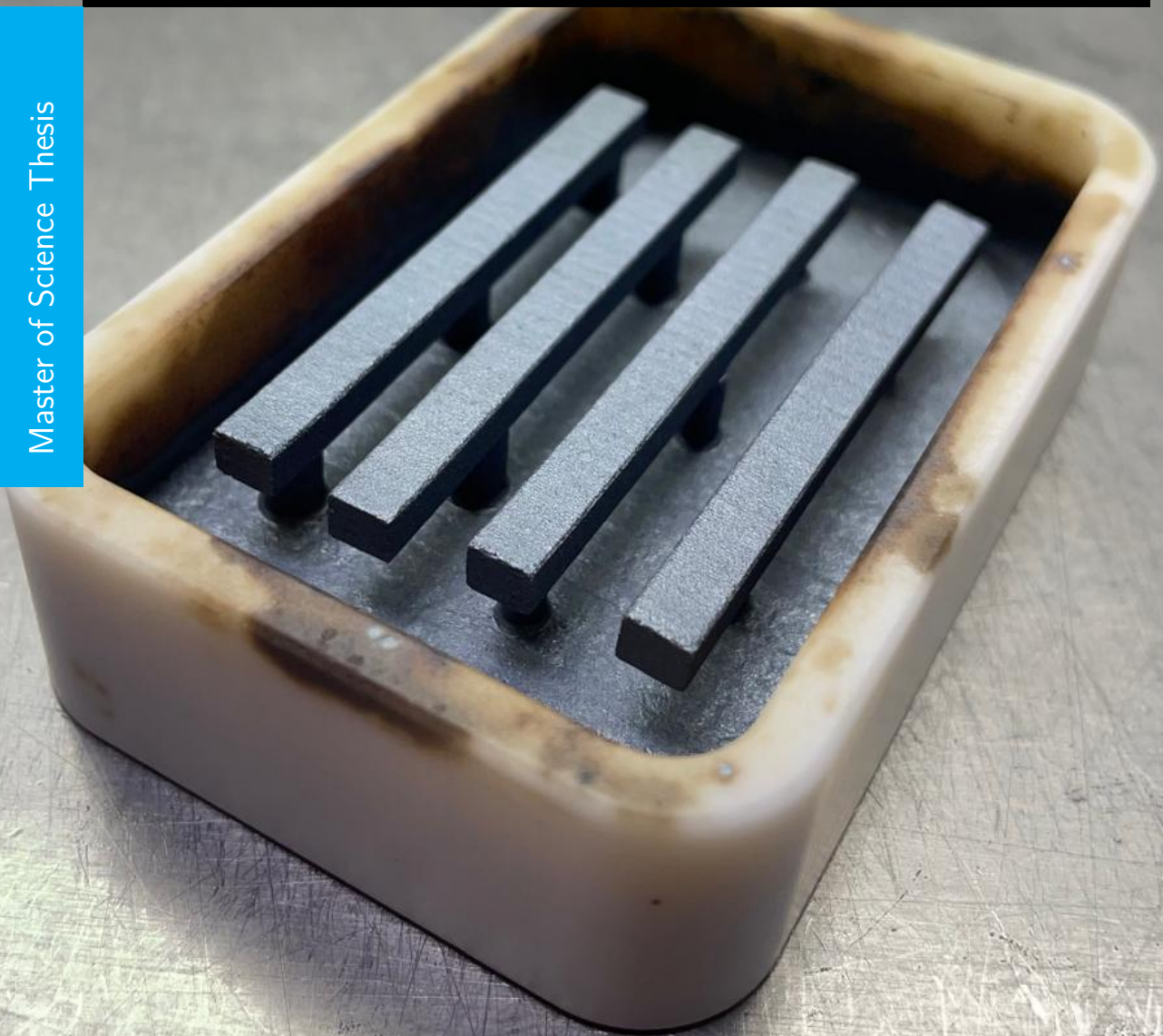


# Pressureless Infiltration of 3D-printed Alumina with Copper Oxide

Olaf Verbunt

Master of Science Thesis





# **Pressureless Infiltration of 3D-printed Alumina with Copper Oxide**

MASTER OF SCIENCE THESIS

For the degree of Master of Science in Materials Science and  
Engineering at Delft University of Technology

Olaf Verbunt

January 22, 2025

# ASML

The work in this thesis was supported by ASML. Their cooperation is hereby gratefully acknowledged.



Copyright © Materials Science and Engineering  
All rights reserved.



Materials Science  
and Engineering

DELFT UNIVERSITY OF TECHNOLOGY  
DEPARTMENT OF  
MATERIALS SCIENCE AND ENGINEERING

The undersigned hereby certify that they have read and recommend to the Faculty of  
Mechanical Engineering for acceptance a thesis entitled

PRESSURELESS INFILTRATION OF 3D-PRINTED ALUMINA WITH COPPER  
OXIDE

by

OLAF VERBUNT

in partial fulfillment of the requirements for the degree of  
MASTER OF SCIENCE MATERIALS SCIENCE AND ENGINEERING

Dated: January 22, 2025

Chair thesis committee:

---

Prof.dr.ir. Vera Popovich

Thesis committee:

---

Dr. Cristian Craus

---

Prof.dr.ir. Marcel Hermans

---

Dr. Omid Nejadseyfi



---

# Abstract

This study investigates the pressureless infiltration of 3D-printed alumina with copper oxide to produce ceramic composites suitable for ASML application. ASML's components demand high mechanical performance ceramics with complex shapes and low porosity. An effective method for producing large and complex shapes is powder bed binder jetting (PBBJ). A major challenge of this technique is achieving a low level of porosity. To address this challenge, pressureless infiltration has been employed as a post-processing method to reduce porosity.

Alumina porous structures with a relative bulk density of 59% were fabricated with PBBJ. An infiltration setup was designed and successfully tested on these alumina porous structures. Infiltrating the alumina with copper oxide in an oxygen-rich environment, resulted in a relative density of 85% and a flexural strength of 53.6 MPa. Reactions between alumina and copper oxide resulted in the consumption of up to 50% of the alumina, leading to the formation of ternary oxides (like  $\text{CuAlO}_2$ ). The ternary oxides accounted for approximately 70 wt.% of the composite. The formation of these ternary oxides significantly reduces the composite's mechanical properties, as it consumed the load bearing alumina. It was predicted that at 0% porosity, the theoretical minimal strength of this composite would be only 33% of the strength of alumina.

The feasibility of infiltration in nitrogen was explored through differential thermal analysis (DTA), thermogravimetric analysis (TGA), and X-ray diffraction (XRD) analyses. For these tests an equimolar powder mixture (consisting of  $\text{Al}_2\text{O}_3$  and  $\text{Cu}_2\text{O}$ ) was used. The results revealed 5 different phase transitions during the infiltration cycle. Even under the most optimal thermal infiltration conditions, 72 wt.% ternary oxide was formed.

Pressureless infiltration shows potential in improving the density of porous bodies created by PBBJ. The thermal infiltration cycle has to be improved in order to minimize the unwanted reactions between alumina and copper oxide. Using alternative materials for infiltration, may better meet ASML's requirements.

---

# Table of Contents

<b>Acknowledgements</b>	<b>v</b>
<b>1 Introduction</b>	<b>1</b>
1-1 Thesis scope and outline . . . . .	1
1-2 Background and motivation . . . . .	2
1-2-1 3D-printing technical ceramics . . . . .	2
1-2-2 User case ASML . . . . .	2
1-3 Problem statement and research objective . . . . .	3
<b>2 Theoretical Background</b>	<b>4</b>
2-1 Powder bed binder jetting . . . . .	4
2-2 Materials . . . . .	7
2-2-1 Alumina . . . . .	7
2-2-2 Copper oxide . . . . .	9
2-2-3 Composite . . . . .	14
2-3 Pressureless infiltration . . . . .	20
2-4 Research questions . . . . .	26
<b>3 Methodology</b>	<b>27</b>
3-1 Powder bed binder jetting . . . . .	28
3-2 Infiltration setup . . . . .	31
3-3 Characterization techniques . . . . .	35
<b>4 Results</b>	<b>39</b>
4-1 Powder bed binder jetting . . . . .	39
4-2 Infiltration in oxygen . . . . .	41
4-3 Infiltration simulation . . . . .	46
4-3-1 Thermogravimetric analysis (TGA) . . . . .	46
4-3-2 Differential thermal analysis (DTA) . . . . .	48
4-3-3 X-ray diffraction (XRD) . . . . .	55

---

<b>5 Discussion</b>	<b>56</b>
5-1 Effects of powder bed binder jetting and sintering conditions . . . . .	56
5-2 Effects of infiltration on densification and material properties . . . . .	57
5-3 Effects of infiltration environment . . . . .	61
5-4 ASML compliance . . . . .	64
<b>6 Conclusions</b>	<b>66</b>
<b>7 Recommendations</b>	<b>68</b>
<b>A Annex data results</b>	<b>69</b>
A-1 Powder bed binder jetting . . . . .	69
A-2 Infiltration in oxygen environment . . . . .	71
A-3 Infiltration in nitrogen environment . . . . .	72
<b>B Annex peak analysis</b>	<b>75</b>
B-1 Thermogravimetric analysis (TGA) . . . . .	76
B-2 Differential thermal analysis (DTA) . . . . .	77
<b>Bibliography</b>	<b>83</b>
<b>Glossary</b>	<b>89</b>
List of Acronyms . . . . .	89



---

# Acknowledgements

To begin with, I would like to express my gratitude to my supervisors, Professor Vera Popovich and Cristian Craus.

Vera, thank you for guiding me through the process of this master thesis. Your advice, your support and your intelligence came often at the right moment. I really appreciate that despite your busy schedule, you always made time to help me. Cristian, thank you for your active involvement in my project. I often felt like we were working together on this project, which made the process feel both collaborative and rewarding. Hans Brouwer, thank you for always taking the time to help me. Your unmatched technical knowledge was irreplaceable during my thesis.

To my roommates at Huize Tommy (d'n Haai, d'n Sloth, d'n Mark and d'n Krab) thank you for all your support. A special thanks to my friend d'n Krab (a.k.a. Ons Stefke). Although this might be a bit one-sided, you were my favorite project member during all of my bachelor projects.

To my family, thank you for always being there for me. Mom, you're an underrated academic powerhouse. Dad, your renowned PhD thesis: "*The Glutathione Redox Cycle in the Reper-fused Rat Heart*" remains a constant source of inspiration [A]. And to my brother and sister, thank you for your mental support.

I also want to thank my beautiful girlfriend, Lale, for all your support. Your turn to graduate is coming next year. I have no doubt that you will do excellent.

[A]: Robert-Jan Albert Maria Verbunt. The Glutathione Redox Cycle in the Reper-fused Rat Heart. *Rijksuni-versiteit Leiden*, 1996.

Delft, University of Technology  
January 22, 2025

Olaf Verbunt

Master of Science Thesis

Olaf Verbunt



---

# Chapter 1

---

## Introduction

### 1-1 Thesis scope and outline

This thesis investigates the pressureless infiltration of copper oxide into alumina to develop a high density (>99%) ceramic composite material. The focus is on understanding the infiltration process and phase transformations that took place during infiltration. Porous alumina structures were produced exclusively using powder bed binder jetting (PBBJ), with no other additive manufacturing methods explored. The printing was done using alumina powder and sintering was conducted using a vacuum graphite furnace. Pressurized sintering, did not give any significant densification. The scope also centers on the requirements for ASML applications. Experiments were performed in oxygen-rich and full nitrogen environments to assess their effects on infiltration and phase transformations. Characterization methods included microstructural characterization, thermogravimetric analysis (TGA), differential thermal analysis (DTA), X-ray diffraction (XRD), scanning electron microscope (SEM) and 3-point bending tests. Broader economic analysis and real-world testing (like 3D-printing the ASML applications) are excluded.

The introduction provides the background and motivation for this research. This includes an introduction to 3D-printing high-density technical ceramics. The user case of ASML is as well introduced. Due to confidentiality, details about the ASML use case could not be shared and are therefore referred to as the 'ASML application'. The technical background elaborates on the 3D-printing technique PBBJ. It focuses on the materials used (alumina and copper oxide) and their interaction in composite form, focusing on both mechanical and chemical aspects. This chapter also introduces pressureless infiltration and concludes with the research questions. The methodology includes a block diagram, where the experimental process is detailed with each step individually. The results section begins with the characterization of the 3D-printed PBBJ alumina porous structure, followed by infiltration and the peaks observed during experiments in nitrogen using DTA and TGA. In the discussion, the reactions are assigned to the observed peaks and the findings are analyzed. The conclusion addresses the research questions, while the recommendations outline potential directions for future work.

## 1-2 Background and motivation

### 1-2-1 3D-printing technical ceramics

Technical ceramics are ceramic materials that are used for demanding environments where high performance is essential. These materials often have outstanding mechanical, thermal and chemical properties [8, 59]. Some technical ceramics have excellent hardness and wear resistance make them ideal for tools and machines under heavy use, such as cutting tools. The specific stiffness provided by some technical ceramics provides added benefits in mechanical applications [19]. Electrical characteristics could also add value, with for example alumina being used as an insulating material in electronics [47]. However, producing technical ceramics with complex shapes has long been challenging due to the difficulty of machining these hard and brittle materials [8].

3D-printing methods are changing this by enabling the manufacturing of high-density ceramics with complex geometries. The 3D-printing techniques minimizes the need for machining and post-processing. It can also reduce the production time and costs [8]. With this reason, 3D-printing as a technique for creating ceramic components is becoming a promising tool.

Technical ceramics are becoming more important in the semiconductor industry. The stability of these technical ceramics under heat and chemicals is crucial. Higher accelerations are required in chip manufacturing machines, with the rise in chip production. To meet these demands, materials like technical ceramics, known for their high specific stiffness, could offer an appealing alternative to traditional materials. Their role in high-tech applications highlights their importance in modern engineering [8].

### 1-2-2 User case ASML

The user case of this master thesis is provided by ASML. ASML plays a critical role in the semiconductor industry by providing advanced photolithography systems used in chip manufacturing. These machines are essential for creating complex patterns on silicon wafers. ASML specializes in both deep ultraviolet (DUV) and extreme ultraviolet (EUV) lithography systems. The EUV technology enables the production of the most advanced semiconductor designs [36].

ASML's innovations have played a major role in following the trend of the Moore's Law, which predicts the steady increase in the number of transistors on a chip. For ASML it's not just about the number of transistors, the production speed measured in wafers per hour, is equally important. The machines need to deliver high wafer outputs to remain competitive, allowing customers of the ASML machines to recover their investments. To achieve this, the machines must scan silicon wafers faster, requiring higher acceleration. At the same time, downtime is costly, so every component must perform reliably without failure.

Higher acceleration rates increase mechanical stress on machine components. To address this, ASML is exploring technical ceramics as potential replacements for some metal parts. Ceramics offer high specific stiffness, stable thermal properties such as good conductivity, low expansion and chemical resistance. This makes ceramics suitable for specific application areas in ASML machines.

One critical requirement for the ASML application are the internal cooling channels to maintain a constant temperature. These channels are designed with small tolerances. For example, the walls of these internal cooling channels are  $<1$  mm. These channels must be leak-proof, handling fluids without failure. Leak tightness is determined by the viscosity of the fluid, the pressure of the fluid, the pore size, and the pore connectivity. Since the ASML application is located in a critical environment, it is critical to avoid any leakage at all costs. Therefore, it is assumed that the ASML application must have a very low level of porosity to guarantee safety, below 1%. This value is an assumption and further calculations are required to determine the exact threshold. Achieving such a low level of porosity poses a significant challenge for PBBJ [9].

## 1-3 Problem statement and research objective

### Problem statement

There is a demand for technical ceramics with complex geometries and low porosity ( $<1\%$ ). Standard manufacturing methods are unable to meet these requirements due to their limitations in producing complex shapes. While PBBJ is capable of fabricating complex shapes, achieving ceramics with low porosity remains a significant challenge.

### Research objective

Investigate the effect of infiltration on density and properties of porous ceramic structures produced by PBBJ.

# Theoretical Background

The theoretical background explains the main concepts needed to carry out the research. It begins with an explanation of powder bed binder jetting, starting from the powder and ending with the sintering process.

Next, the materials used in this research are introduced, namely alumina and copper oxide. Their mechanical and chemical interactions are further detailed in the section about composite.

Finally, the principle of pressureless infiltration is explained. Knowing this theory is important for successfully infiltrating the porous structures.

### 2-1 Powder bed binder jetting

powder bed binder jetting (PBBJ) is a additive manufacturing technique that is used in this study for creating 3D objects. With this technique, a liquid binder is selectively deposited onto layers of powder to form a solid structure. Compared to other additive manufacturing methods, PBBJ offers two key advantages. It can produce faster and can handle larger build volumes [9]. These advantages are beneficial for creating complex geometries on a larger scale. A wide range of materials can be printed with PBBJ, including ceramics, metals, and composites. However, achieving low porosity and high mechanical strength remains a challenge for working with ceramics [9]. Careful optimization of process parameters and post-processing techniques is required.

The PBBJ process begins with the preparation of fine powder. This powder is spread in thin layers over a build plate. A print head deposits the liquid binder according to a pre-defined 3D model. The binder adheres the powder particles to form the green part. This layer-by-layer process continues until the entire object is printed. Post-processing steps, such as curing, depowdering, and sintering, are then applied. These steps are needed in order to create a solid 3D-object. A schematic of the process is shown in Figure 2-1.

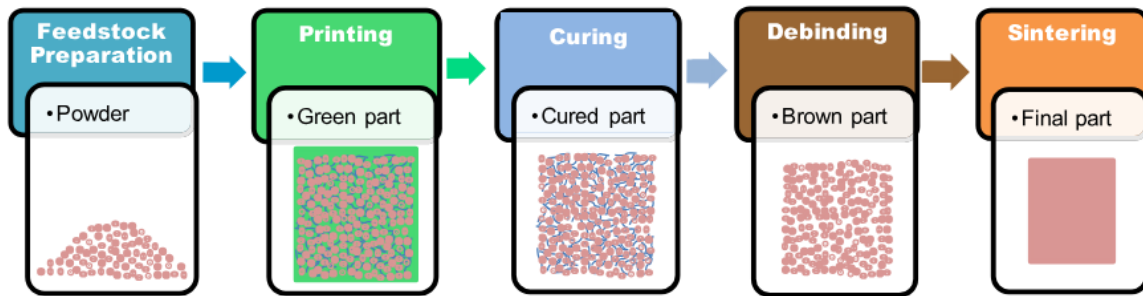


**Figure 2-1:** Major steps in powder bed binder jetting [9]

A typical PBBJ system consists of several key components, as shown in Figure 2-2. The build plate provides the foundation for layer-by-layer construction. The recoater and roller ensure even distribution and compaction of the powder layers. The print head and binder cartridge precisely deposit the liquid binder onto the powder bed. A heater assists in binder evaporation after each layer. This improves layer adhesion and prepares the surface for the next layer.

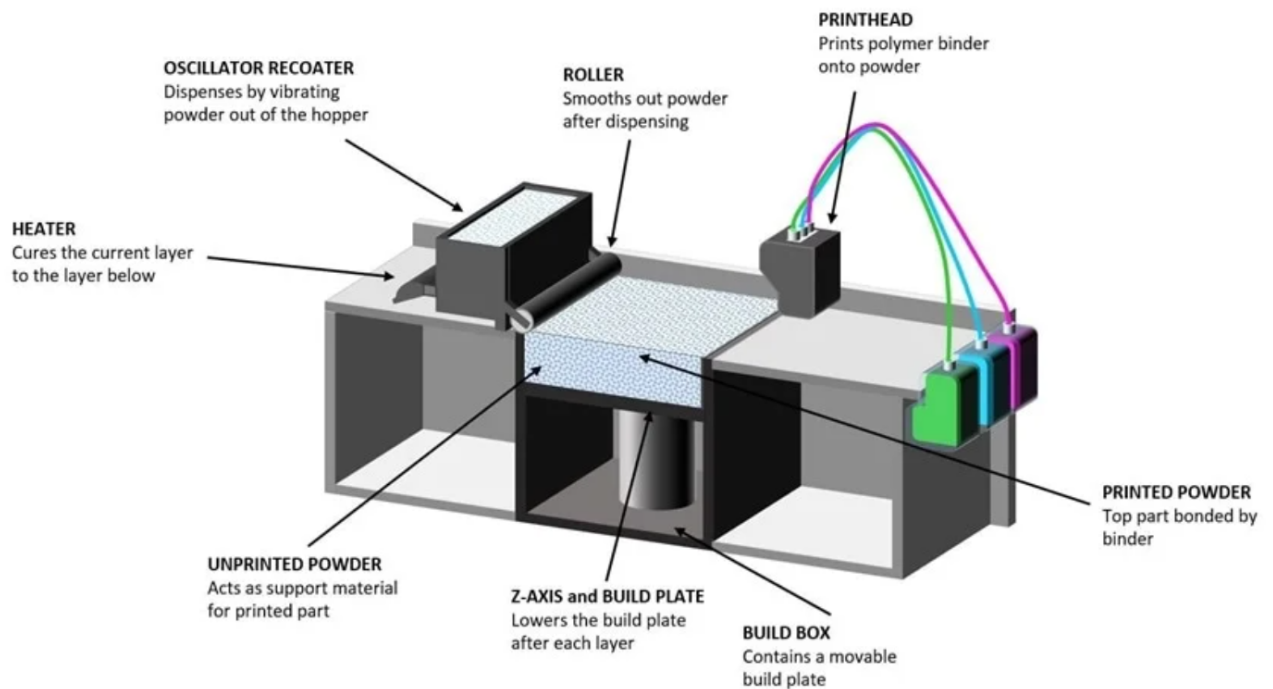


**Figure 2-2:** Major components in powder bed binder jetting [12]

After printing, the green part undergoes post-processing. Curing solidifies the binder, enhancing structural integrity needed for depowdering. Depowdering removes unbound powder, which can be recycled for future use. The binder is then removed through thermal decomposition, also known as debinding. This leaves the brown part. Finally, sintering densifies the brown part by promoting particle bonding through heat. This process improves the mechanical integrity of the 3D-printed part and reduces porosity.

The quality of parts produced by PBBJ depends on several key process parameters. Binder properties, such as viscosity and droplet size, are crucial for effective particle bonding [63]. Layer thickness plays an important role in surface finish and resolution. The optimal layer thickness is typically based on particle size [9]. Binder saturation represents the volume of binder relative to the air space in the powder bed. Proper control of saturation ensures structural integrity and dimensional accuracy [9].

Although PBBJ has significant advantages in producing complex geometries, it faces challenges in achieving low porosity working with ceramics. Different densification techniques could be used in order to improve the relative density of the as printed and sintered objects. These densification techniques include the use of nanoparticles in the binder, powder granulation, sintering additives, liquid slurry infiltration and liquid phase infiltration [9]. In this research, liquid phase infiltration will be used as the post-processing method to improve the relative density.

### Density and porosity

In PBBJ various terminologies are used to define different types of densities. These include densities associated with the packing state of the powder, densities of the part at various stages of the process and densities that account for the presence or absence of pores. Similarly, different terms are used to describe porosity. Table 2-1 provides a summary of these density and porosity terminologies, based on the literature review by W. Du et al. [9].

The terminology of open and closed pores are mentioned in Table 2-1. Open pores are permeable from the surface, while closed pores are totally included into the bulk. In Figure 2-3, a schematic cross view can be seen that shows the difference between open and closed pores.

**Table 2-1:** Density and porosity terminology [9]

Terminology	Definition
<b>Powder density in different packing states</b>	
Apparent density	Density of freely settled powder
Tap density	Density of powder after standard tapping process
Powder bed density	Density of powder that is spread on the build platform
<b>Part density after different process stages</b>	
Green density	Density after printing and curing
Brown density	Density after debinding
Sintered density	Density after sintering
<b>Part density and porosity when different pores are included</b>	
Apparent solid density	Mass per unit apparent solid volume (total volume of solid material and closed pores)
Bulk density	Mass per unit bulk volume (total volume including open and closed pores)
Apparent porosity	Volume percentage of open pores in the bulk material
Closed porosity	Volume percentage of closed pores in the bulk material
Bulk porosity	The sum of apparent and closed porosity

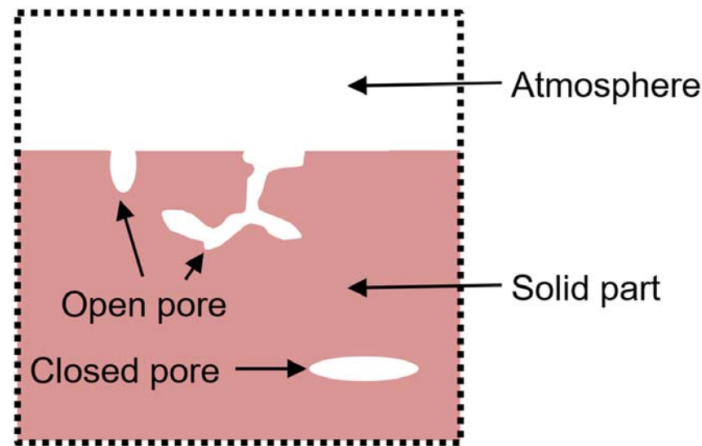


Figure 2-3: Schematic view open and closed pores in a cross section view [9]

## 2-2 Materials

This research focuses on two main materials: alumina and copper oxide. Alumina is the material used to create the porous structure with the use of PBBJ. Copper oxide is the infiltrated material that goes inside the porous structure. This section begins by focusing on the properties of alumina. Next, the properties of copper oxide are examined, with special attention given to how it behaves during oxidation and reduction under different oxygen partial pressures. Lastly, the composite section is divided into two parts: mechanical and chemical. The mechanical part examines how the mechanical properties of the composite changes with varying concentrations of alumina and copper oxide. The chemical part investigates the interactions between alumina and copper oxide at different temperatures and environments.

### 2-2-1 Alumina

Alumina ( $Al_2O_3$ ) is a ceramic material, that has multiple useful material properties. These material properties include mechanical, chemical, thermal and electrical properties. It has a high melting point of  $2,054^\circ C$  and is very stable [53]. Alumina exists in multiple phases, with the  $\alpha$ -phase being the most commonly used for mechanical applications due to its superior hardness and strength [38]. Therefore, this section will focus exclusively on  $\alpha$ -alumina.

#### Mechanical properties

Alumina is renowned for its hardness, stiffness, strength and relatively low density [38]. This results in a high specific stiffness and high specific strength, which could be useful material properties for material selection. However, there are also some downsides of using alumina relating to the mechanical properties. An example of this, is the relatively low fracture toughness.

Table 2-2 presents the mechanical properties of 99.5% purity  $\alpha$ -alumina with a density greater than 99.9%, derived from Granta EduPack 2021 [54]. From a PBBJ perspective, these material properties are on the higher end, as achieving near-zero porosity with binder jetting is

**Table 2-2:** Material properties 99.5% purity  $\alpha$ -alumina [54]

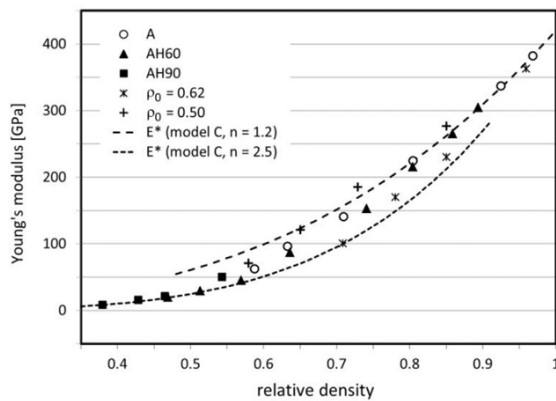
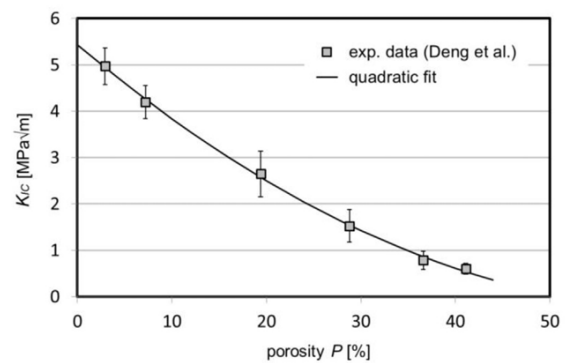
Material property	Value	[Unit]
Young's modulus	363 - 381	GPa
Tensile strength	252 - 265	MPa
Elongation	0.07	% strain
Compressive strength	2.52 - 2.63	GPa
Flexural strength	302 - 318	MPa
Poisson's ratio	0.21 - 0.27	-
Hardness Vickers	1480 - 1720	HV
Fracture toughness	3.8 - 4.2	$\text{MPa}\sqrt{m}$

**Table 2-3:** Porosity vs. strength of  $\alpha$ -alumina [53]

Porosity (%)	Flexural strength (MPa)
0	269
10	172
20	110
30	76
40	55
50	47

very challenging [9]. Therefore, a study that correlates flexural strength with porosity provides more relevant insights, as shown in Table 2-3 [53]. The values in Table 2-3 align with the findings of A. K. Mohan, a predecessor of this study, where a flexural strength of 59.5 MPa was achieved with a porosity of 33.1% [34]. For an optimal strength, it can be derived from the table that a as low as possible porosity is to be desired.

The Young's modulus is also heavily dependent on the porosity. In Figure 2-4, the relation of alumina can be seen between the Young's modulus and the relative density [18]. In the graph there are two lines seen for two different models that describe the relation between relative density and Young's modulus (namely model C,  $n = 1.2$  &  $n=2.5$ ). The highest Young's modulus can be achieved with the highest relative density i.e. lowest porosity. The values of the figure correspond again with the studies of A. K. Mohan, where they achieved a Young's modulus of 77.3 GPa with a relative density of 66.9% [34].

**Figure 2-4:** Relation between Young's modulus and relative density for alumina [18]**Figure 2-5:** Relation between fracture toughness and porosity for alumina [18]

The fracture toughness increases with a decreasing porosity i.e. increasing relative density. This can be seen in Figure 2-5 [18]. In order to construct the diagram, an extrapolation has been made to determine the fracture toughness for a porosity of 0%.

### Structure of $\alpha$ -alumina

Alumina can have multiple phases, namely stable phases and metastable phases. However the only stable phase of  $\text{Al}_2\text{O}_3$  under room temperature and atmospheric pressure is corundum ( $\alpha$ -phase). The corundum structure is shown in Figure 2-6. It consists of oxygen ions in a slightly distorted close-packed hexagonal (rhombohedral) lattice, space group  $R\bar{3}c$ . The aluminum ions occupy two-thirds of the octahedral sites in the oxygen lattice. The lattice parameters for corundum are  $a = 4.758 \text{ \AA}$  and  $c = 12.991 \text{ \AA}$  [49].

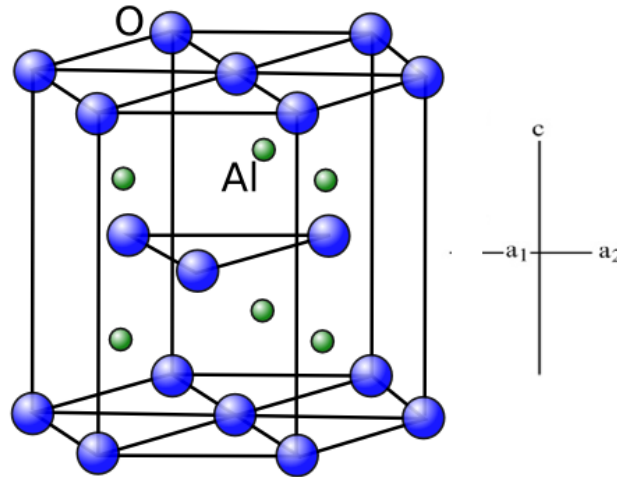


**Figure 2-6:** The structure of  $\alpha$ -alumina, also known as corundum [49]

### 2-2-2 Copper oxide

This section offers a brief overview of the oxidation states of copper oxide, its stability under different oxygen partial pressures, its mechanical properties, surface tension, viscosity and contact angle on alumina. The surface tension, viscosity and contact angle are key factors required for further calculations related to the wettability of copper oxide on alumina.

#### Oxidation states

The copper-oxygen (Cu-O) system is known for the existence of two main oxides: cuprous oxide ( $\text{Cu}_2\text{O}$ ) and cupric oxide ( $\text{CuO}$ ). The phases exist at the different oxygen pressures and different temperatures. This can be seen in Figure 2-7.  $\text{Cu}_2\text{O}$  tends to remain stable in reducing conditions, while  $\text{CuO}$  is more commonly formed in oxidizing environments [13].

The oxidation of  $\text{Cu}_2\text{O}$  to  $\text{CuO}$  in an oxygen rich environment takes place in the temperature domain of 300 - 700 °C. The oxidation reaction is described by equation 2-1 [3, 15].



This reaction occurs as  $\text{Cu}_2\text{O}$ , in which copper is in the +1 oxidation state, is converted into  $\text{CuO}$ , where copper is in the +2 oxidation state [3].

In air, CuO (cupric) transforms back to Cu<sub>2</sub>O (cuprous) at temperatures above 1020 °C [56, 21], though some sources indicate that this transformation occurs around 1000 °C [3]. This redox process for copper, when going from CuO to Cu<sub>2</sub>O, involves the reduction of copper from the +2 to the +1 oxidation state. This can be seen in equation 2-2 and in equation 2-3.



The oxidation of Cu<sub>2</sub>O to CuO is an exothermic process, releasing heat as Cu<sub>2</sub>O is oxidized. Conversely, the reduction of CuO to Cu<sub>2</sub>O is endothermic, requiring an input of energy [3].

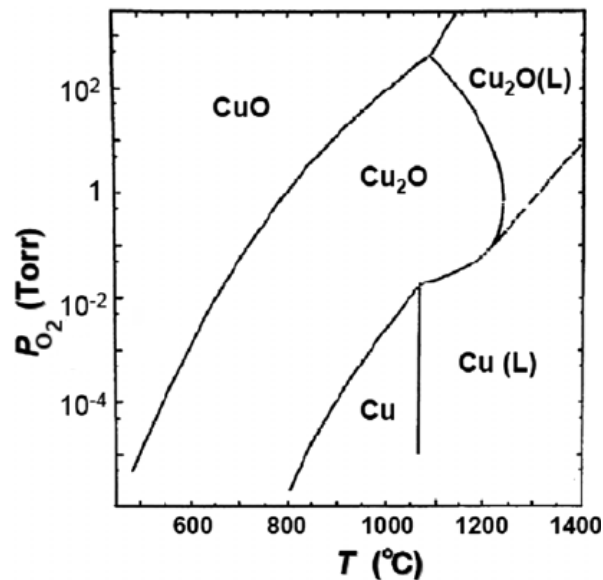


**Figure 2-7:** Phase diagram of the copper–oxygen system, showing oxygen partial pressure as a function of temperature [2]

### Mechanical properties

In this study, copper oxide is used as an infiltrated phase in the porous alumina structure made by PBBJ. Alumina is the main load-bearing part of the composite, so the mechanical properties of copper oxide are less important but not completely irrelevant. They still play a role in the final mechanical performance of the composite. In Table 2-4, the density and Young's modulus of the copper oxides are shown. It is clear that, in terms of specific stiffness ( $\frac{E}{\rho}$ ), copper oxide does not perform as well as alumina.

### Surface tension

The surface tension of copper oxide plays a key role in determining its wetting behavior. The infiltration of copper oxide into alumina in this research occurs at temperatures ranging from 1230°C to 1300°C (see section 4). Direct measurements of surface tension for copper oxide at these temperatures are not readily available in the literature.

Research by C. Nexhip et al. provided a formula to calculate the surface tension of Cu-O systems at 1130°C under varying oxygen partial pressures ( $pO_2$ ) (see equation 2-4) [35]. As detailed earlier, CuO decomposes to Cu<sub>2</sub>O above 1020°C, therefore this formula specifically calculates the surface tension of Cu<sub>2</sub>O.

$$\gamma = 1251 - 77.5 \cdot \ln \left( 1 + (2.79 \times 10^5 \cdot \sqrt{pO_2}) \right) \text{ [mN/m]} \quad (2-4)$$

This formula provides the surface tension at 1130°C. To estimate the surface tension at the infiltration temperature of 1250°C, extrapolation of the data is necessary. The method for extrapolation is outlined in equation 2-5 [35].

$$\gamma(T) = \gamma_0 - k(T - T_0) \quad (2-5)$$

Here,  $k$  represents the temperature coefficient, which was defined by C. Nexhip et al. to range from 0.2 to 0.3 mN/(m · K) [35]. Next, the surface tension is calculated at 1250°C and at  $pO_2 = 0.2$  (see equation 2-6 and 2-7).

$$\gamma = 1251 - 77.5 \cdot \ln \left( 1 + (2.79 \times 10^5 \cdot \sqrt{0.2}) \right) \quad (2-6)$$

$$\gamma = 1251 - 909.4 = 341.6 \text{ mN/m} \quad (2-7)$$

Thus, the surface tension  $\gamma$  at  $pO_2 = 0.2$  atm is approximately 341.6 mN/m at 1130°C.

The surface tension 1250°C can be calculated with the temperature coefficient. For the following calculation, the average value of  $k$ , which is 0.25 mN/(m · K) defined by C. Nexhip et al. [35], will be used. Using this value, the surface tension can be determined through the following extrapolation (see equation 2-8).

$$\gamma(1523 \text{ K}) = 341.6 - 0.25 \times (1523 - 1400) = 311 \text{ mN/m} \quad (2-8)$$

## Viscosity

In the research by M. Chen et al., the viscosity of a  $\text{Cu}_2\text{O}$  system was studied within the temperature range of 1230 to 1330 °C [5]. This aligns with the conditions of the process that is interesting for this research (1250 to 1300 °C). Their study applied the Modified Urbain model to calculate the viscosity, and the results were compared with experimental data. The data showed a strong correlation with the model's predictions. This can be seen in Figure 2-8.

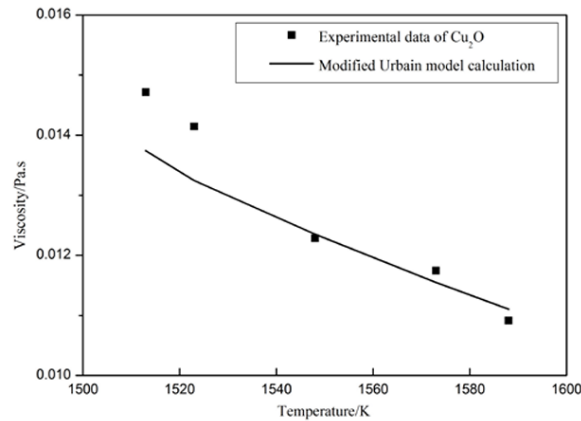


**Figure 2-8:** Comparison of experimental data (symbols) and calculated viscosities (line) for the  $\text{Cu}_2\text{O}$  system in the temperature range of 1240 to 1315 °C [5]

The tests by M. Chen et al. were done in an argon atmosphere, which could affect the viscosity values compared to other gases [5]. The exact impact on the viscosity of a different environment is unknown. In this research, it is assumed that the results in argon are close enough to the environment of this research where different concentrations of oxygen and nitrogen are combined.

### Contact angle

To calculate the contact angle  $\theta$  of  $\text{Cu}_2\text{O}$  on alumina, the Young's equation can be used in equation 2-9 [25]:

$$\cos \theta = \frac{\gamma_{SV} - \gamma_{SL}}{\gamma_{LV}} \quad (2-9)$$

where:

- $\gamma_{SV}$  is the surface tension of the solid (alumina) in a vacuum.
- $\gamma_{SL}$  is the surface tension at the solid-liquid interface (between alumina and  $\text{Cu}_2\text{O}$ ).
- $\gamma_{LV}$  is the surface tension of the liquid ( $\text{Cu}_2\text{O}$ ) in contact with its vapor.

Determining the contact angle between copper oxide and alumina at 1250 - 1300°C presents several challenges. One reason is the lack of data on the three surface tensions at various oxygen partial pressures at 1250 - 1300°C. Additionally, reactions occur at the phase boundary at this temperature, with ternary oxides beginning to form at temperatures above 750°C [3], which further complicates the analysis.

As stated before, the specific contact angle of liquid copper oxide on alumina at 1250-1300°C has not been widely documented in the literature. Therefore, an assumption is necessary. Metallic copper has a poor wetting angle on alumina, with contact angles greater than 90° [57]. Adding oxygen to the copper melt significantly reduces its contact angle with alumina. N.A. Travitzky et al. measured wetting angles of 72°, 57°, 44°, and 32° for copper-oxygen alloys with 0.8, 1.6, 2.4, and 3.2 wt.% oxygen at 1300°C [57]. In this master thesis,  $\text{Cu}_2\text{O}$  is used, which contains 11.2 wt.% oxygen. Considering that the wetting angle decreases as oxygen content increases, it is assumed that the contact angle for 100%  $\text{Cu}_2\text{O}$  would be around 32° (or might be even lower). This assumption is verified by Figure 2-9, where in a broken alumina crucible containing solidified  $\text{Cu}_2\text{O}$ , the contact angle was indicated and determined to be around 25°.

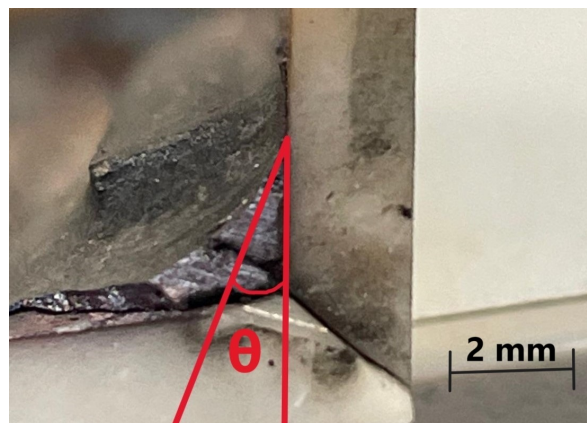


**Figure 2-9:** Broken alumina crucible with wetted and solidified  $\text{Cu}_2\text{O}$ . The contact angle, marked by red lines, is approximately 25°

### 2-2-3 Composite

In this section, the interaction between copper oxide and alumina in the composite will be elaborated. The section starts with the chemical perspective. This is followed by the mechanical analysis. The chemical analysis will focus on the reactions that occur between copper oxide and alumina at elevated temperatures. The mechanical analysis examines how the Young's modulus varies with different concentrations of copper oxide.

#### Chemical

Alumina and copper oxide react at elevated temperatures. This can be seen in the phase diagram of  $\text{Al}_2\text{O}_3$  and  $\text{Cu}_2\text{O}$  with varying concentrations (see Figure 2-10). The phase diagram was derived from experiments conducted in an argon atmosphere [6]. The diagram highlights the formation of various phases, including metallic copper and the ternary oxide  $\text{CuAlO}_2$  (delafossite). From the diagram, it can be derived that these phases begin to form from approximately 900 °C [6].

Additionally, the same phase diagram has been reconstructed for experiments carried out in an air environment, as depicted in Figure 2-11 [17]. In this scenario, two ternary oxides, namely  $\text{CuAlO}_2$  (delafossite) and  $\text{CuAl}_2\text{O}_4$  (spinel), can be observed. The spinel phase emerges at temperatures around 600 °C. With increasing temperature it transitions into  $\text{CuAlO}_2$  (delafossite). On the right side of the phase diagram, an eutectic point is noticeable near 1130 °C, marking the temperature where liquid  $\text{CuAlO}_2$  and  $\text{Cu}_2\text{O}$  solidify into a solid phase [17]. It is unlikely that a spinel phase will be present in the infiltrated bending bar samples, as copper oxide is infiltrated at a temperature of 1230 °C. At this temperature, delafossite ( $\text{CuAlO}_2$ ) forms instead of the spinel phase ( $\text{CuAl}_2\text{O}_4$ ). Although the delafossite can oxidize during the cooling process.

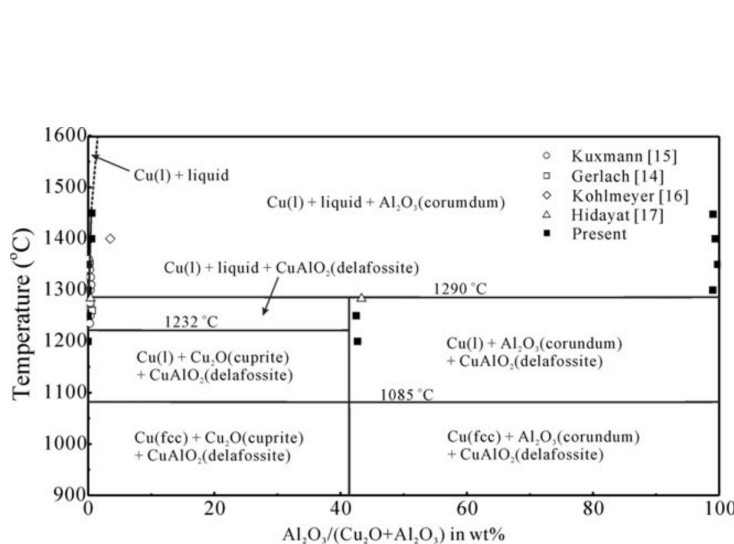


**Figure 2-10:** The phase diagram of the  $\text{Cu}_2\text{O}$ – $\text{Al}_2\text{O}_3$  system in equilibrium with metallic copper in argon [6]

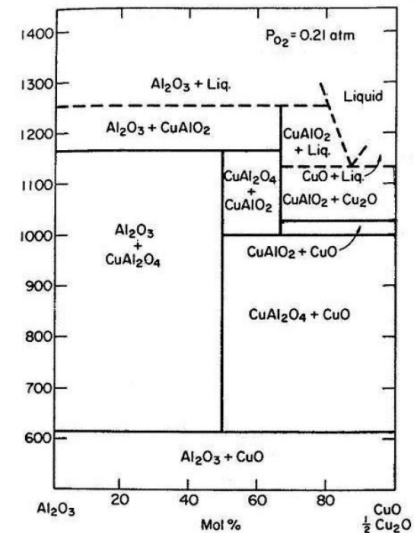


**Figure 2-11:** The projected isobaric phase diagram for the  $\text{CuO}$ – $\text{Cu}_2\text{O}$ – $\text{Al}_2\text{O}_3$  system at  $p_{\text{O}_2} = 0.21$  atm [17]

A.P. Amrute et al. conducted an in situ X-ray diffraction (XRD) analysis using an equimolar powder mixture of  $\text{Al}_2\text{O}_3$  and  $\text{Cu}_2\text{O}$  at various temperatures (see Figure 2-12 for air and Figure 2-13 for  $\text{N}_2$ ) [3]. This analysis reveals that ternary oxide formation begins at higher temperatures in nitrogen ( $1000^\circ\text{C}$ ) compared to oxygen ( $750^\circ\text{C}$ ), as shown in the figures. The results are not fully comparable, as the study utilized  $\gamma$ -alumina, whereas this study employs  $\alpha$ -alumina. Since  $\gamma$ -alumina transitions to  $\alpha$ -alumina around  $850^\circ\text{C}$ , the data is more relevant above this temperature [3].

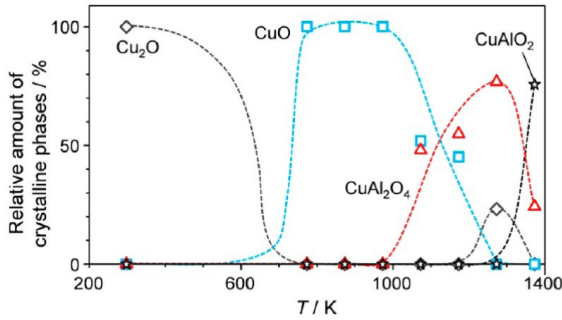


**Figure 2-12:** Evolution of the crystalline phases during the synthesis of  $\text{CuAlO}_2$  in air as determined from the in situ XRD analysis based on equimolar  $\text{Cu}_2\text{O} + \text{Al}_2\text{O}_3$  mixtures [3]

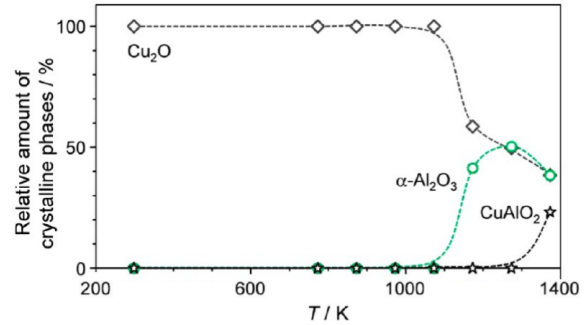


**Figure 2-13:** Evolution of the crystalline phases during the synthesis of  $\text{CuAlO}_2$  in  $\text{N}_2$  as determined from the in situ XRD analysis based on equimolar  $\text{Cu}_2\text{O} + \text{Al}_2\text{O}_3$  mixtures [3]

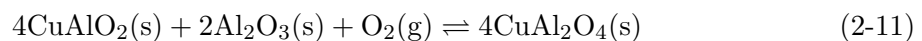
#### Formation of the spinel $\text{CuAl}_2\text{O}_4$

The spinel ( $\text{CuAl}_2\text{O}_4$ ) is created by a reaction between cupric oxide ( $\text{CuO}$ ) and alumina ( $\text{Al}_2\text{O}_3$ ). This reaction takes place after  $\text{Cu}_2\text{O}$  is oxidized to  $\text{CuO}$ , as shown in reaction 2-1. Once  $\text{CuO}$  is formed, it reacts with alumina between the temperatures of  $700^\circ\text{C}$  and  $1000^\circ\text{C}$ , leading to the formation of  $\text{CuAl}_2\text{O}_4$ , as described in equation 2-10 [3]. In Figure 2-11, it can be seen that the reaction might take place at even lower temperatures ( $600^\circ\text{C}$ ) [17]. The reaction is exothermic, as indicated by its negative formation enthalpy [4].



The oxidation of  $\text{Cu}_2\text{O}$  to  $\text{CuO}$  does not occur in an inert environment, due to the absence of oxygen. Without this oxidation step,  $\text{Cu}_2\text{O}$  remains stable in its +1 oxidation state, preventing the formation of  $\text{CuO}$ . As a result, the subsequent reaction between  $\text{CuO}$  and  $\text{Al}_2\text{O}_3$  cannot take place. Therefore, oxygen is needed in order to let the formation of the spinel happen [3].

A spinel ( $\text{CuAl}_2\text{O}_4$ ) can also form when a delafossite ( $\text{CuAlO}_2$ ) oxidizes. This oxidation reaction is shown in reaction 2-11 [15] (with an excess amount of  $\text{Al}_2\text{O}_3$ ). The equilibrium for this reaction is reached when the partial pressure of  $\text{O}_2$  ( $P_{\text{O}_2}$ ) is 0.014 bar at  $900^\circ\text{C}$ . If an excess amount of  $\text{CuO}$  is present, the oxidation reaction follows reaction 2-12. The equilibrium for this reaction is reached when  $P_{\text{O}_2}$  is 0.048 bar at  $900^\circ\text{C}$  [15].



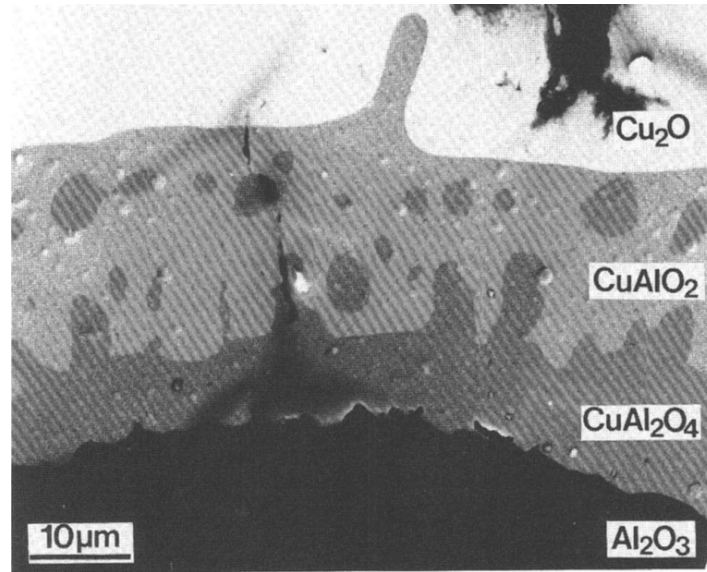
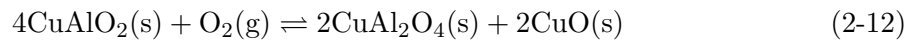
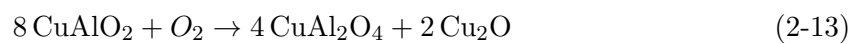


**Figure 2-14:** Alumina and copper oxide interface after 408 hours at 1100 °C in an oxygen rich environment [56]



Research by David W. Susnitzky et al. suggest that the spinel phase could be produced within the delafossite layer ( $\text{CuAlO}_2$ ), with evidence shown by dark spots in micrographs, as can be seen in Figure 2-14 [56]. The appearance of small  $\text{CuAl}_2\text{O}_4$  particles, along with  $\text{Cu}_2\text{O}$  particles and visible pores within the  $\text{CuAlO}_2$  layer, suggests that the delafossite  $\text{CuAlO}_2$  oxidizes to form  $\text{CuAl}_2\text{O}_4$  and  $\text{Cu}_2\text{O}$  during the cooling process through a chemical reaction, as shown in the equation 2-13 [56].



The pores in the material might help oxygen ( $\text{O}_2$ ) move to the  $\text{CuAlO}_2$  layer [56].

### *Formation of the delafossite $\text{CuAlO}_2$*

Delafossite ( $\text{CuAlO}_2$ ) forms between 1000°C and 1100°C in oxygen rich environments [15]. The delafossite can already be forming at around 900 °C, in an inert environment [6]. One of the main pathways for its formation is through a reaction between  $\alpha$ -alumina ( $\text{Al}_2\text{O}_3$ ) and cuprous oxide ( $\text{Cu}_2\text{O}$ ), which results in the production of delafossite. This process can be described by the chemical reaction shown in equation 2-14 [15]. The formation enthalpy of delafossite  $\text{CuAlO}_2$  was estimated by J.M. Ok et al. using the DFT-based Fitted Elemental-Phase Reference Energies (FERE) method [37]. The enthalpy was calculated as -2.7 eV/atom, indicating an exothermic reaction.



Delafossite can also be produced through the reduction of spinel ( $\text{CuAl}_2\text{O}_4$ ). This route involves reduction of the spinel where  $\text{CuAl}_2\text{O}_4$  is gradually converted into  $\text{CuAlO}_2$ , as outlined in reactions 2-11, 2-12, and 2-13 [15, 56]. In environments without oxygen, the reduction of  $\text{CuAl}_2\text{O}_4$  to  $\text{CuAlO}_2$  occurs very slowly [15].

### **Mechanical**

The mechanical properties of the composite changes as the composition of the composite changes. This section focuses on how the Young's modulus is influenced by the composition and microstructure of the composite. It should be noted, that this research started with the user case of ASML, which aimed to achieve the highest possible  $E/\rho$ . Table 2-4 presents the density and stiffness values of the phases studied that were seen in the alumina copper oxide composite. In the following section, the relationship between stiffness, composition, and microstructure will be derived.

The stiffness of a composite material can be estimated using the rule of mixtures. One of the models that is used in the rule of mixtures theory is the Voigt model. This model calculates Young's modulus for a composite in which the reinforcement is continuous and load-bearing throughout the sample [29]. In this model, the alumina particles act as reinforcements and form an interconnected, load-bearing network. The Voigt model, which considers the two materials in the composite to act as parallel springs, is depicted in Figure 2-15 and is mathematically represented by Equation 2-15 [29].

$$E = E_c f_c + E_a f_a \quad (2-15)$$

Where:

- $E$  represents the overall Young's modulus of the composite.
- $E_c$  is the Young's modulus of the copper-phase material.
- $f_c$  is the volume fraction of the copper-phase material.
- $E_a$  is the Young's modulus of alumina.
- $f_a$  is the volume fraction of alumina.

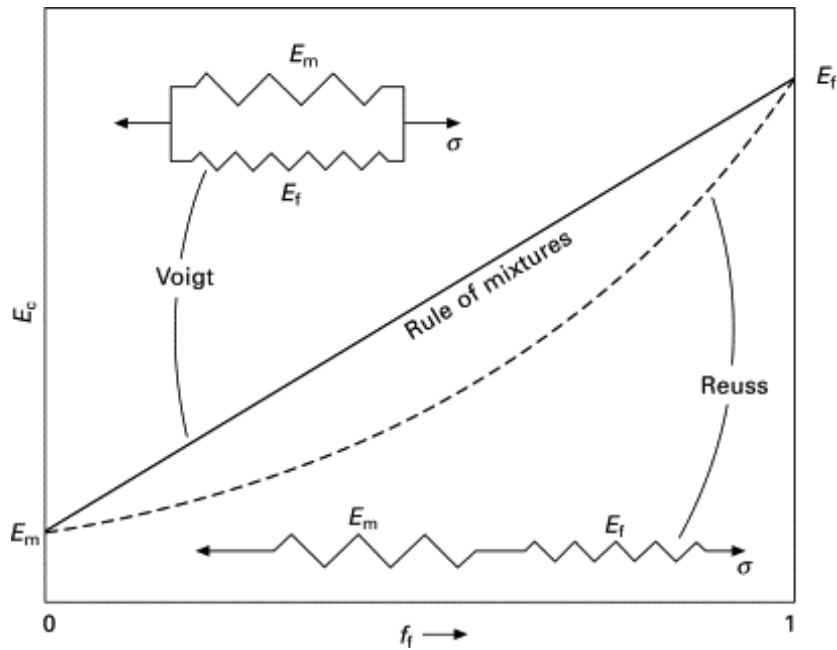


**Figure 2-15:** The Young's Modulus of composites as a function of volume fraction, based on equations 2-15 and 2-16 [29]

The Voigt model assumes that strain is uniform across the composite, while stress differs between the two phases.

Using the values from Table 2-4 and Formula 2-15, it becomes clear that a higher alumina content increases the Young's modulus of the material. Increasing the alumina fraction improves also the density characteristics. When ternary oxide forms, it decreases the alumina content in the composite. This decrease is explained by the reactions in equations 2-10 and 2-14, where alumina is consumed to form  $\text{CuAl}_2\text{O}_4$  and  $\text{CuAlO}_2$ .

Too much ternary oxide can cause the alumina phases in the porous structure to become disconnected. This is assumed to be visible in Figure 2-16, where the non-connected alumina regions are marked with the letter A. When the alumina phases are not interconnected, they cannot transfer loads effectively, meaning the alumina is no longer load-bearing. In this case, the composite behaves like a series of springs. The Young's modulus of the composite can then be determined by the Reuss model, which assumes that the two materials act like springs in series. The formula for this can be found in equation 2-16 [29].

$$E = \left( \frac{f_a}{E_a} + \frac{1 - f_a}{E_c} \right)^{-1} \quad (2-16)$$

In the Reuss model, the stress is uniform across the composite, while strain differs between the two phases.

As seen in Figure 2-15, the Reuss model predicts a lower stiffness compared to the Voigt model. This shows why disconnected alumina phases are undesirable. Thus, reducing the formation of ternary oxides is crucial to keep the alumina phases connected and maintain the load-bearing capacity of the composite.

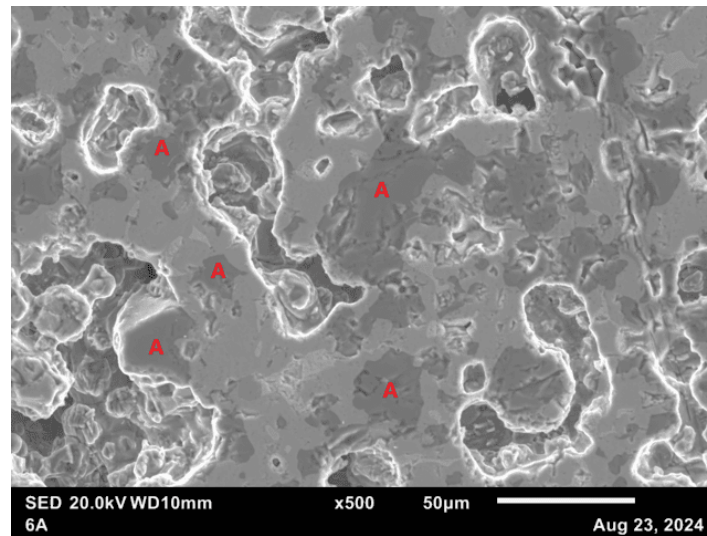


**Figure 2-16:** scanning electron microscope (SEM) scan of alumina infiltrated with copper oxide; A marks the alumina phase

In conclusion, achieving a composite with a high  $E/\rho$  requires maximizing the alumina content. This is due to alumina's combination of the highest Young's modulus and lowest density, as shown in Table 2-4, in accordance with the rule of mixtures.

Material	Density (g/cm <sup>3</sup> )	Stiffness (Young's Modulus, GPa)	Source
Alumina (Al <sub>2</sub> O <sub>3</sub> )	3.96	370	[54]
Cuprous Oxide (Cu <sub>2</sub> O)	6.0	~110	[40]
Cupric Oxide (CuO)	5.94	~140	[41]
CuAl <sub>2</sub> O <sub>4</sub>	Not widely reported*	Not widely reported*	
CuAlO <sub>2</sub>	4.9	~180	[3, 39]

**Table 2-4:** Density and Stiffness of Different Materials. \*Data not widely available, but likely significantly lower than alumina

## 2-3 Pressureless infiltration

In this section the pressureless infiltration process of a liquid phase is elaborated, where a liquid phase is infiltrated into the porous component without any external pressure component used as a driving force. The liquid phase is later on solidified to create one dense solid structure. This technique can be used to densify a porous structure, that is created by PBBJ. This theoretical background explores key principles, such as wettability and Jurin's law. It also evaluates the advantages and disadvantages of pressureless infiltration in combination with PBBJ.

### Working Principle

Infiltrating the porous structure object with a liquid phase is a technique used for reducing its porosity. The process involves absorbing the liquid phase in a porous structure, like a sponge absorbing water. The liquid phase is transferred to the pores in the porous structure. Subsequently, the liquid phase solidifies and reinforces the overall structure. The effectiveness of this process is largely depended on the capillary action, which is influenced by the principles of wettability and Jurin's law [7].

Wettability measures how easily a liquid spreads across a solid surface, quantified by the contact angle between the liquid and the solid. A lower contact angle indicates better wettability, meaning the liquid can more easily penetrate the porous structure [10]. The contact angle for pressureless infiltration must be low enough to ensure effective capillary action. The rule of thumb is, that for spontaneous infiltration the contact angle must be at least lower than 90 degrees (the lower the better) ( $\theta < 90^\circ$ ) [7]. In Figure 2-17, an schematic drawing can be seen of the working principle of the contact angle and wetting and non-wetting behaviour.

The contact angle  $\theta$  is calculated with equation 2-9. This equation highlights the parameters influencing the contact angle and thereby the infiltration of the alumina porous structure by the liquid phase. The contact angle is reduced by increasing  $\gamma_{SV}$  and decreasing  $\gamma_{SL}$ . Lowering  $\gamma_{LV}$  while maintaining constant  $\gamma_{SV}$  and  $\gamma_{SL}$  will reduce the wetting angle in systems that are already wetting, but it cannot convert a non-wetting system ( $\theta > 90^\circ$ ) into a wetting one ( $\theta < 90^\circ$ ).

The wettability is also sensitive to more factors than only the contact angle. Wettability depends on factors like reactivity, solubility, interface reactions, surface roughness, impurities, melt oxidation, processing conditions, matrix composition and even the atmosphere. The wettability can be adjusted by introducing extra alloying elements in the to be infiltrated liquid phase [10].

Jurin's law describes the capillary rise of a liquid in a narrow tube. An schematic view of capillary rise can be seen in Figure 2-18. According to Jurin's law, the height  $h$  to which a liquid will rise in a capillary tube in an axisymmetric case is given by 2-17 [27].

$$h = \frac{4\gamma \cos \theta}{\rho g d} \quad (2-17)$$

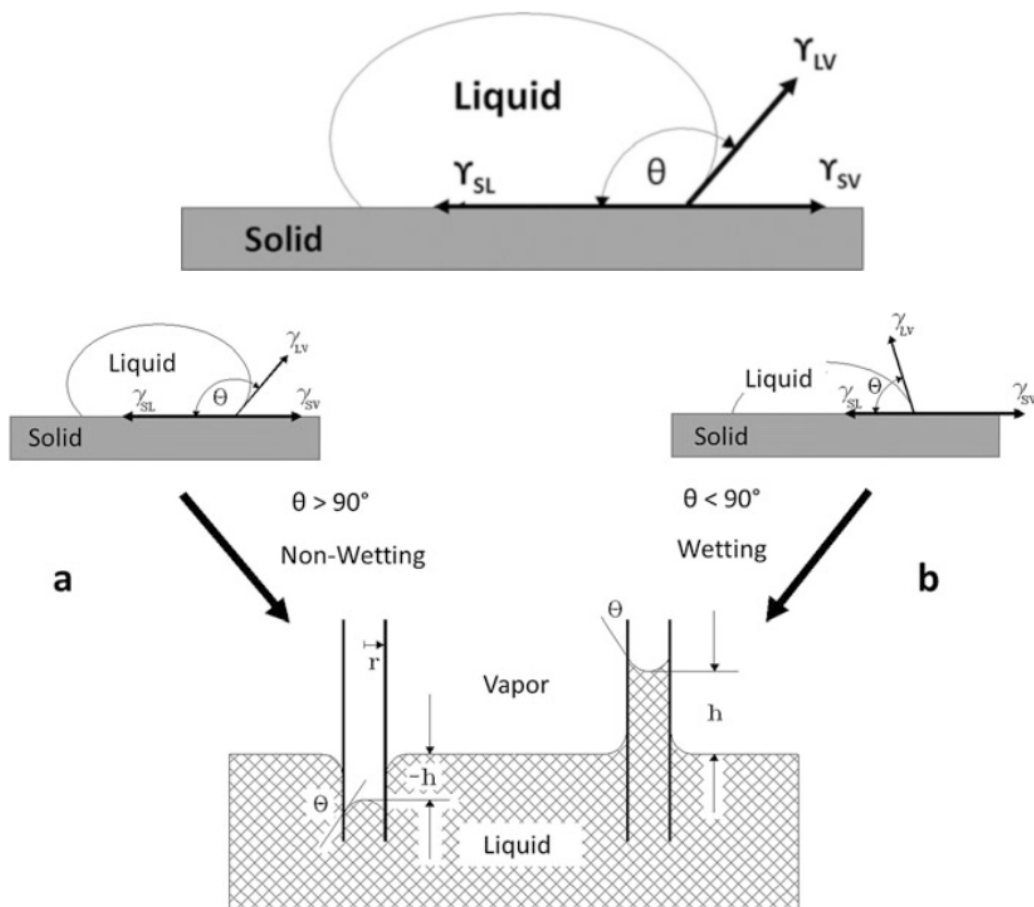


**Figure 2-17:** Surface forces acting at the point of intersection of a liquid resting on a solid; (a) Non-wetting system. (b) Wetting system in function of the contact angle [7]

where:

- $\gamma$  is the surface tension of the liquid,
- $\theta$  is the contact angle (related to wettability),
- $\rho$  is the density of the liquid,
- $g$  is the acceleration due to gravity,
- $d$  is the diameter of the capillary tube (or pore size).

In porous structures, smaller pore sizes, liquids with higher surface tension and a lower contact angle enhance infiltration effectiveness. Smaller pores can also increase the likelihood of clogging, leading to closed porosity, which can obstruct further infiltration. Therefore it is needed to optimize the porosity and pore size, to achieve the highest densification.

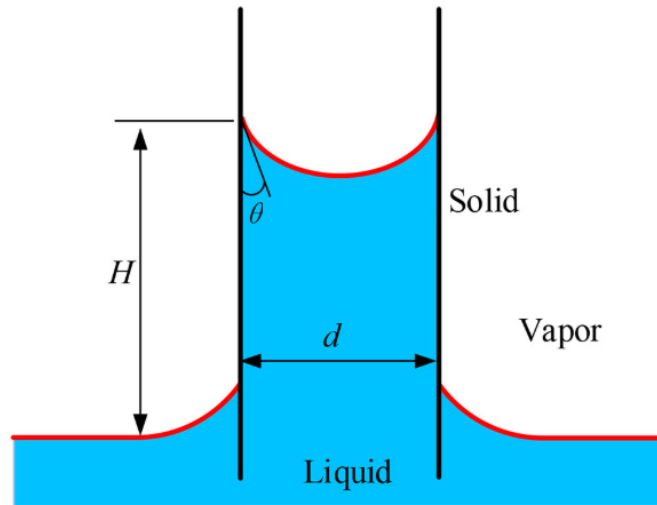


Figure 2-18: Schematic of the capillary rise [27]

### Advantages

In this section the advantages of pressureless infiltration combined with PBBJ are elaborated.

- *Enhanced mechanical properties:* Infiltration can significantly increase the mechanical strength, hardness, and wear resistance of alumina by filling the pores and creating a denser structure. In Figure 2-19, the strength of the liquid infiltrated PBBJ samples are compared to samples without liquid infiltration for alumina PBBJ structures. It can be seen that the liquid infiltration samples have a significant higher flexural strength. The highest flexural strength so far with alumina is 317.5 MPa, where a PBBJ structure is infiltrated with liquid copper in a oxygen rich environment [42].

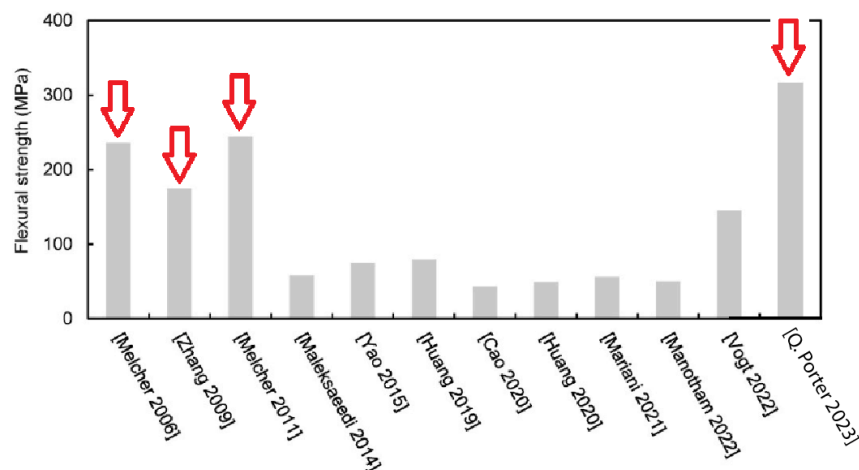
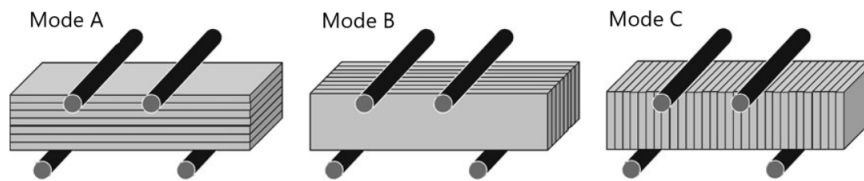


Figure 2-19: Comparison of the flexural strengths of alumina-based specimens fabricated by PBBJ, followed by sintering. The red arrow indicate the infiltrated samples with a liquid phase metal or ceramic [42]

- *Reduced porosity:* The pressureless infiltration of a liquid phase significantly reduces the porosity in the porous alumina. In the research of Q. Porter, an open porosity of  $0.6 \pm 0.2\%$  was measured for alumina infiltrated with copper in an oxygen rich environment [42].
- *Customized properties:* By selecting the right infiltrating materials, the properties of the composite can be selected to specific applications.
- *Reduced anisotropy:* Binder jetting often results in anisotropic properties due to the layer-by-layer nature of the printing process. Infiltration helps to reduce this anisotropy by uniformly filling the pores and creating a more homogeneous material structure, thereby enhancing the isotropic mechanical properties. In Table 2-5 the mechanical properties regarding different orientations of the sample are displayed of the uninfiltrated and the infiltrated sample. The testing orientations that were used can be seen in Figure 2-20 [31]. This shows that the isotropic properties are improved due to infiltration.
- *Dimensional accuracy:* Since the green body requires minimal shrinkage during sintering to achieve high density liquid melt infiltration, the risk of shrinkage defects can be significantly reduced. This method can enhance dimensional accuracy and help minimize shrinkage cracks [28].



**Figure 2-20:** Sample loading modes according to the layer-by-layer build process of PBBJ. The flexural strength results with the different loading modes can be found in Table 2-5 [31]

**Table 2-5:** Mechanical properties of  $\text{Al}_2\text{O}_3$  (without infiltration) and  $\text{Al}_2\text{O}_3/\text{Cu-O}$  composites (with infiltration). The loading modes are based on Figure 2-20 [31]

	Mode A	Mode B	Mode C
<b><math>\text{Al}_2\text{O}_3</math> (without infiltration)</b>			
4-Point bending strength (MPa)	$56 \pm 3$	$53 \pm 3$	$19 \pm 2$
Young's modulus (GPa)	$113 \pm 5$	$93 \pm 4$	$92 \pm 13$
Fracture toughness $K_{Ic}$ ( $\text{MPa}\sqrt{\text{m}}$ )	$1.6 \pm 0.1$	$1.8 \pm 0.1$	$0.5 \pm 0.1$
<b><math>\text{Al}_2\text{O}_3/\text{Cu-O}</math> Composite (with infiltration)</b>			
4-Point bending strength (MPa)	$236 \pm 32$	$245 \pm 43$	$222 \pm 15$
Young's modulus (GPa)	$204 \pm 8$	$198 \pm 9$	$194 \pm 9$
Fracture toughness $K_{Ic}$ ( $\sqrt{\text{m}}$ )	$5.5 \pm 0.3$	$5.6 \pm 0.8$	$5.0 \pm 1.0$
Vickers' hardness $\text{HV}_{10}$ (GPa)	$2.5 \pm 0.1$	$2.4 \pm 0.3$	$2.4 \pm 0.5$

## Disadvantages

- *Complex processing:* The infiltration process adds extra steps to the process, which needs a precise control of temperature, pressure, and atmosphere to ensure successful infiltration without defects. This will all add up to the complexity.
- *Material compatibility:* Not all metals or ceramics in liquid phase are compatible with alumina. The melting temperature of the liquid phase must be lower than the temperature where the porous structure is mechanically stable. The liquid phase must have a low contact angle on the solid state, in order to make pressureless infiltration happen.
- *Cost:* The additional steps and materials involved in infiltration can increase the overall cost of producing the composite material. For example an extra heating cycle is needed, which is increasing the energy usage.
- *Thermal stress:* Differences in thermal expansion coefficients between the solid state and the liquid phase can induce thermal stresses during cooling, potentially leading to cracks or other defects [7].
- *Incomplete infiltration:* Incomplete infiltration occurs when the liquid phase cannot fully penetrate the porous alumina, due to closed porosity or too limited capillary driving force. Closed pores are isolated cavities that are not in connection with the external surface. This can be seen in Figure 2-3. To minimize this issue, the infiltration process must be optimized.
- *Multi phase material:* Introducing a liquid phase into a porous base material will result in the formation of multiple phases. Some of these phases may not be suitable for the given application area. This can present potential issues for compatibility.

### Infiltration time

It is important to determine how long the system should be maintained at the infiltration temperature in order to fully infiltrate the porous body. This infiltration time can be calculated. The Lucas-Washburn equation is a useful tool to estimate how fast this infiltration occurs [11]. The standard Lucas-Washburn equation does not include the effect of gravity, which is important for vertical infiltration.

Therefore the Lucas-Washburn equation was modified to account for gravity as this was a factor that couldn't be ruled out [11, 62]. The modified formula can be found in equation 2-18.

$$t = -\frac{h}{b} - \frac{a}{b^2} \ln \left( 1 - \frac{bh}{a} \right) \quad (2-18)$$

Where:

$$a = \frac{\sigma R \cos \theta}{4\mu} \quad (2-19)$$

and

$$b = \frac{\rho g R^2 \sin \psi}{8\mu} \quad (2-20)$$

- $a$  represents the capillary force driving the infiltration (without gravity)
- $b$  accounts for the effect of gravity on the infiltration process
- $\sigma$  is the surface tension of the liquid
- $R$  is the pore radius
- $\theta$  is the contact angle between the liquid and the surface
- $\mu$  is the dynamic viscosity of the liquid
- $\rho$  is the density of the liquid
- $g$  is the acceleration due to gravity
- $\psi$  is the infiltration angle

This modified formula allows to calculate the infiltration time. It can ensure that the sample remains at the infiltration temperature long enough for the liquid phase to infiltrate the porous structure. In figure 2-21, the infiltration set-up is displayed and the relating units  $g$ ,  $h(t)$  and  $\psi$  are displayed.

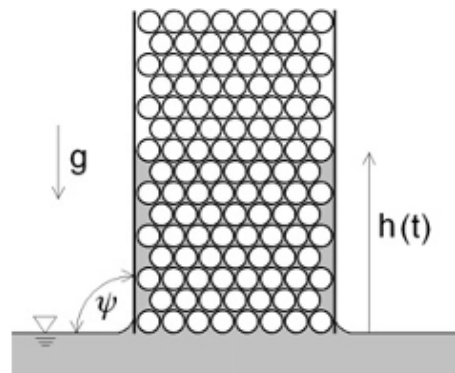


**Figure 2-21:** Schematic representation of infiltration in a porous medium [11]

## 2-4 Research questions

- What impact does the infiltration of copper oxide into porous alumina have on the chemical, mechanical and microstructural properties of the resulting composite?
- What phase transformations occur during the thermal cycle of infiltration in nitrogen?
- Can the infiltrated composite be applied in ASML technologies?

---

# Chapter 3

---

## Methodology

The methodology for this project is summarized in Figure 3-1, which provides a block diagram detailing each step. It starts with the fabrication of alumina porous samples with powder bed binder jetting (PBBJ). These 3D-printed samples are then cured and sintered. The sintered samples undergo microstructural characterization. This characterization is used for the infiltration process that follows. In the infiltration process the samples are infiltrated in an oxygen-rich environment. The microstructure and mechanical properties (particularly flexural strength) of the infiltrated samples are evaluated. Next, the potential of infiltrating in a nitrogen environment is assessed. This is done by a simulation experiment of the infiltration process in a nitrogen atmosphere. This simulation aims to identify phase transitions and serves as a preparatory step for future nitrogen infiltration experiments.

Each step in the figure is explained further in Section 3-1 till Section 3-3.

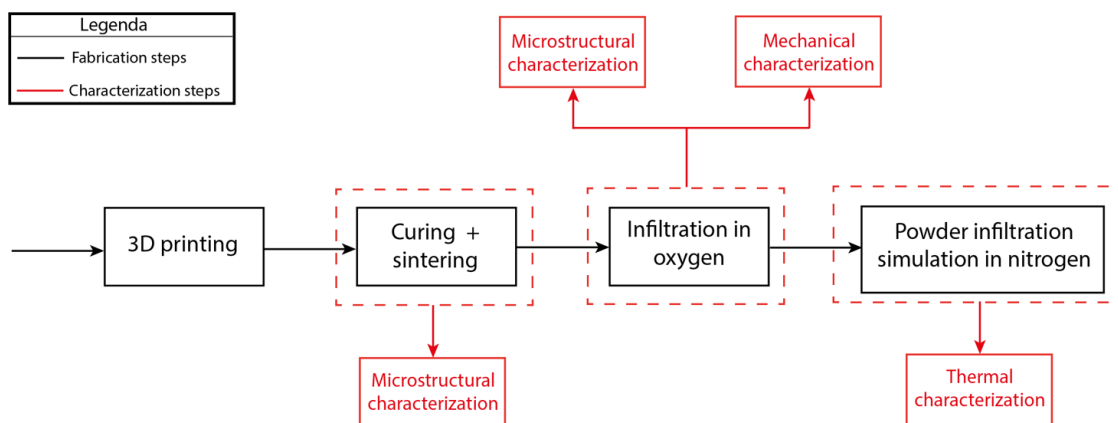


**Figure 3-1:** Graphical representation of the project methodology: black lines are indicating the fabrication process, while red lines indicate the characterization process

### 3-1 Powder bed binder jetting

In this section, it is described which materials and process parameters were used for PBBJ.

#### Materials

The powder used for the PBBJ process is  $\alpha$ -alumina, with a purity of 99.9%. Two sizes of powder were selected for this study: 10  $\mu\text{m}$  (BAK-10, xtra GmbH, Germany) and 20  $\mu\text{m}$  (BAK-20, xtra GmbH, Germany). It is important to note that no multimodal mixtures of powders were used in this research. Before the printing process, each batch of powder was dried in an oven (Yamato DX412C, Japan) at 200°C for a minimum of 12 hours. This step was essential to reduce moisture content, as excess moisture can significantly impact the flowability, packing density and printing quality. After drying, the powder was sieved using a 106  $\mu\text{m}$  (140 mesh) sieve to ensure a uniform distribution before deposition onto the powder bed.

#### Printing

The alumina parts were fabricated using a binder jet printer (BJP), ExOne - Innovent Plus (Huntington, PA, USA). The ExOne BJP features a build envelope of 65 × 65 × 160 mm, with a printhead consisting of 256 nozzles. The binder used in this study was an aqueous-based liquid binder with a density of 1.06 g/cm<sup>3</sup>, supplied by ExOne (Huntington, PA, USA). Figure 3-2 shows the BJP used for printing the alumina samples. The process parameters employed during PBBJ are summarized in Table 3-1. These values are based on prior research conducted by A.K. Mohan, which determined the ideal printing conditions for avoiding defects in the green body [34].

During the printing process, adjustments to the binder set time and drying time were occasionally necessary. An ideal combination of parameters could not be consistently identified. This variability might be influenced by the environmental conditions surrounding the printer.

The target powder bed temperature of 65°C was not achieved during the printing process. Instead, the bed temperature stabilized at 55°C. Achieving the target temperature would have required additional heating time, but this led to overdrying symptoms. Despite this, the printed parts were of satisfactory quality at 55°C. Therefore, it was assumed that the deviation from the target temperature did not significantly impact the printing results.

After the printing process is finished, the whole set-up of the powder bed including the printed samples within the powder bed is put inside an open air oven (Yamato DX412C, Japan). The conditions are 200°C for 6 hours to fully cure the binder. These curing settings were provided by the binder manufacturer (ExOne). The green bodies that are cured, but still in the powder bed, can be seen in Figure 3-3. The green bodies that are cured and depowdered can be seen in Figure 3-4.



**Figure 3-2:** BJP by ExOne

**Table 3-1:** Process Parameters

Parameter	Value
Binder set time	5-10 seconds
Heating time	20-25 seconds
Emitter output	90%
Target Bed Temperature	65°C
Recoat speed	200 mm/second
Roller speed	200 rpm
Roller traverse speed	10 mm/second
Roughing roller speed	400 rpm
Saturation	90%
Ultrasonic intensity	50%
Delay on dispenser	1 second
Layer thickness	Twice the powder size

### Sintering

The cured alumina bodies are placed inside a furnace (LHTG 200-300/22-2G, Carbolite Gero GmbH & Co. KG, Germany) on an high density alumina flate plate (see Figure 3-4). The furnace operates in an argon atmosphere, where the debinding and sintering processes take place.

The whole debinding and sintering thermal cycle can be seen in Figure 3-5. The debinding



**Figure 3-3:** Cured alumina bending bar samples produced by PBBJ embedded within the powder bed



**Figure 3-4:** Cured alumina bending bar samples produced by PBBJ depowdered and put onto a alumina flat plate

thermal cycle is advised by the manufacturer of the binder (ExOne). After debinding, the samples are sintered at  $1550^{\circ}\text{C}$ , with a holding time of 24 hours.

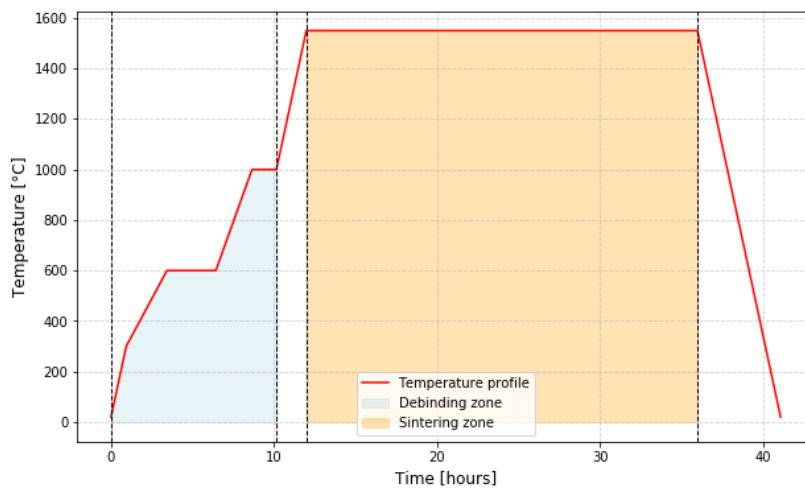


**Figure 3-5:** Thermal cycle of debinding and sintering used in this research

The sintering process, provided by the manufacturer of BJP (ExOne) resulted in more warpage of the alumina samples, what is unwanted. This sintering process was executed at  $1650^{\circ}\text{C}$  for 6 hours in vacuum.

## 3-2 Infiltration setup

### Materials

Two materials were used for infiltration in this research. Metallic copper powder with a particle size of  $149\ \mu\text{m}$  (100 mesh) and a purity of 99%. This material was supplied by Thermo Scientific Chemicals.  $\text{Cu}_2\text{O}$  powder with a particle size of  $74\ \mu\text{m}$  (200 mesh) and a purity of 99%. This material was also supplied by Thermo Scientific Chemicals.

### Infiltration set-up

Two infiltration setups have been developed and utilized in this research.

- *Infiltration setup A* was designed as a fast method for infiltration. This setup does not need a porous infiltration structure, making the process easier. It is not possible to recover a complete sample with this setup; only about 50% of the sample can be retrieved. This happens because the bottom side of the bending bar sample gets stuck in the meltpool of the solidified infiltrated material. The microstructure and chemical composition can still be analyzed using this setup. In this setup, the bending bar is placed vertically inside an alumina thimble crucible. The powder that will be infiltrated in liquid phase, is placed next to the bending bar sample, as shown in Figure 3-6. Figure 3-7 shows the prepared setup A before it is placed in the oven to start the infiltration process.

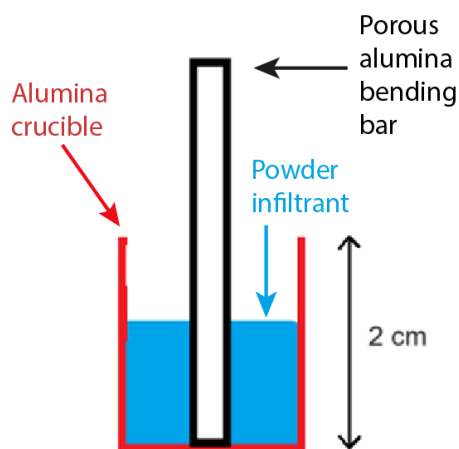


**Figure 3-6:** Schematic view of cross section of infiltration setup A for pressureless infiltration



**Figure 3-7:** Infiltration setup A before the pressureless infiltration

- *Infiltration setup B* was developed for infiltrating bending bars. Unlike setup A, it allows for the extraction of a complete and intact sample. This is necessary for strength and density measurements. Infiltration setup B consists of a base plate and infiltration pillars, as shown in Figure 3-8. The dimensions of infiltration setup B can be found in Figure 3-9. Four different columns of pillars are included in the infiltration setup to study how the diameter and number of the pillars affect the densification of the bending bars. The columns are marked with red letters for identification. In section 4-2, the results of the differences in infiltration pillars on the density will be given.

The entire setup is placed inside an alumina crucible for infiltration. The powder that will be infiltrated is placed next to the pillars, as shown in Figure 3-8. The bending bars to be infiltrated are positioned on top of the infiltration pillars, as shown in Figure 3-9.

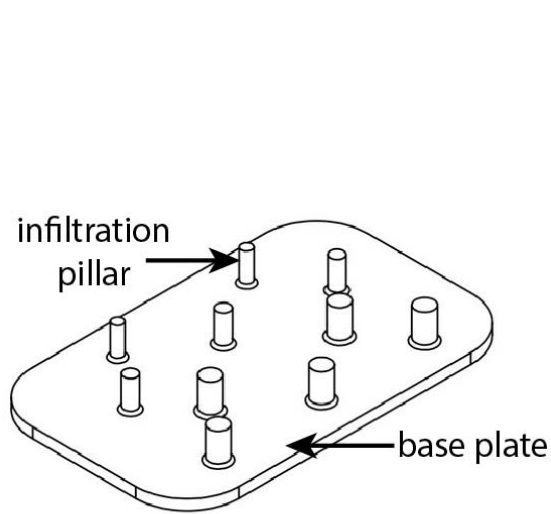


**Figure 3-8:** Schematic view of infiltration setup B

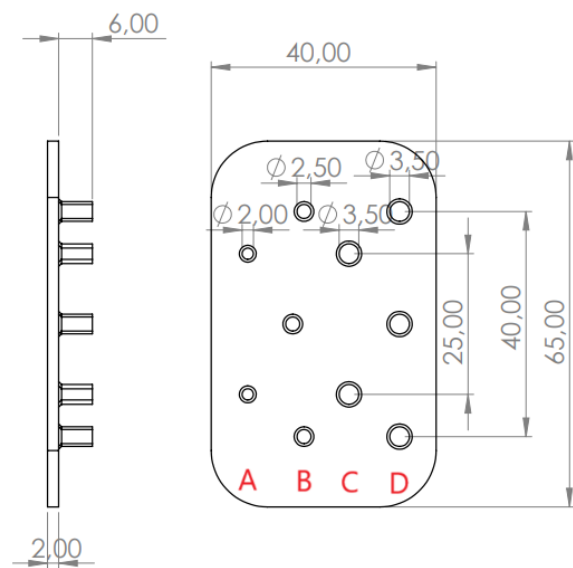


**Figure 3-9:** Schematic view of the dimensions of the infiltration setup B. With red letters are the 4 different columns of pillars indicated



**Figure 3-10:** Infiltration setup B, with powder along the infiltration pillars



**Figure 3-11:** Infiltration setup B, with the bending bar samples on top of the infiltration pillars

### Infiltration temperature cycle

The infiltration temperature cycle involves heating, an optional isothermal hold, and cooling. The parameters are the infiltration temperature, the infiltration time (the isothermal hold) and the heating rates. During this study, the heating cycle was initially reproduced based on existing literature. This thermal cycle included a heating rate of 7.5 K/min, a 90-minute isothermal hold, and an infiltration temperature of 1300°C [42, 31]. After this, more optimal thermal cycles were used in the infiltration simulation, based on the optimization of the parameters of the thermal cycles. These are elaborated below.

- *Infiltration temperature*

The infiltration temperature must at least equal the melting point of the infiltrated material, which in this research is copper oxide. Pressureless infiltration relies on the wetting of the alumina porous structure by the liquid copper oxide. Without achieving a liquid state, the copper oxide cannot wet the pores and infiltration will not occur [10]. To identify this minimum wetting temperature, a differential thermal analysis (DTA) test was conducted. The process of the DTA is detailed section 3-3. The minimal wetting temperature is represented by the peak temperature of Peak 2 in Section 4-3-2. This temperature is measured as 1235°C.

- *Infiltration time*

The infiltration time of a porous body can be determined using Equation (2-18). In this section, the infiltration time for a porous body at 1250°C and  $pO_2 = 0.2$  will be calculated for infiltration setup A. The formula uses several variables that have been explained previously, as summarized in Table 3-2. These conditions, including the temperature of 1250°C, will also be used later in the study to obtain the results. The infiltration time remain within a safety margin since, in practice, the infiltration angle is less than 90°. This shortens the infiltration time. This is due to the vertical samples resting against the edge of the alumina crucible in infiltration set-up A (see Figure 3-7).

**Table 3-2:** List of variables \*The infiltration is going vertically upwards

Variable	Value	Source
$\sigma$	311 mN/m	Section 2-2-2
$\theta$	32 deg	Section 2-2-2
$R$	9.1 $\mu\text{m}$	Section 4-1
$\mu$	0.013 Pa · s	Figure 2-8
$\rho$	6 g/cm <sup>3</sup>	Table 2-4
$g$	9.81 m/s <sup>2</sup>	
$\Psi$	90 deg	*
$h$	4 cm	Figure 3-6

First  $a$  can be calculated with equation 2-19. The calculation can be found in equation 3-1.

$$a = \frac{\sigma R \cos \theta}{4\mu} = \frac{311 \times 10^{-3} \times 9.1 \times 10^{-6} \times \cos(32^\circ)}{4 \times 0.013} = 4.62 \times 10^{-5} \text{ m/s} \quad (3-1)$$

Then  $b$  can be calculated according to equation 2-20. The calculation of  $b$  can be found in equation 3-2.

$$b = \frac{\rho g R^2 \sin \Psi}{8\mu} = \frac{6 \times 10^3 \times 9.81 \times (9.1 \times 10^{-6})^2 \times \sin(90^\circ)}{8 \times 0.013} = 4.69 \times 10^{-5} \text{ m/s} \quad (3-2)$$

With both variables  $a$  and  $b$  known, the infiltration time can be calculated with formula 2-18. The calculation can be found in equation 3-3.

$$t = -\frac{h}{b} - \frac{a}{b^2} \ln \left( 1 - \frac{bh}{a} \right) = 18 \text{ seconds} \quad (3-3)$$

- *Heating rates*

The heating rates ranged from 1 to 10 K/min per minute. The slow heatrate was determined to be 1K/min per minute, while the fast heatrate was determined to be 10K/min. This upper limit was chosen to minimize the risk of damaging the delicate alumina crucibles, which may not withstand rapid temperature changes. For the infiltration experiments in oxygen, 7.5 K/min per minute was selected as a balanced option, aligning with commonly reported values in related studies [42, 31].

### Infiltration oven

For infiltration a Lenton tube furnace was used, with an alumina crucible tube. An image of the tube oven can be seen in Figure 3-12.

The environment was controlled with gasflows of O<sub>2</sub> and N<sub>2</sub>. For a test in oxygen (pO<sub>2</sub> of 0.2 atm), a gasflow of 50 mL/min O<sub>2</sub> and 200 mL/min N<sub>2</sub> was used. For a test in a nitrogen environment, the oven was prior to the heating cycle flushed for an hour with 250 mL/min N<sub>2</sub>. Hereafter the experiment was conducted with an gasflow of 250 mL/min N<sub>2</sub>.



**Figure 3-12:** Lenton tube furnace, used for infiltration

### 3-3 Characterization techniques

In the following section the characterization techniques are elaborated.

#### Density analysis

In order to perform density measurements, first the dimensional measurements must be made to calculate the volume of the sample. This measurement is done by measuring three times. Two times on the outer sides and one time in the middle. The average of these three measurements was taken for the final value. The dimensions are measured using a Horex digital caliper (150 mm), which provides a precision of two decimals. For determining the sample's weight, the Precisa Series 321 LX 120 A weight scale is used, offering an accuracy of 0.1 mg. The sides of the sample are not grinded. With the volume determined from the averaged dimensional measurements, the relative density (bulk density, see Table 2-1) is calculated by dividing the sample's weight by its calculated volume.

The density of the infiltrated samples is calculated as follows: the initial relative density and mass of the sample that has to be infiltrated are known. After infiltration, the weight gain is measured. This weight gain is then divided by the density of the infiltrated material to calculate the volume of the infiltrated product. This calculated volume is then divided by the volume of the sample bending bar, resulting in the relative density increase. Adding this increase to the initial relative density provides an estimate of the infiltrated sample's overall density. The equation for calculate the density after infiltration is given by equation 3-4.

When infiltrating copper oxide, it is not always clear whether  $\text{Cu}_2\text{O}$  or  $\text{CuO}$  has been infiltrated. Their densities are very similar (within a 1% range), as shown in Table 2-4. Therefore, the density of the infiltrated material is assumed to be  $6 \text{ g/cm}^3$ .

$$\rho_{\text{final}} = \rho_{\text{initial}} + \frac{\Delta m}{\rho_{\text{infiltrated}} \cdot V_{\text{sample}}} \quad (3-4)$$

where:

- $\rho_{\text{final}}$  is the final relative density of the infiltrated sample (dimensionless, as a ratio).
- $\rho_{\text{initial}}$  is the initial relative density of the sample (dimensionless, as a ratio).
- $\Delta m$  is the weight gain after infiltration (measured in g).
- $\rho_{\text{infiltrated}}$  is the density of the infiltrated material (measured in  $\text{g}/\text{cm}^3$ ).
- $V_{\text{sample}}$  is the volume of the sample bending bar (measured in  $\text{cm}^3$ ).

### Mechanical testing

The flexural strength of the samples was measured in accordance with ASTM C1161-16, utilizing a three-point bending test performed on a Zwick Z010 testing machine. The test employed a span of 40 mm (configuration B in the ASTM C1161-16). The bending bar sample dimensions included a width of 4.21 mm with a standard deviation of 0.05 mm and a height of 3.24 mm with a standard deviation of 0.01 mm. Prior to testing, the samples were grinded to a surface finish of P800. A loading rate of 1 MPa/s was applied during the bending test. In total, 10 samples were tested to obtain an average value for the flexural strength, as specified by ASTM C1161-16.

### Microstructural analysis

For the microstructural analysis, scanning electron microscope (SEM), Energy-dispersive X-ray spectroscopy (EDS), and optical microscopy were used. The SEM and EDS analyses were performed using the JSM-IT100 (Jeol, Japan), and the optical microscopy was done with the Keyence VHX-7100.

Samples were prepared by cutting them with a cutting machine (Struers, Discotim-6). After cutting, the samples were hot-pressed in epoxy resin using a Struers CitoPress-5 (using conductive resin for SEM and EDS analysis). Non-infiltrated samples, due to their high porosity and therefore high brittleness, were cold-mounted in conductive resin instead of hot-pressing.

The embedded samples were then ground using SiC abrasive paper with various grit sizes: P80, P180, P320, P800, P1200, and P2000. Polishing was performed with diamond paste in two steps: first using 3  $\mu\text{m}$  paste and then 1  $\mu\text{m}$  paste. After polishing, the samples were immersed in isopropanol and cleaned using an ultrasonic cleaner.

For SEM and EDS analysis, the samples were made conductive by applying a thin carbon coating via sputter deposition using an automatic carbon sputter coater (JEC-530, Jeol, Japan). For optical analysis, no carbon coating was applied.

The cross sections analyzed during the microstructural study is shown in Figure 3-13. Different orientations were analyzed according to the printing directions. In each figure of the microstructure, it is indicated which orientation has been used.

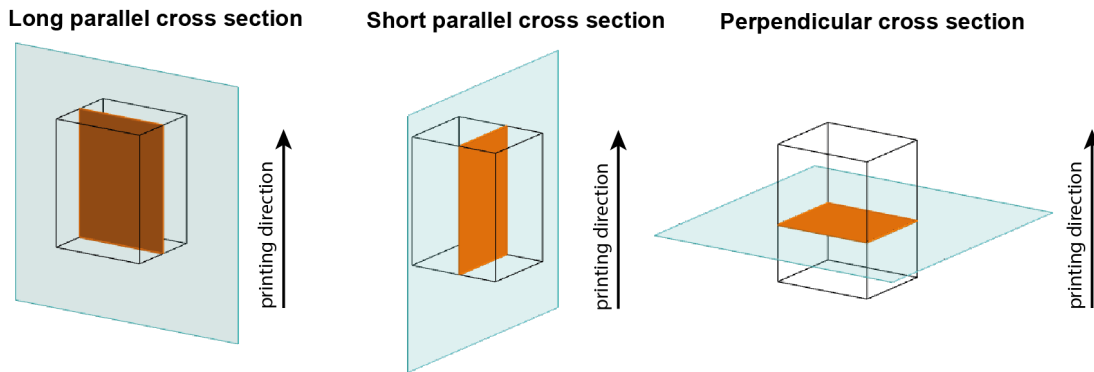


**Figure 3-13:** Indication of the cross section views

### TGA and DTA

thermogravimetric analysis (TGA) and DTA were used to simulate infiltration in nitrogen. Powders of alumina and copper oxide were mixed and placed in the TGA + DTA equipment, where a thermal infiltration cycle was simulated. Data from the TGA and DTA were used to identify of phase transitions occurring during infiltration. Two powder mixtures were analyzed: an equimolar 1:1  $\text{Al}_2\text{O}_3\text{-Cu}_2\text{O}$  mixture (referred to as the equimolar mixture) and a  $\text{Cu}_2\text{O}$ -only powder (referred to as  $\text{Cu}_2\text{O}$ -only). This was done to make sure to differentiate the processes happening from  $\text{Cu}_2\text{O}$  and from the reactions between  $\text{Al}_2\text{O}_3$  and  $\text{Cu}_2\text{O}$ . An equimolar ratio was selected so the two powders could fully react and produce ternary oxides. By applying different heating cycles, different weight percentages of ternary oxides form, providing insight into the process's reaction kinetics.

At the start of the heating cycle, the temperature was held at  $200^\circ\text{C}$  for 30 minutes to ensure complete moisture evaporation. Small alumina crucibles, weighing 190 mg, were used to accommodate the powders, and sample powders weighed 160 mg with an error margin of  $\pm 1\%$ .

The peaks quantified in the results tables were normalized for the  $\text{Cu}_2\text{O}$ -only mixture. Since the  $\text{Cu}_2\text{O}$ -only mixture contains more  $\text{Cu}_2\text{O}$  than the equimolar mixture, normalization ensures that the theoretical amount of  $\text{Cu}_2\text{O}$  is equivalent in both tests.

The TGA and DTA was conducted using a Setaram SETSYS Evolution machine. TGA tracks weight changes while heating, showing the reactions or phase transformations [52]. Differential thermal analysis (DTA) measures heat flow during phase changes. Tracking these thermal changes at certain temperatures identifies the reactions happening [60]. A comprehensive understanding of the phase changes in the system can be achieved by combining the TGA and DTA. The gas flow in the machine was set to 50 mL/min of  $\text{N}_2$ .

Differential Scanning Calorimetry (DSC) was not used in this study. Extra specific calibration was needed in order to use this technique. Although the machine is also capable of DSC. In this study, DTA was primarily used for qualitative analysis, with some semi-quantitative evaluations conducted.

### **X-ray diffraction (XRD)**

XRD phase identification and quantification were performed using powders prepared by pulverizing samples with a ball mill (Fritsch Analysette 3 Spartan) for 3 minutes. The powders were deposited on a Si 510 zero-background wafer. Measurements were carried out using a Bruker D8 Advance diffractometer with Bragg-Brentano geometry, equipped with a graphite monochromator and a Vantec position-sensitive detector. Co  $K\alpha$  radiation was used, with the instrument settings including a divergence slit var12, scatter screen height of 8 mm, and operating conditions of 40 kV and 40 mA. A locked coupled  $\theta$ - $2\theta$  scan was performed over a range of  $10^\circ$  to  $135^\circ$   $2\theta$ , with a step size of  $0.03^\circ$   $2\theta$  and a measurement time of 2 seconds per step. The Rietveld analysis of the obtained data was conducted using Bruker DiffraSuite.EVA version 7.2 and Profex/BGMN version 5.2.

The crucibles used in the TGA and DTA analyses were also utilized to measure the phase composition. However, due to the small size of the crucibles, it was not possible to extract the melted and subsequently solidified contents directly. Therefore, the crucibles and their contents were ball-milled into powder. The crucible weight was known to be 190 mg, while the content of the crucible weighed 160 mg.

In the Rietveld analysis, the weight of the alumina from the crucibles was accounted for by subtracting its proportion ( $190/(190 + 160) = 54\%$ ). The results were then rescaled to 100% for clarity. The scaled phase composition data are presented in Table 4-6.

---

# Chapter 4

---

## Results

In this chapter the results are elaborated. First, the outcome of powder bed binder jetting (PBBJ) are discussed in Section 4-1. The focus in this section lies on examining the density and porosity characteristics of the alumina porous body produced using PBBJ. In the next section (Section 4-2) the results of the copper oxide infiltration process conducted in an oxygen environment is displayed. The section focuses on the density increase, the infiltration setup, the resulting microstructure and the phase composition. Lastly, Section 4-3 covers the infiltration simulations experiments, highlighting the peaks observed in thermogravimetric analysis (TGA) and differential thermal analysis (DTA) analyses, along with the phase composition details. In the discussion (Section 5), reactions are assigned to the peaks observed in the DTA.

### 4-1 Powder bed binder jetting

The PBBJ samples turned light gray after sintering (see Figure 4-1). The mean relative bulk density for samples made with BAK20 powder after sintering is 58.3% with a standard deviation of 1.0% (see Table A-1). The PBBJ samples made and sintered with BAK10 powder achieved a mean relative bulk density of 59.1% with a standard deviation of 0.7%. The X-ray diffraction (XRD) analysis confirmed the presence of only  $\alpha$ -alumina (see Figure A-1).

In Figure 4-2, two sintered infiltration setups are shown. The 3D-printed alumina bodies were cured and debinded together. After debinding, one sample was placed in a closed alumina crucible, while the other remained in an open environment within the sintering oven. The sample in the closed crucible appeared lighter but was still slightly gray (see Figure 4-2).

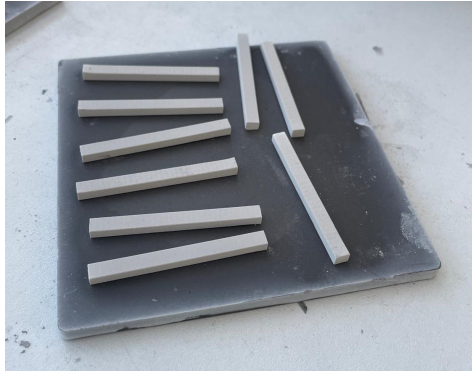


**Figure 4-1:** Sintered samples of alumina bending bars

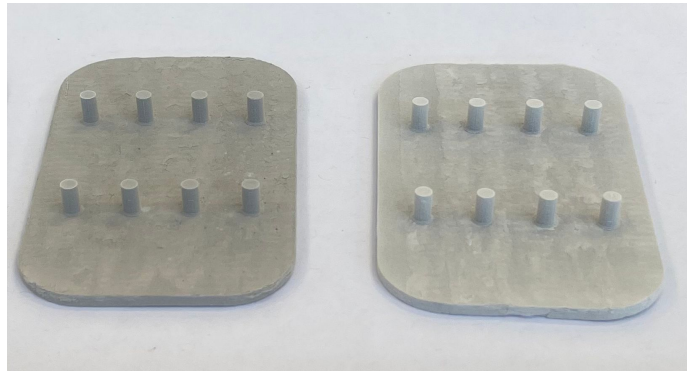


**Figure 4-2:** Left: sample sintered in the oven without an enclosure. Right: sample sintered in the oven with an enclosure

## Microstructure

The microstructure of the sintered porous alumina was characterized using an scanning electron microscope (SEM) and an optical microscope. The SEM image, shown in Figure 4-3, highlights the presence of porosity, though the pores are difficult to distinct. The optical microscope image (Figure 4-4) provides additional clarity on the visibility of the pores. In Figure 4-4, the lightning was adjusted and image editing was done to display the pores in black. This allowed for automated area measurements using the VHX Keyence software, which calculated both maximum and minimum pore diameters.

Using the software, the mean maximum pore diameter was found to be  $9.1 \mu\text{m}$ , with a standard deviation of  $9.8 \mu\text{m}$ . The modal maximum pore diameter was  $2 \mu\text{m}$ . A histogram showing the pore size distribution is presented in Figure 4-5.

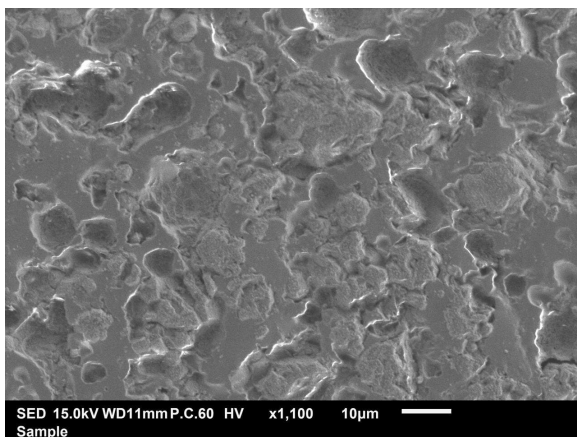


**Figure 4-3:** SEM image of cross section of sintered alumina created by PBBJ in the perpendicular cross section (see Figure 3-13)

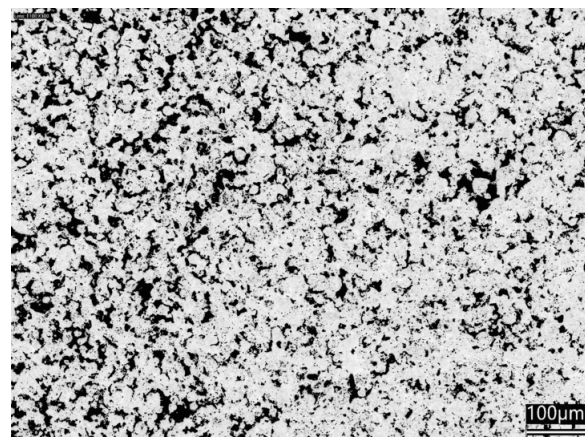


**Figure 4-4:** SEM image of cross section of sintered alumina created by PBBJ in the perpendicular cross section (see Figure 3-13)

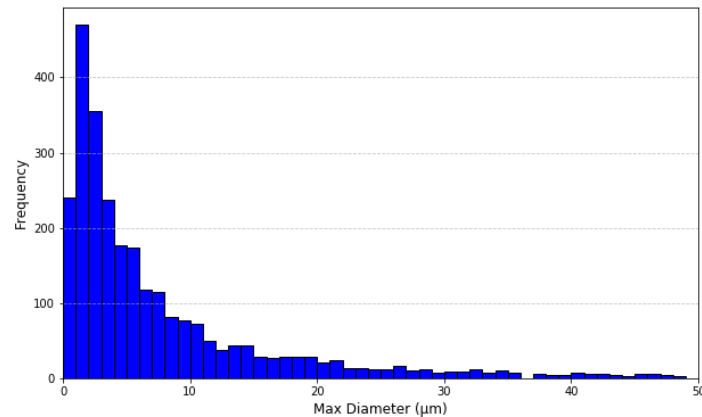


**Figure 4-5:** Histogram of pore maximum diameters determined using VHX Keyence software, with bin width set to 1  $\mu\text{m}$ . The x-axis is limited to 50  $\mu\text{m}$  for clarity.

## 4-2 Infiltration in oxygen

Pressureless infiltration was achieved for infiltrating in an oxygen environment. The samples were infiltrated in  $p_{\text{O}_2}$  of 0.2 atm, 1300°C isotherm for 90 min and 7.5K/min heating rate. The infiltrated bars using infiltration setup B, can be seen in Figure 4-6. To retrieve the samples from the setup, it was possible to push the bars manually by hand of the infiltration pillars. The broken joint left a mark (that can be seen in Figure 4-7). No extra structural damage was observed, other than the mark of the broken joint.

The average density rose after infiltration from 2.3 g/cm<sup>3</sup> to 3.9 g/cm<sup>3</sup> (for data see Table A-3 and Table A-4). Two different infiltration materials were used, namely Cu and Cu<sub>2</sub>O. No significant difference between using Cu powder and Cu<sub>2</sub>O powder was found in the final relative density (<0.5% difference). Infiltration setup B had 4 different columns of infiltration pillars (see Figure 3-9). Each column had 2 or 3 infiltration pillars and each column had a different diameter of the infiltration pillar. No significant difference have been seen in between the relative density achieved after infiltration in between the different columns of infiltration pillars (see Table A-3 and Table A-4). The average relative density after infiltration, calculated with equation 3-4, is 85%. The mean flexural strength was determined to be 53.6 MPa, with a standard deviation of 6.9 MPa.



**Figure 4-6:** infiltrated sample bending bars still attached to infiltration setup, infiltrated in an oxygen rich environment



**Figure 4-7:** Image of a detached bending bar sample that was previously attached to the infiltration setup B. The broken joints are visible in the figure

### Microstructure

A perpendicular cross section was analyzed using an optical microscope. Figure 4-8 shows the perpendicular cross section, where the analyzed surface is located close to the infiltration pillars. As illustrated in Figure 4-8, increased porosity is observed at the location where the infiltration pillar was attached to the sample.

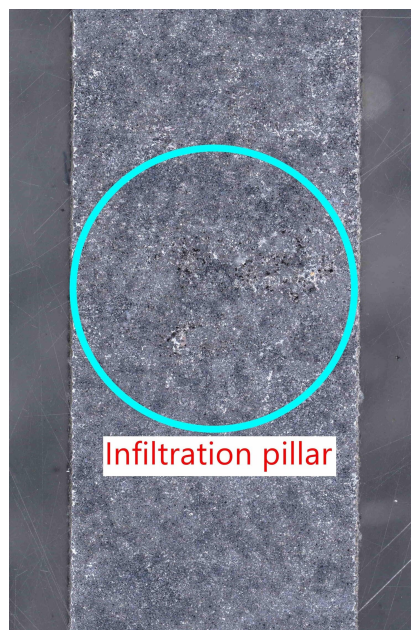


**Figure 4-8:** Optical microscope image of the perpendicular cross section including the location of the infiltration pillar

SEM images of the bulk material from the short parallel cross section cut are shown in Figure 4-9. Porosity is observed throughout the sample, with pores appearing evenly distributed across the cross section. Pore sizes range from 10 to 50 micrometers, with some exceeding this range. Figure 4-10 shows the edge of the sample from the short parallel cross-section.

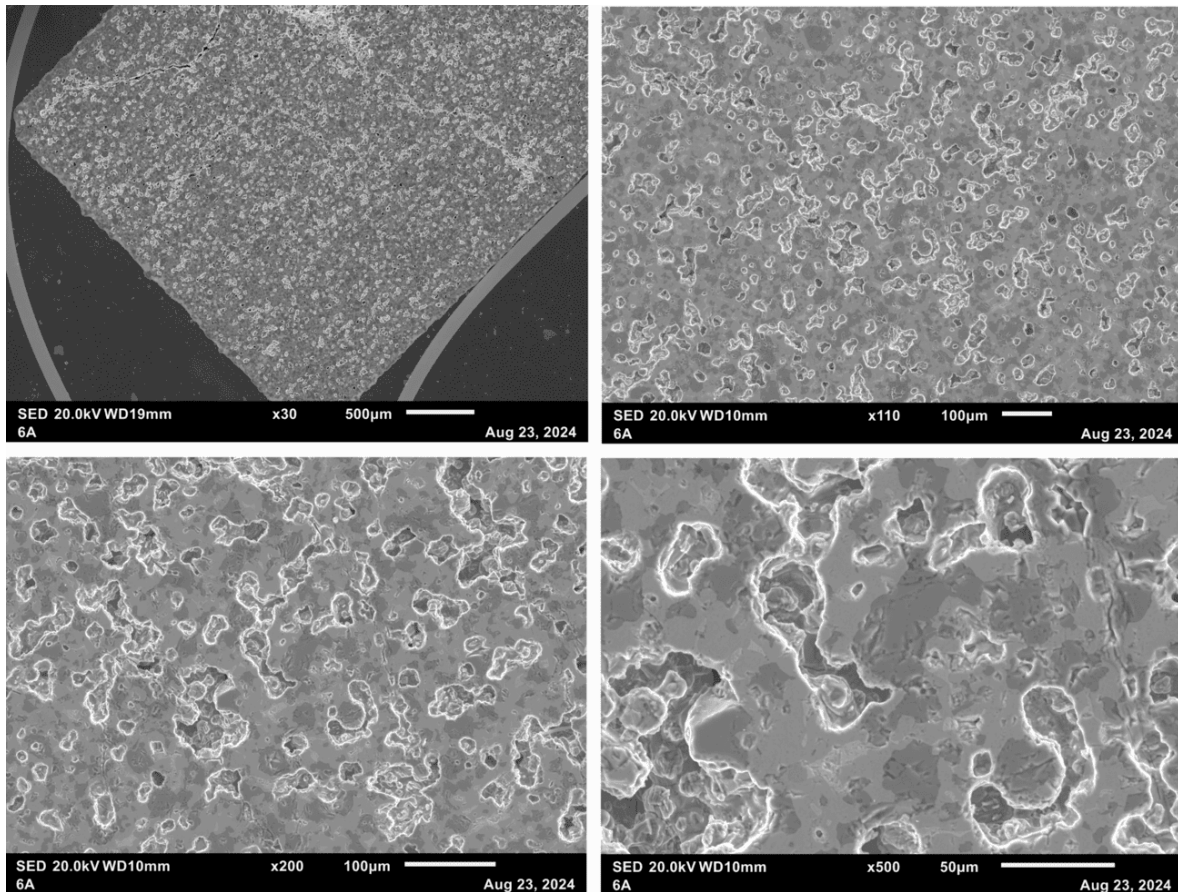


**Figure 4-9:** SEM images of the short parallel cross section bulk of infiltrated porous alumina in an oxygen rich environment

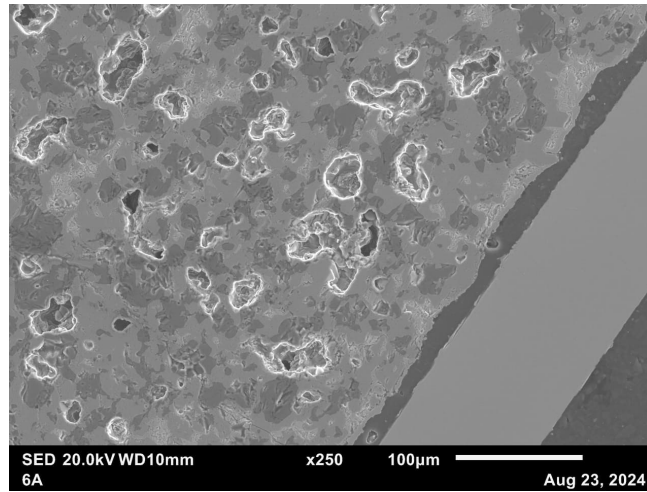


**Figure 4-10:** SEM image of edge of the short parallel cross section of the infiltrated sample alumina porous sample in an oxygen rich environment

An Energy-dispersive X-ray spectroscopy (EDS) map scan was conducted to identify the distribution of elements across different phases. The results of the map scan are shown in Figure 4-11. Four distinct phases, each with a unique visual contrast, were observed: the dark gray phase (labeled A), the medium gray phase (labeled B), the light gray phase (labeled C), and the pores (labeled D). The following items connects the phases to the XRD analysis results, which are presented in Table 4-1.

- The dark gray phase (A) corresponds to alumina ( $\text{Al}_2\text{O}_3$ ). The presence of aluminum and oxygen was detected, but no copper was present.
- The medium gray phase (B) corresponds to a ternary oxide, either  $\text{CuAlO}_2$  or  $\text{AlCuO}_2$ . The presence of aluminum, copper, and oxygen was detected.
- The light gray phase (C) corresponds to copper oxide (either  $\text{Cu}_2\text{O}$  or  $\text{CuO}$ ). It contains copper and oxygen, but no aluminum.
- The pores are indicated with the letter (D). They contain no signal, except for the copper signal.

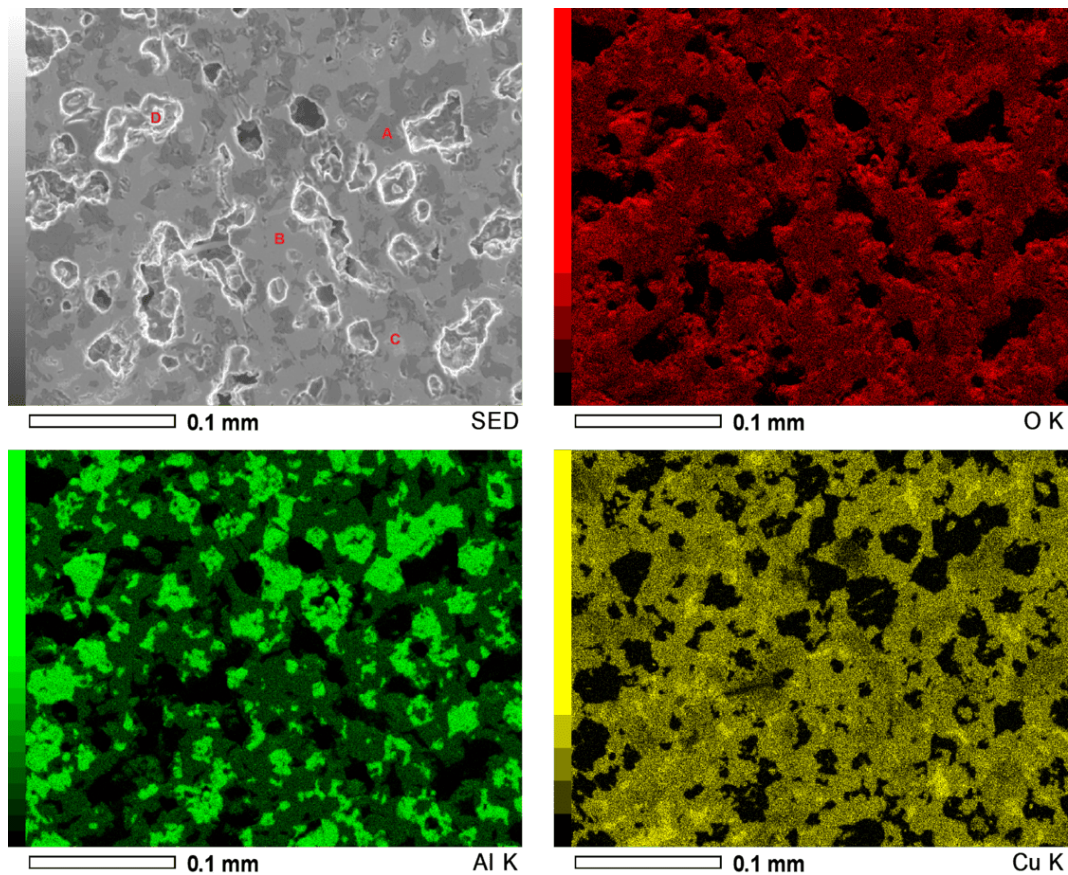


**Figure 4-11:** EDS map scan of porous alumina infiltrated with copper oxide in an oxygen rich environment, analyzed using the short parallel cross section

### Phase composition

An XRD analysis was performed on the powders of two samples infiltrated in an oxygen-rich environment. One sample was infiltrated with Cu starting powder and the other with  $\text{Cu}_2\text{O}$  starting powder. The XRD analysis graph for the Cu powder is shown in Figure A-2 and the graph for the  $\text{Cu}_2\text{O}$  powder is shown in Figure A-3. For the infiltrated samples, five distinct phases were identified: corundum ( $\text{Al}_2\text{O}_3$ ), cuprite ( $\text{Cu}_2\text{O}$ ), tenorite ( $\text{CuO}$ ), copper aluminum oxide ( $\text{CuAlO}_2$ ), and delafossite ( $\text{AlCuO}_2$ ). A Rietveld analysis was conducted to determine the weight percentages of these phases, and the results are presented in Table 4-1. The difference in phase composition between the Cu and  $\text{Cu}_2\text{O}$  starting powders is within a 2% margin.

The amount of alumina decreases significantly during infiltration. Initially, the bending bar sample contained 1.4 grams of alumina (Table A-1). After infiltration, the amount of alumina in the bending bar sample decreases to 0.7 grams. This 0.7 grams corresponds to 25 wt.% of the total weight of 3.9 grams (combining Table A-3 and Table 4-1). This represents a 50% loss of alumina in the bending bar sample.

**Table 4-1:** Rietveld analysis of XRD data for samples infiltrated with different starting powders: one with Cu and the other with Cu<sub>2</sub>O, both in an oxygen-rich environment

Sample	Compound	Wt%
Infiltration with Cu powder	Corundum (Al <sub>2</sub> O <sub>3</sub> )	25
	Cuprite (Cu <sub>2</sub> O)	2
	Tenorite (CuO)	3
	Copper Aluminum Oxide (CuAlO <sub>2</sub> )	67
	Delafossite (AlCuO <sub>2</sub> )	2
Infiltration with Cu <sub>2</sub> O powder	Corundum (Al <sub>2</sub> O <sub>3</sub> )	23
	Cuprite (Cu <sub>2</sub> O)	2
	Tenorite (CuO)	3
	Copper Aluminum Oxide (CuAlO <sub>2</sub> )	69
	Delafossite (AlCuO <sub>2</sub> )	3

### 4-3 Infiltration simulation

In this section, the results of the simulation of infiltration in nitrogen is elaborated. The simulation is done with powder mixtures in an DTA and TGA. These simulations were used to identify the reactions and phase transitions that occur during infiltration. The findings are further discussed in the discussion (chapter 5).

#### 4-3-1 Thermogravimetric analysis (TGA)

A TGA test was conducted to examine any potential mass changes during the heating cycle. In Figure 4-12, the TGA curve of the equimolar mixture (light blue) is shown along with the thermal cycle. A small negative mass change of 1.5 mg is observed, which is less than 1% of the original mass of the equimolar powder mixture (160 mg).

A reference test was also performed using an empty crucible without any powder (see dark blue line in Figure 4-12). This allows a comparison between the data from the crucible containing the equimolar powder mixture and the empty crucible, helping to filter out any instrumental effects. The two curves show a somewhat similar pattern.

To investigate further, the difference between the TGA results of the equimolar mixture and the empty crucible was calculated and plotted (see purple line in Figure 4-13). To highlight the pattern more clearly, the first derivative of the TGA difference was also calculated and plotted (see green line in Figure 4-13). This shows a clear peak in the difference at around 1.25 hours, which corresponds to approximately 330°C.

In Figure 4-14, the TGA and DTA data combined are shown at the moment of weight loss (330°C and 1.25 hours). It can be observed that there is a positive heat flow at this point, indicating exothermic behavior.

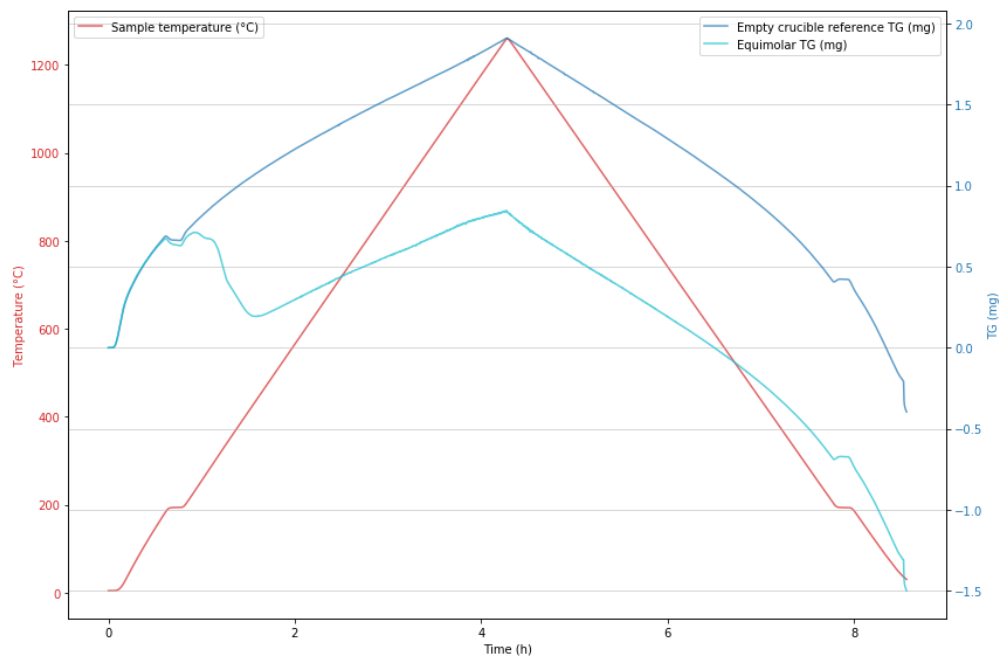


**Figure 4-12:** TGA of the equimolar mixture of  $\text{Al}_2\text{O}_3$  and  $\text{Cu}_2\text{O}$  (light blue) and the TGA of an empty crucible (dark blue) during the thermal cycle of infiltration in an  $\text{N}_2$  environment. Both with an heating rate of 5K/min

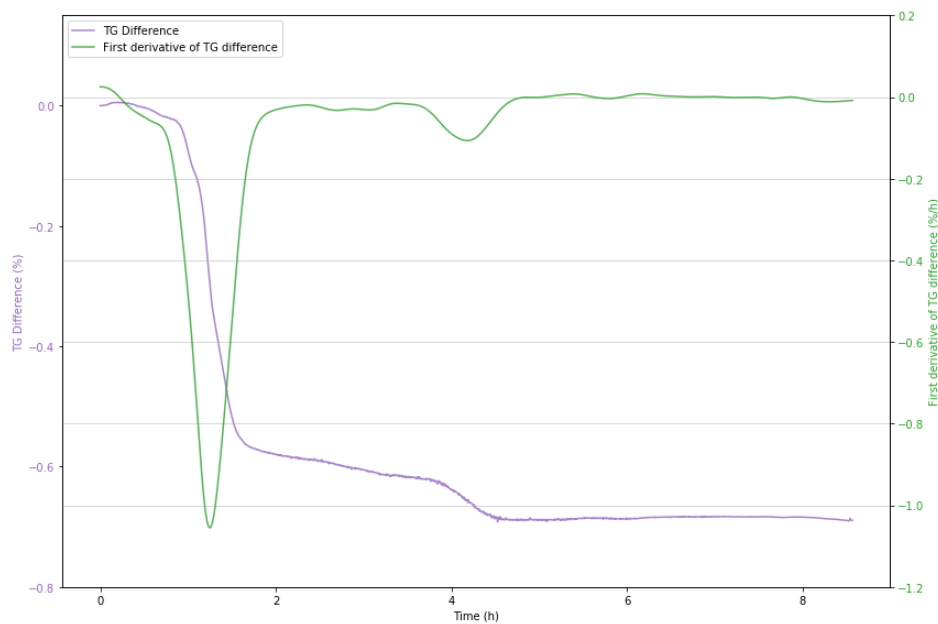


**Figure 4-13:** TG Difference showing the weight change in the TGA during the same thermal cycle, comparing the empty crucible to the crucible with the equimolar powder mixture. The first derivative of the weight difference is plotted as well to highlight the points where the differences between the two TG tests are most significant

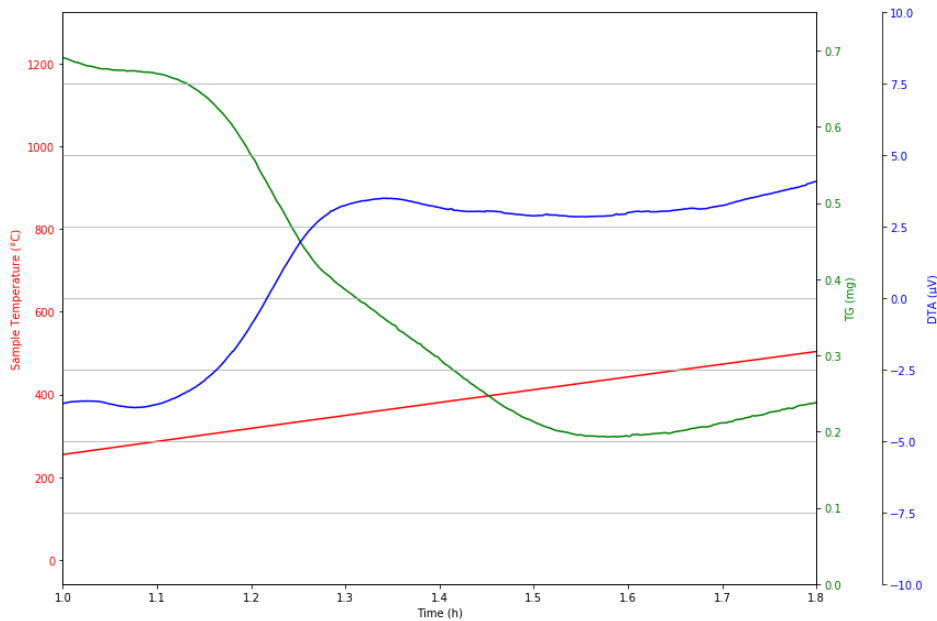


**Figure 4-14:** DTA and TGA of the equimolar mixture of  $\text{Al}_2\text{O}_3$  and  $\text{Cu}_2\text{O}$  during the weight loss phenomenon in an  $\text{N}_2$  environment

#### 4-3-2 Differential thermal analysis (DTA)

DTA results are presented of the equimolar powder mixture in Figure 4-15. The displayed temperature range is limited to 250–1250°C, as the lower temperature zone is assumed to be irrelevant and may be significantly affected by moisture evaporation from the powder mixture. In this figure, multiple peaks are visible, corresponding to various processes occurring throughout the heating cycle. Each peak is marked with a specific peak reference, and the associated peaks are further detailed in this section. In Annex B, the reactions of the peaks are identified based on literature and aligned with the current analysis. This provide an explanation of the processes occurring at each peak.

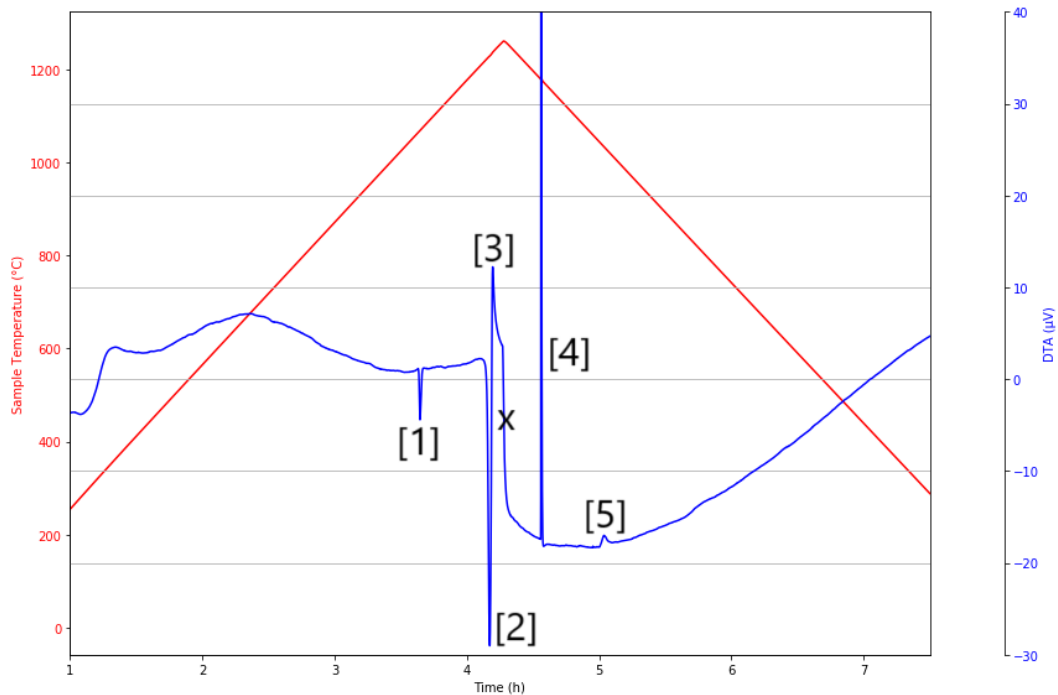


**Figure 4-15:** DTA of equimolar mix of  $\text{Al}_2\text{O}_3$  and  $\text{Cu}_2\text{O}$  in an  $\text{N}_2$  environment with a heating rate of 5K/min

### Peak 1

Peak 1, observed in the DTA analysis, is identified as an endothermic peak ( $\Delta H > 0$ ). It is present in both the DTA graph of the equimolar ( $\text{Al}_2\text{O}_3$  and  $\text{Cu}_2\text{O}$ ) powder mixture and the DTA graph for  $\text{Cu}_2\text{O}$ -only (see Figure 4-16). The values for different thermal cycles and for  $\text{Cu}_2\text{O}$  are summarized in Table 4-2. The heat values of the equimolar sample at 5 K/min and the  $\text{Cu}_2\text{O}$ -only sample at 5 K/min differ by less than 5%.

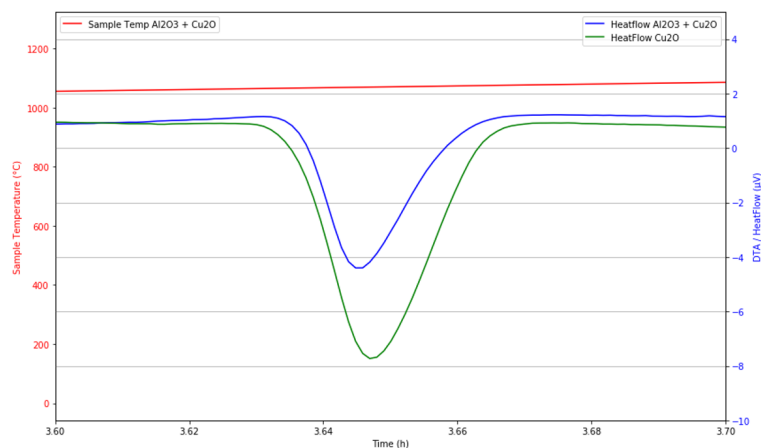


**Figure 4-16:** Close-up view of Peak 1 in the DTA of an equimolar mixture of  $\text{Al}_2\text{O}_3$  and  $\text{Cu}_2\text{O}$  and  $\text{Cu}_2\text{O}$ -only, conducted in a  $\text{N}_2$  environment with a heating rate of 5K/min

**Table 4-2:** Peak 1 \*normalised with factor 1.7

	T <sub>peak</sub> (°C)	Heat ( $\mu\text{V} \cdot \text{s}/\text{mg}$ )	Intensity ( $\mu\text{V}$ )
Equimolar 5K/min	1069	2.0	-6.2
Equimolar 1K/min	1069	1.7	-2.3
Equimolar 10K/min	1068	1.6	-7.1
Cu <sub>2</sub> O only 5K/min *	1069	1.9	-4.9

## Peak 2

Peak 2 is identified as an endothermic peak ( $\Delta H > 0$ ). When comparing the equimolar Al<sub>2</sub>O<sub>3</sub>-Cu<sub>2</sub>O mixture with the Cu<sub>2</sub>O-only sample, the heat of the peak is significantly larger in the Cu<sub>2</sub>O-only sample. The heat of the Cu<sub>2</sub>O-only sample is 2.4 times greater than that of the equimolar mixture under the same heating cycle (based on data Table 4-3). It can be seen in Figure 4-17, that the peaks are shifted.

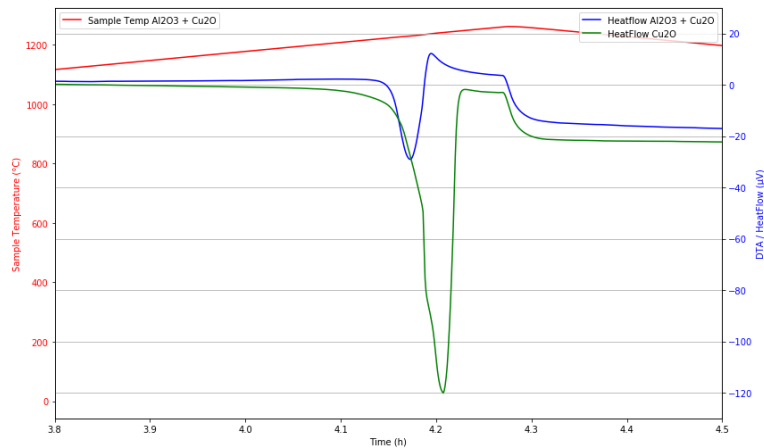


**Figure 4-17:** Close-up view of Peak 2 in the DTA of an equimolar mixture of Al<sub>2</sub>O<sub>3</sub> and Cu<sub>2</sub>O and a mixture of Cu<sub>2</sub>O-only, conducted in a N<sub>2</sub> environment with a heating rate of 5K/min

**Table 4-3:** Peak 2 \*normalised with factor 1.7

	T <sub>peak</sub> (°C)	Heat ( $\mu\text{V} \cdot \text{s}/\text{mg}$ )	Intensity ( $\mu\text{V}$ )
Equimolar 5K/min	1230	19.2	-35.4
Equimolar 1K/min	1227	16.8	-12.2
Equimolar 10K/min	1231	18.6	-47.2
Cu <sub>2</sub> O only 5K/min *	1236	46.2	-62.1

### Peak 3

In the DTA that includes the equimolar mixture, an exothermic peak is observed (at peak 3 location). In the mixture of  $\text{Cu}_2\text{O}$ -only, the exothermic peak is not observed. In Figure 4-18 and Figure 4-19, the position of Peak 3 is marked by a green arrow. In Table 4-4, the data from the DTA can be seen.

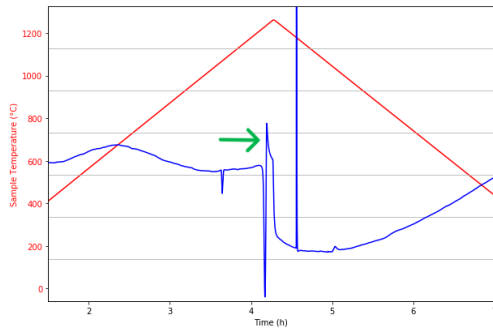


**Figure 4-18:** DTA of equimolar mixture of  $\text{Al}_2\text{O}_3$  and  $\text{Cu}_2\text{O}$  in an  $\text{N}_2$  environment with a heating rate of 5K/min

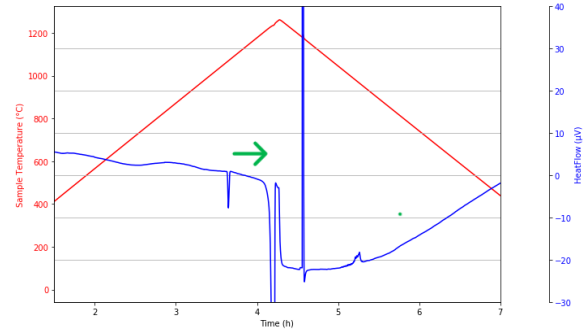


**Figure 4-19:** DTA of equimolar mixture of  $\text{Al}_2\text{O}_3$  and  $\text{Cu}_2\text{O}$  in an  $\text{N}_2$  environment with a heating rate of 5K/min

**Table 4-4:** Peak 3 \*normalized with factor 1.7

	T <sub>peak</sub> (°C)	Heat ( $\mu\text{V} \cdot \text{s}/\text{mg}$ )	Intensity ( $\mu\text{V}$ )
Equimolar 5K/min	1237	-2.6	8.3
Equimolar 1K/min	1232	-1.8	2.3
Equimolar 10K/min	1242	-1.9	7.7
$\text{Cu}_2\text{O}$ only* **	N/A	N/A	N/A

### Peak 4

Peak 4 is an exothermic peak. Comparing the equimolar mixture and the  $\text{Cu}_2\text{O}$ -only mixture (see Figure 4-20), the peak in the  $\text{Cu}_2\text{O}$  sample is significantly stronger. As shown in Table 4-5, the heat released by  $\text{Cu}_2\text{O}$  is 4.8 times greater than that of the equimolar mixture. The peaks are also slightly shifted.

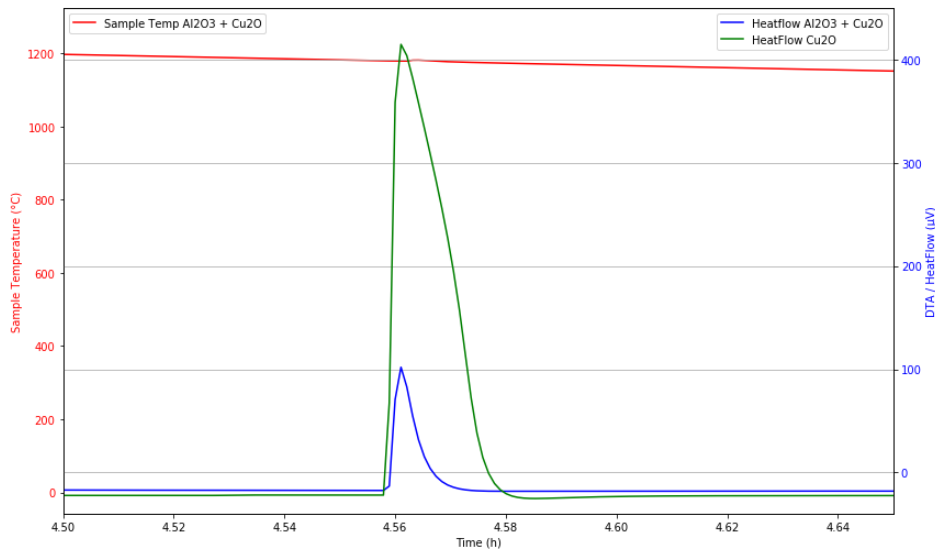


**Figure 4-20:** Close-up view of Peak 5 in the DTA of an equimolar mixture of  $\text{Al}_2\text{O}_3$  and  $\text{Cu}_2\text{O}$  and a mixture of  $\text{Cu}_2\text{O}$ -only, conducted in a  $\text{N}_2$  environment with a heating rate of 5K/min

**Table 4-5:** Peak 4 \*normalized with factor 1.7

	T <sub>peak</sub> (°C)	Heat ( $\mu\text{V} \cdot \text{s}/\text{mg}$ )	Intensity ( $\mu\text{V}$ )
Equimolar 5K/min	1174	-10.9	109
Equimolar 1K/min	1166	-6.3	65
Equimolar 10K/min	1179	-11.8	117
$\text{Cu}_2\text{O}$ only*	1180	-52.1	237

## Peak 5

In Figure 4-21, the DTA curves of both the  $\text{Cu}_2\text{O}$ -only sample and the equimolar mixture are displayed, revealing distinct peaks at different temperatures with varying shapes. This observation indicates that peak 5 consists of two separate peaks. Further analysis in Figure 4-22, which shows the DTA curve of the equimolar mixture with a slow heating rate (1 K/min), verifies that Peak 5 consists of two distinct peaks, labeled as peaks 5.1 and 5.2. The temperatures and shapes of these peaks in Figure 4-22 correspond to those in Figure 4-21, confirming the identification of peaks 5.1 and 5.2. The peak temperature of Peak 5.1 is around 1060°C and the peak temperature of Peak 5.2 is around 1030°C.

These two peaks (5.1 and 5.2) are also present in the DTA of the equimolar mixture where an isotherm of 30 minutes at 1250°C was maintained (see Figure A-5). Additionally, they were observed in the equimolar mixture with a faster heating rate (see Figure A-6). However, only Peak 5.2 was identified in the DTA analysis of the  $\text{Cu}_2\text{O}$ -only sample (see Figure A-8 and Figure A-9).

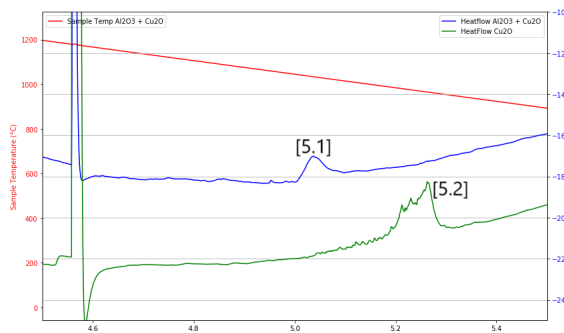


**Figure 4-21:** Peak 5 indication in both the DTA of the  $\text{Cu}_2\text{O}$  and the  $\text{Cu}_2\text{O}$  and  $\text{Al}_2\text{O}_3$  equimolar powder mixtures in an  $\text{N}_2$  environment

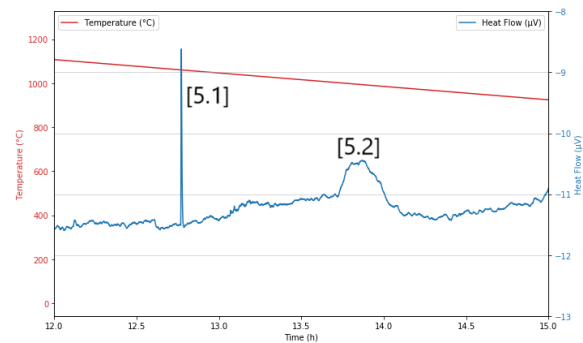


**Figure 4-22:** Peak 5 indication in the DTA of the equimolar mixture  $\text{Cu}_2\text{O}$  and  $\text{Al}_2\text{O}_3$  with a slow heating rate of 1K/min in an  $\text{N}_2$  environment

## Peak x

Peak x is a negative heat flow shift observed in both the DTA tests for the equimolar mixture and the  $\text{Cu}_2\text{O}$ -only powder (see Figure 4-15). The peak intensity is similar for both the equimolar mixture and the  $\text{Cu}_2\text{O}$ -only powder under the same heating rate.

The peak occurs precisely at  $1250^\circ\text{C}$ , corresponding with the transition point of the thermal cycle from heating to cooling. In Figure 4-23, the vertical dashed line indicates the point where the heating rate changes from heating to cooling. In the DTA, when the equimolar mixture was heated to  $1400^\circ\text{C}$ , the negative heat flow shift was observed at the transition point of  $1400^\circ\text{C}$  (see Figure A-10).

In the test with the equimolar mixture where an isotherm is maintained, the negative heat flow shift is divided into two sections. The first shift occurs when the temperature transitions from heating to the isotherm, while the second shift occurs when the temperature transitions from the isotherm to cooling. The results of this test, with dashed lines indicating the heating rate changes, are shown in Figure 4-24.

When a higher heating rate difference occurs, the negative heat flow shift at Peak x becomes more pronounced. This is evident in Figure A-6, which shows the results of the DTA conducted with a heating rate of  $10\text{ K/min}$ . Conversely, a lower heating rate difference leads to a smaller negative heat flow shift. This can be observed in Figure A-7, where the same DTA was performed with a heating rate of  $1\text{ K/min}$ . All experiments referenced in this section were conducted using the same equimolar mixture.

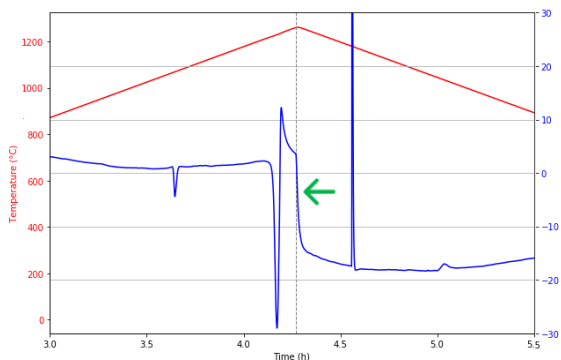


**Figure 4-23:** DTA of an equimolar mixture of  $\text{Al}_2\text{O}_3$  and  $\text{Cu}_2\text{O}$ , conducted in a  $\text{N}_2$  environment with a heating rate of  $5\text{ K/min}$ . The vertical dashed line indicate the switch from heating to cooling

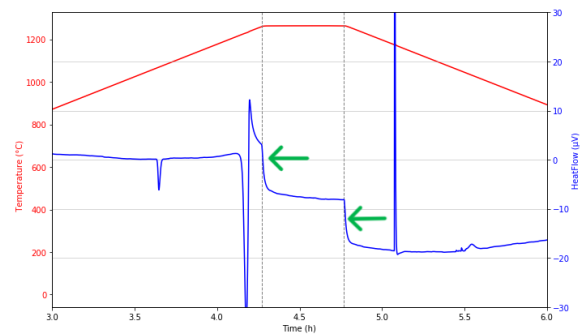


**Figure 4-24:** DTA of an equimolar mixture of  $\text{Al}_2\text{O}_3$  and  $\text{Cu}_2\text{O}$ , conducted in a  $\text{N}_2$  environment with a heating rate of  $5\text{ K/min}$ . An isotherm is reached for 30 minutes at  $1250^\circ\text{C}$ . The vertical dashed lines indicate the switch from heating to isothermal and from isothermal to cooling

### 4-3-3 X-ray diffraction (XRD)

An XRD analysis was performed on the crushed crucibles used during the DTA tests. The results of the XRD-Rietveld analysis were scaled (for scaling see Section 3-3). The scaled values, which provide clarity about the contents of the crucibles, are presented in Table 4-6.

For the test with Cu<sub>2</sub>O-only, all the alumina phase was subtracted, and the remaining values were similarly scaled back to 100%. The original results from the XRD-Rietveld analysis are provided in Table A-5. In every XRD analysis, some percentages silicon was detected. This was also subtracted, as it was not part of the equimolar mixture or the Cu<sub>2</sub>O-only mixture.

**Table 4-6:** Scaled XRD Rietveld analyse results of the crushed alumina crucibles of the DTA tests

Sample	Compound	Wt%
Equimolar, 5K/min, 1250 °C, 30 min isotherm	Copper Aluminum Oxide (CuAlO <sub>2</sub> )	87
	Copper (Cu)	3
	Cuprite (Cu <sub>2</sub> O)	3
	Corundum (Al <sub>2</sub> O <sub>3</sub> )	8
Equimolar, 1K/min, 1250 °C, 30 min isotherm	Copper Aluminum Oxide (CuAlO <sub>2</sub> )	88
	Copper (Cu)	2
	Cuprite (Cu <sub>2</sub> O)	1
	Corundum (Al <sub>2</sub> O <sub>3</sub> )	9
Equimolar, 10K/min, 1250 °C, 30 min isotherm	Copper Aluminum Oxide (CuAlO <sub>2</sub> )	82
	Copper (Cu)	2
	Cuprite (Cu <sub>2</sub> O)	4
	Corundum (Al <sub>2</sub> O <sub>3</sub> )	11
Equimolar, 10K/min, 1250 °C, no isotherm	Copper Aluminum Oxide (CuAlO <sub>2</sub> )	73
	Copper (Cu)	2
	Cuprite (Cu <sub>2</sub> O)	5
	Corundum (Al <sub>2</sub> O <sub>3</sub> )	20
Cu <sub>2</sub> O-only, 5K /min, 1250 °C, 30 min isotherm	Copper Aluminum Oxide (CuAlO <sub>2</sub> )	33
	Copper (Cu)	17
	Cuprite (Cu <sub>2</sub> O)	50
Equimolar, 5K/min, 1400 °C, 30 min isotherm	Copper Aluminum Oxide (CuAlO <sub>2</sub> )	57
	Copper (Cu)	5
	Cuprite (Cu <sub>2</sub> O)	7
	Corundum (Al <sub>2</sub> O <sub>3</sub> )	31

---

# Chapter 5

---

## Discussion

The discussion elaborates on the following aspects: the effects of powder bed binder jetting (PBBJ) and sintering conditions, the effects of infiltration on densification and material properties, the effects of the infiltration environment and compliance with ASML standards.

### 5-1 Effects of powder bed binder jetting and sintering conditions

The results show that the bulk density of PBBJ alumina was 58.3% for BAK20 and 59.1% for BAK10. These values are comparable to findings from other studies that utilized a unimodal alumina powder in combination with PBBJ. A comparison with the literature is displayed in Figure 5-1.

No strength measurements were performed on the porous alumina structures, as it was deemed irrelevant due to the high level of porosity in the samples. From Table 2-3, it can be observed that alumina with a porosity of around 40%, the flexural strength is approximately 55 MPa. This aligns with the study by A.K. Mohan, a flexural strength of 59.5 MPa was achieved with a porosity of 33.1% [34]. Based on these findings, the flexural strength of alumina produced by PBBJ in this study is assumed to be less than 60 MPa.

The maximum pore size distribution has similarities with a Poisson distribution. The calculated infiltration time (equation 3-3) may lack accuracy due to the wide pore size distribution. For the calculations the mean of the maximum pore size as used. The modal pore size is 2  $\mu\text{m}$ , while the mean value used in calculations, is 9  $\mu\text{m}$ . Using the modal pore size, the infiltration time would be around 80 seconds. This difference is considered insignificant.

The sintered samples were expected to be white, but instead they were light gray. This discoloration is suspected to be caused by environment of the sintering oven. To investigate the oven's influence on the color change, an experiment was performed where one sample was sintered inside an enclosure while another was left exposed to the sintering ovens environment (see Figure 4-2). The sample inside the enclosure had a lighter gray color in comparison with the sample that was without enclosure. This indicates that the sintering oven environment

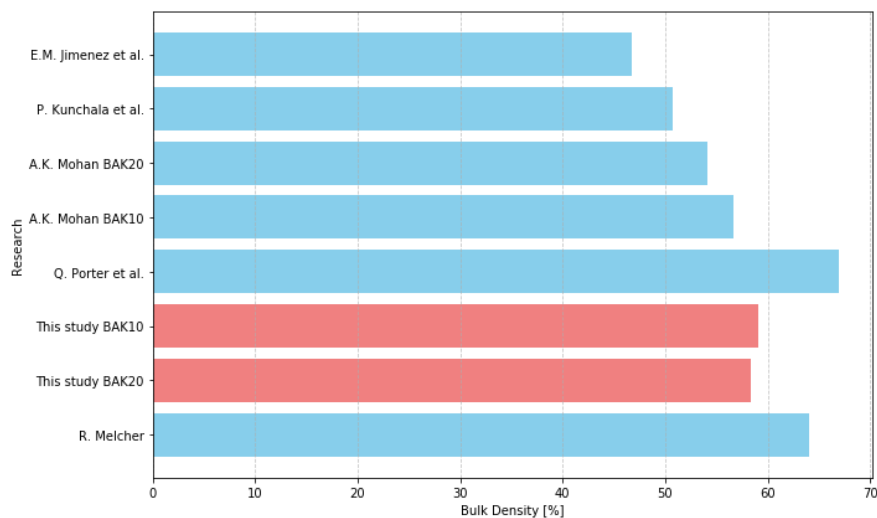


**Figure 5-1:** Bulk density comparison of porous alumina bodies created by PBBJ. The data includes results from various studies, highlighting this study in red. [32, 24, 42, 34, 30]

likely contributes to the discoloration. However, the enclosed sample still has a color change, as the final sintered product was not as white as the original alumina powder used for PBBJ. No carbon contamination is assumed to be present, as heating the samples in the presence of  $O_2$ , did not give any color change. X-ray diffraction (XRD) analysis identified only  $\alpha$ -alumina in the samples. This implies that, if contaminants are responsible for the gray color, their concentration is minimal. It is assumed that this contamination has little impact on wetting. As shown in the EDS map scan (see Figure 5-4), alumina still bonds well with the other phases. Note: other characterization methods are more suitable for detecting elemental contamination in trace amounts (like XRF) [43]. However, they were not used in this study. The change in color of alumina could be caused by contamination with metal oxides [44]. This may originate from the sintering oven, which is also used for sintering stainless steel 316L. Metal oxides from these previous processes might have contaminated the oven. This contamination could have ended up in the alumina in trace amounts. This issue remains open due to the lack of further investigation and the absence of elements other than alumina in the XRD analysis

## 5-2 Effects of infiltration on densification and material properties

Pressureless infiltration was successfully applied to porous alumina samples produced using PBBJ, resulting in an increase in relative bulk density from 58% to 85%. The flexural strength after infiltration was 53.6 MPa. Compared to existing literature on PBBJ alumina, including studies that incorporate optional post-processing steps, the performance achieved in this research is relatively modest. This comparison is illustrated in Figure 5-2. The suboptimal strength is likely due to the reaction between copper oxide and alumina. Since alumina is the main load-bearing structure, the consumption of alumina during the infiltration cycle lowers the composite's mechanical properties. This theory is substantiated by the rule of mixtures.

Infiltration set-up B was successful in retrieving intact infiltrated bending bar samples. Post-

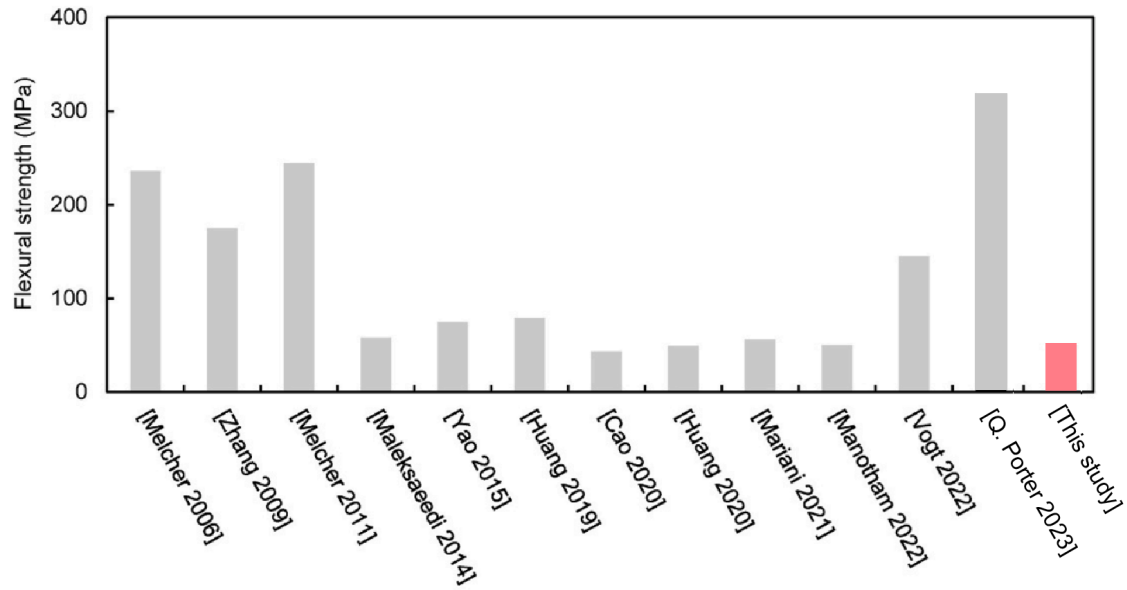


**Figure 5-2:** Comparison of the flexural strengths of alumina-based specimens fabricated by PBBJ, followed by sintering and optional post-processing. The red bar indicates the flexural strength of porous alumina created by PBBJ and subsequently infiltrated with copper (oxide) in an oxygen rich environment [42]

infiltration, the bending bar samples could be easily removed manually. It is presumed that bonding occurred solely through a mechanical inferior copper oxide joint, as there was no initial mechanical connection between the alumina parts. This is because the porous alumina samples were simply placed on top of the infiltration pillars. This allowed for easy detachment from the pillars, with no observable structural damage to the bending bar samples.

There was no difference in density among the four columns of infiltration pillars. Therefore, infiltration column (A) (see Figure 3-9) is regarded as the best. This column has only two pillars with the smallest diameter (2 mm). As a result, the bending bar was the easiest to remove, with minimal surface damage at the broken joint (see Figure 4-7).

Two different powders were used as infiltration materials: copper and copper oxide ( $\text{Cu}_2\text{O}$ ). Copper was chosen because it was used in the study by Q. Porter et al. [42], where a fully ceramic composite with favorable mechanical properties was made. Copper oxide ( $\text{Cu}_2\text{O}$ ) was included to investigate whether differences in infiltration characteristics, such as density and phase composition, could be observed. A potential difference in infiltration characteristics could have arisen, because copper must first absorb oxygen before it can effectively wet the alumina (see section 2-2-2). However, no significant differences in relative density or phase composition were observed between the samples infiltrated with copper powder and those infiltrated with copper oxide ( $\text{Cu}_2\text{O}$ ), as shown in Table 4-1. Therefore, it is assumed that the copper had enough time to fully oxidize prior to infiltration.

In the scanning electron microscope (SEM) images, it was observed that the pores are distributed throughout the entire cross section, except at the edge of the sample (see Figure 4-9 and Figure 4-11). At the edge of the sample, the light gray phase was identified in the Energy-dispersive X-ray spectroscopy (EDS) scan. This light phase corresponds to copper oxide. In

Figure 4-6, the samples appear dark gray in reality. Since cuprous ( $\text{Cu}_2\text{O}$ ) has a brown-red color and tenorite ( $\text{CuO}$ ) has a dark gray/black color, it is presumed that the sample is covered with  $\text{CuO}$  after infiltration. The volume increase after infiltration ranges from 0 to 3 vol.%, which can be attributed to the added copper oxide layer. However, measurement errors also contribute to this variation.

The EDS analysis (Figure 4-11) shows that the pores share boundaries with both the alumina phase and the ternary oxide phase. From Figure A-10 could be derived that the melting point of the ternary oxide was determined to be approximately  $1280^\circ\text{C}$ . This indicates that the ternary oxide was in a liquid phase at the infiltration temperature of  $1300^\circ\text{C}$ . Since the liquid phase is connected to pores, it suggests that the pores are not closed pores. If it were closed pores, it would be entirely surrounded by the alumina phase. This indicates potential for further densification. A plausible explanation why no further infiltration occurred is the significant reduction in the alumina structure. This reduction increased the distance between the alumina phases. Additionally, the formation of a thick ternary oxide reaction layer could have hindered wetting by the copper oxide. Resulting in the pores not being fully filled by a liquid phase. This hypothesis is based on observation and is not currently supported by literature or scientific data.

In Section 4-2, it was shown that copper oxide reacts with alumina at high rates. The amount of alumina in the bending bar decreases by 50 wt.% during infiltration. This conversion could be explained by section 2-2-3. In this section in the chemical analysis, it can be observed that copper oxide and alumina begin reacting with each other in an oxygen rich environment at temperatures as low as  $600$  to  $700^\circ\text{C}$ . It is now clear that the reaction rates are too high to produce a composite with good mechanical properties. This can be explained by, as discussed in Section 2-2-3 in the mechanical analysis, the rule of mixture. The rule of mixture suggests that as much alumina as possible must be preserved to get the highest mechanical performing material. However, in this study, a substantial 50% reduction in alumina content was observed, which severely reduced the composite's mechanical performance.

When comparing the results with other research where copper (oxide) was infiltrated into an alumina porous structure, the flexural strength of 53.6 MPa observed in this study is significantly lower than the 317.5 MPa reported by Q. Porter et al. [42]. In their study more alumina was preserved (see Figure 5-3) and a higher density was reached. No aluminum elements can be detected in the copper rich phases. This contrasts with the EDS map in this study (Figure 5-4), where aluminum in copper-rich phases indicates ternary oxide formation, unlike the minimal ternary oxides reported by Q. Porter et al.

A key difference may be the oxygen availability in the oven used. They started with copper powder, which consumed oxygen as it oxidized. The hypothesis is that the oxygen content reduced in their oven to a minimal level where not further copper oxidized. As detailed in Section 2-2-2, copper can already wet alumina with an oxygen content of 0.8 wt.%. The lower oxygen content in their infiltrated phase minimized the reactions between copper oxide and alumina, thereby preserving the alumina. This preservation of alumina likely contributed to the superior strength observed in their study. Further evidence suggests that the infiltrated copper in Q. Porter's samples was primarily metallic, as indicated by oxygen-free copper areas in Figure 5-3. This aligns with findings from R. Melcher et al., who reported a flexural strength of 245 MPa when infiltrating porous alumina with a copper melt containing 3.2 wt.% oxygen. Their strength value is closer to that of Q. Porter et al. than this study [31].

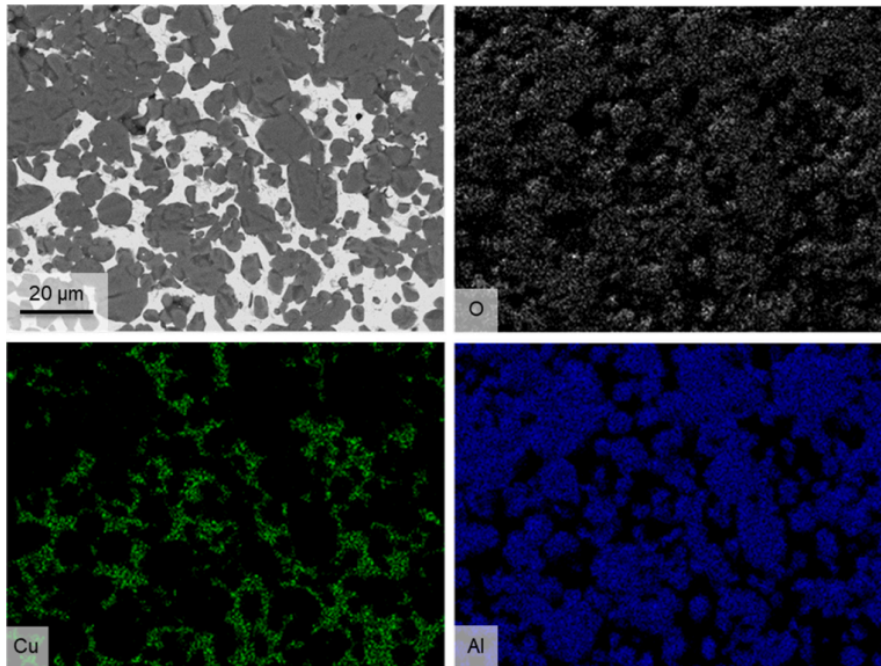


**Figure 5-3:** Elemental maps from EDS for an infiltrated specimen made [42]

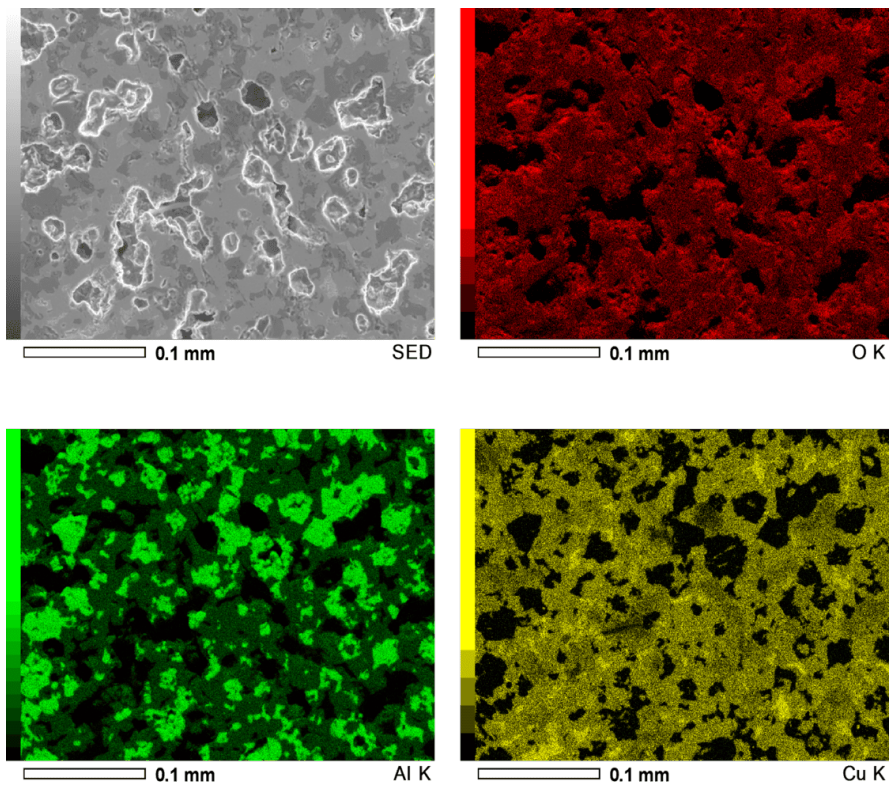


**Figure 5-4:** EDS map scan of porous alumina infiltrated with copper oxide in an oxygen rich environment, analyzed using the short parallel cross section

### 5-3 Effects of infiltration environment

Infiltration in an oxygen environment results in significant reactions, leading to the consumption of approximately half of the alumina. As shown in Figure 2-13, the phase transition between alumina and copper oxide in nitrogen occurs at a onset higher temperature, with slower reaction kinetics. This suggests that infiltrating in a nitrogen environment could be more favorable. Before proceeding with infiltration in a nitrogen environment, it is essential to understand the reactions occurring during a thermal infiltration cycle. A review of the literature did not reveal this information. Therefore, this section examines the phase transitions in a nitrogen environment to provide this understanding using differential thermal analysis (DTA), thermogravimetric analysis (TGA) and XRD. The peaks and their proposed reactions are presented in Figure 5-5. These reactions were determined through a combination of peak comparisons between DTA, TGA, and XRD data, observations and information available in the literature. The detailed derivation process of determining the reactions is provided in Annex B.

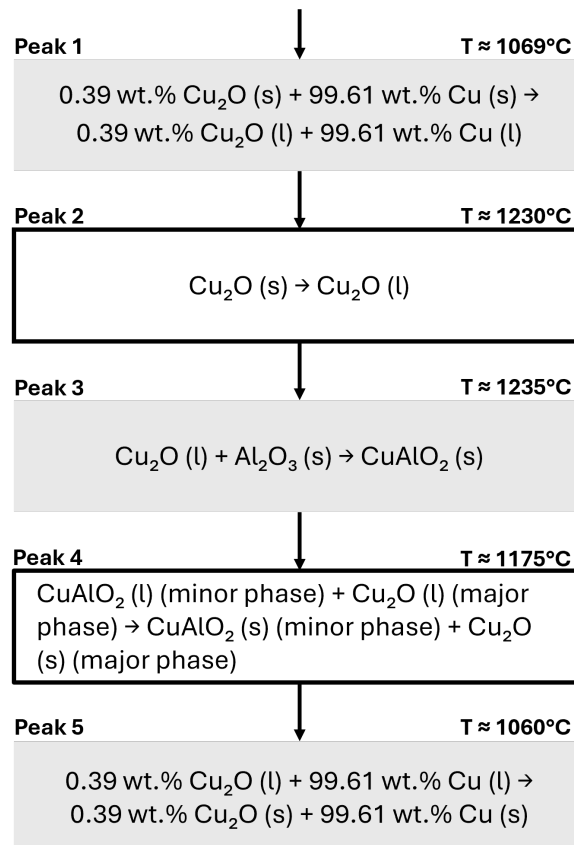


**Figure 5-5:** Phase transitions during the thermal cycle of the equimolar mixture of  $\text{Al}_2\text{O}_3$  and  $\text{Cu}_2\text{O}$  in nitrogen

In order to create a high-performance mechanical composite the challenge is to minimize the formation of ternary oxides and thereby reduce the consumption of alumina (the load bearing structure). In Figure 5-5, it can be seen that the ternary oxide ( $\text{CuAlO}_2$ , delafossite) forms at peak 3 at  $1235^\circ\text{C}$ . In contrast, section 2-2-3 notes that delafossite can already start forming in solid-state at around  $900 - 1100^\circ\text{C}$  [3]. But why do we see this significant peak at  $1235^\circ\text{C}$  and not earlier? The hypothesis is that the delay arises from the limited contact area between  $\text{Cu}_2\text{O}$  and  $\text{Al}_2\text{O}_3$  powders prior to melting. Before  $\text{Cu}_2\text{O}$  melts, contact between the  $\text{Cu}_2\text{O}$  and  $\text{Al}_2\text{O}_3$  powders is minimal, restricting reaction kinetics to limited points of contact. However, once  $\text{Cu}_2\text{O}$  melts, it wets the alumina, encircling the  $\text{Al}_2\text{O}_3$  particles and significantly increasing the surface area available for reaction. This enhanced contact area promotes more extensive delafossite formation, explaining the increased intensity of the exothermic peak observed. This process is schematically illustrated in Figure 5-6.

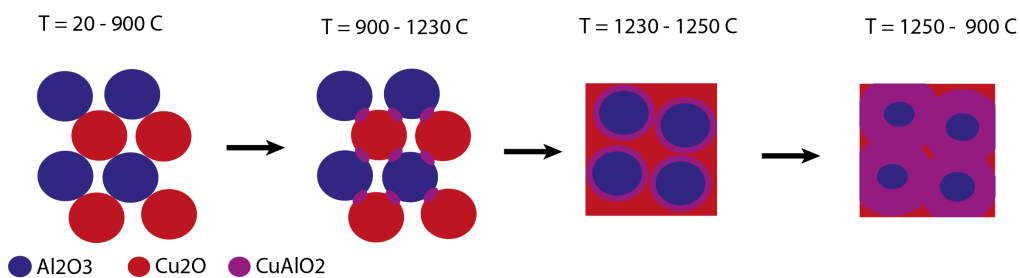


**Figure 5-6:** Schematic overview on the formation of delafossite in a powder analysis

Can we detect the solid-state reactions of the formation of the delafossite in the DTA analysis? First it is important to know when the system is in liquid-solid state or in solid-state. This is displayed in Figure 5-7, where the DTA graphs of the equimolar mixture and the  $\text{Cu}_2\text{O}$ -only mixture are plotted together. Once  $\text{Cu}_2\text{O}$  has melted, the reactions occur in a liquid-solid state. The difference between the equimolar mixture and the  $\text{Cu}_2\text{O}$ -only mixture becomes larger, indicated by the pink arrow (see Figure 5-7). This increase in reaction intensity is matching the previous section's explanation of melting and wetting, where more surface area is available for reactions.

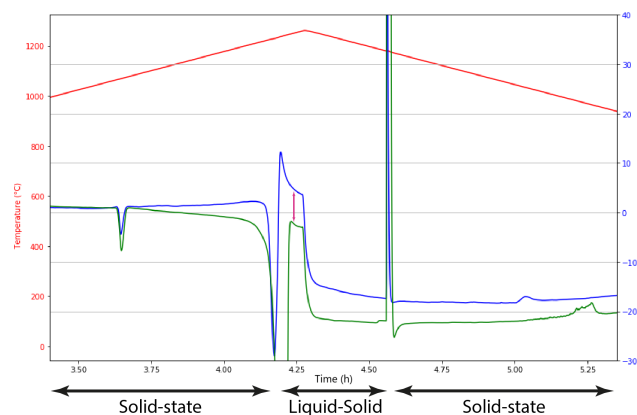


**Figure 5-7:** Graph comparing the DTA of an equimolar mixture and a  $\text{Cu}_2\text{O}$ -only mixture, highlighting three distinct regions: solid-state, liquid-solid and a again solid-state. The purple arrow indicates the difference between the equimolar mixture and the  $\text{Cu}_2\text{O}$ -only mixture

It's important to remember that the formation reaction of the delafossite is exothermic. The reaction kinetics in solid-state appear to increase with temperature, marking the the exothermic trend by the yellow arrow in Figure 5-8. The peak intensity is less than 10% compared to that of peak 3, suggesting that solid-state reactions play a minimal role.

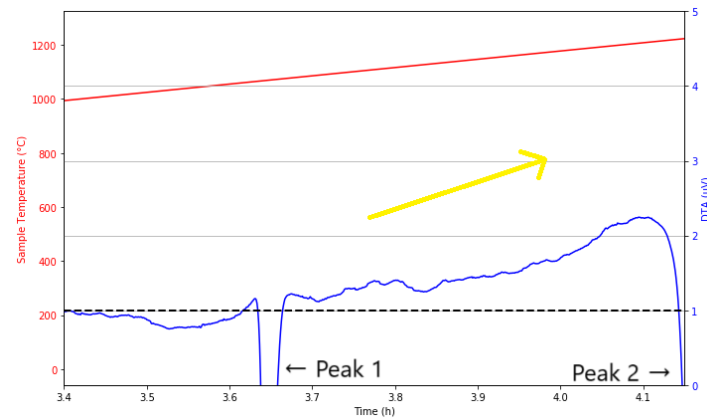


**Figure 5-8:** DTA of an equimolar mixture of  $\text{Al}_2\text{O}_3$  and  $\text{Cu}_2\text{O}$ . The yellow arrow indicated the hypothesized exothermic behaviour of the formation of delafossite in solid-state

To minimize the formation of the ternary oxide, it is crucial to reduce or prevent the occurrence of peak 3. This can be achieved by limiting the reaction kinetics between alumina and copper oxide. A solution could be lowering the infiltration temperature, potentially to a point below where alumina and copper oxide react. However, in order to make this work, the copper oxide should be doped with other elements to reduce this melting temperature. Another solution could be reducing the duration spent in the liquid-solid state, where peak 3 takes place. This could reduce the amount of ternary oxide being formed during infiltration.

The latest hypothesis, where the time stayed in the liquid-solid state is minimized, is discussed in this section. In Figure A-6, the DTA results are shown for an experiment designed to minimize the formation of ternary oxide using the knowledge gained so far. The peak temperature of  $1250^\circ\text{C}$  was chosen close to the melting temperature of copper oxide ( $1230^\circ\text{C}$ , identified in Peak 2). The heating and cooling rates were set to the maximum allowed by the equipment ( $10\text{ K/min}$ ) and no isotherm was maintained. This was done to minimize the time spent in the liquid-solid state. The phase composition of the mixture is presented in Table 4-6.

The results indicate that less ternary oxide was formed under these conditions, with approximately  $(87 - 73)/87 \times 100 = 16\%$  less ternary oxide compared to the  $5\text{ K/min}$  heating cycle with a 30-minute isotherm. However, a significant amount of ternary oxide (72%) still formed, leading to the consumption of alumina. This suggests that infiltration with this fast thermal infiltration cycle must be further optimized to reduce the amount of ternary oxide being formed. It should be noted that this is an equimolar mixture and during infiltration other ratios could be used.

To understand how fast the process needs to be to avoid this, it is helpful to focus further on peak 3. In Figure 5-9, the width of Peak 3 is observed to be approximately 6 minutes, with a gradual decay continuing afterward. The intensity in the DTA correlates with the reaction rate [60]. For Peak 3, the steep left side of the slope indicates that copper oxide

rapidly wets the alumina, utilizing a large surface area and resulting in a high reaction rate. Consequently, a reaction layer forms. To continue reacting, the copper oxide must diffuse through this layer, slowing the process and explaining the non-linear decay observed after Peak 3 (see Figure 5-9). This non-linear decay could be described by diffusion models [48]. Due to time constraints, modeling these kinetics was not feasible. However, an insight was given that a lot of reactions are happening in the first minutes after the copper oxide wets the alumina.

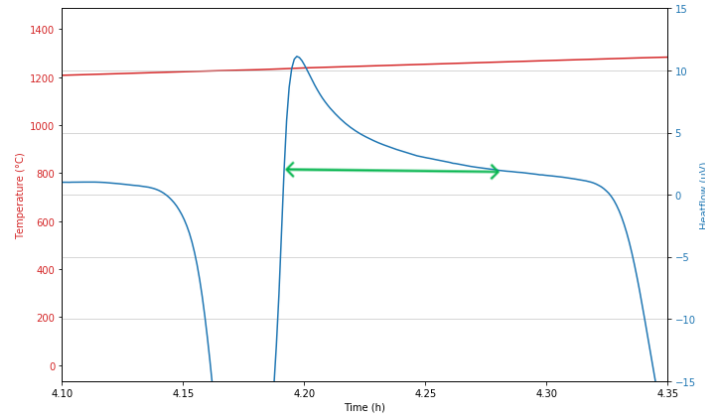


**Figure 5-9:** DTA of equimolar mix of  $\text{Al}_2\text{O}_3$  and  $\text{Cu}_2\text{O}$  in an nitrogen environment with a heating rate of 5K/min and a peak temperature of 1400°C

## 5-4 ASML compliance

As mentioned in the introduction, porosity is a key factor for the ASML application. The ASML application has pressurized channels with thin walls and must not leak. In the introduction, the assumption has been made that porosity ( $>1\%$ ) is not desired. Since the ASML application is located in a critical environment, preventing leaks is even more critical. Based on the assumptions above, a bulk porosity of 15% is unlikely to be sufficient for leak-tight applications in a vacuum environment at ASML. The mechanical properties of the copper oxide infiltration in its current state, with a flexural strength of 53.6 MPa, are insufficient for ASML applications. It is important to note that ASML employs a different method for measuring mechanical properties, specifically a 4-point bending test with a representative surface finish. Therefore, the flexural strength observed in this research might differ from ASML standards. However, it is assumed that the deviation will not be significant for this research.

A topic of interest is how strong this ceramic composite could be with the phase composition that was found in this study (see section 4-2) with a porosity that is close to 0%. In order to determine this theoretical flexural strength, an empirical relationship between flexural strength and porosity of a ceramic can be utilized to estimate the flexural strength at 0% porosity. This relationship can be found in equation 5-1 [23].

$$\sigma_0 = \frac{\sigma}{(1 - P)^n} \quad (5-1)$$

Where:

- $\sigma_0$  is the estimated flexural strength at 0% porosity.
- $\sigma$  is the flexural strength of the material at a known porosity
- $P$  is the fractional porosity (15% porosity means  $P = 0.15$ ).
- $n$  is an empirical constant

For a ceramic material,  $n$  typically ranges from 4 to 7 [14].

The worst case and best case scenario for the ceramic composite in this research, will be calculated ( $n = 4$  and  $n = 7$ ).

**For  $n = 4$ :**

$$\begin{aligned}\sigma_0 &= \frac{53.6}{(1 - 0.15)^4} \\ &\approx 103 \text{ MPa}\end{aligned}$$

**For  $n = 7$ :**

$$\begin{aligned}\sigma_0 &= \frac{53.6}{(1 - 0.15)^7} \\ &\approx 167 \text{ MPa}\end{aligned}$$

The estimated flexural strength at 0% porosity ranges between 103 MPa and 167 MPa. Comparing the lower bound of this estimate with 99.5%  $\alpha$ -alumina, which has a flexural strength of approximately 310 MPa, reveals that the theoretical strength of the composite produced in this study is only 33% of the strength of alumina [54]. Therefore, the mechanical suitability of this composite is not promising for the ASML application. No additional mechanical properties were tested. The significant deviation in strength from the desired value placed further testing out of scope.

Characteristic feature sizes are important for the suitability of ASML applications. It was not investigated whether these feature sizes could be achieved using PBBJ combined with infiltration. Although it was initially planned, the significant degradation of mechanical integrity caused by the formation of a ternary oxide made it no longer relevant. It is assumed that achieving these characteristic feature sizes depends on the mechanical integrity of the material. Since the material was mechanically inferior, further investigation into the feasibility of producing these feature sizes with PBBJ and infiltration was deemed a waste of time.

There were additional requirements that were not tested, such as fatigue, thermal properties, cleanliness, outgassing, and optical properties. However, as explained earlier, the priority was to first address the mechanical integrity of the composite before attempting to characterize these other properties.

---

## Chapter 6

---

# Conclusions

This thesis explored the pressureless infiltration of powder bed binder jetting (PBBJ) alumina with copper oxide. By combining PBBJ and pressureless infiltration, the research aimed to create high-performance ceramic composites suitable for ASML application. It focuses on understanding the relation between process parameters and the resulting composite characteristics. The conclusion is based on giving answers to research questions stated in Section 2-4.

### **What impact does the infiltration of copper oxide into porous alumina have on the chemical, mechanical, and microstructural properties of the resulting composite?**

The relative bulk density increased from 59% to 85%, indicating a 44% increase in density. This highlights the potential of liquid phase infiltration for increasing the density of porous structures fabricated by PBBJ. Approximately 50 wt.% of the alumina was consumed, during the infiltration process. This loss is a result of the reactions between copper oxide and alumina, where over 70 wt.% of the material transformed into ternary oxides. This phenomenon is a significant consideration when planning the infiltration of a porous structure with a liquid phase. It is assumed that these reactions have limited the further densification of the porous structure. The consumption of alumina prevented as well any improvement in flexural strength. Variations between the results of this research and previous studies are likely due to differences in the oxygen content of the infiltrated liquid phase (copper-oxygen melt). The oxygen level in the melt significantly impacts both the densification process and the mechanical properties of the infiltrated alumina.

### **What phase transformations occur during the thermal cycle of infiltration in nitrogen?**

As observed during infiltration in oxygen, significant reactions occur between copper oxide and alumina. To assess whether infiltration in nitrogen is a viable approach, the phase transitions in nitrogen were analyzed. The differential thermal analysis (DTA) identified five phase transformations. Among these, one critical phase transformation (peak 3) was identified, corresponding to the formation of the ternary oxide, delafossite. This peak 3 took

place in the liquid-solid state of the infiltration process and was a result of the increased reaction surface area after the wetting of alumina by copper oxide.

A strategy was developed to optimize the thermal cycle, aiming to minimize the time spent in the liquid-solid state to reduce ternary oxide formation. However, the most efficient thermal cycle in this research was still suboptimal, resulting in over 70 wt.% ternary oxide formation during the equimolar powder analysis. This 70 wt.% is still 16% less than the non-optimized thermal cycle. Further refinement of the thermal cycle is necessary to effectively limit ternary oxide formation. Other methods for reducing the formation of ternary oxides, like reducing the melting temperature of the copper oxide could be a solution as well.

### **ASML compliance**

The results of this study demonstrate that the ceramic composite produced through copper oxide infiltration with the current process parameters is not suitable for the ASML application. Improvements in the infiltration process are necessary to meet ASML's requirements.

At present, the material's high porosity of 85% renders it incapable of satisfying the leak-tight specifications. From a mechanical perspective, the composite's flexural strength of 53.6 MPa is significantly below the minimum required stress and is weaker than the current material used as the benchmark. Adjustments to the composite composition and the composition density have to be made, in order to achieve the desired requirements.

Despite these limitations, PBBJ has shown potential in fabricating medium to large-sized additive manufactured components. Furthermore, significant densification of the porous structures produced by PBBJ was achieved with the infiltration process. This makes it an intriguing area for further investigation to identify potential ASML applications.

# Recommendations

- Pressureless infiltration is a promising method for achieving high-density ceramic composites. However, copper oxide and alumina do not form a suitable composite for the current ASML application under the existing process parameters. Selecting an alternative infiltration material with suitable properties could potentially meet ASML's requirements.

Possible options are: lanthanum-based silicate glasses are suitable for infiltration into porous alumina [1, 61]. An alloy of aluminum and magnesium can be utilized for infiltration in porous alumina [50]. Infiltrating with a copper-oxygen melt containing a lower oxygen percentage could also be an interesting area of research [31].

Every new composite, having its own distinct material properties, that might suit certain ASML application areas.

- The thermal infiltration cycle could be optimized to reduce the time the system remains in the liquid-solid state. This adjustment would help prevent the formation of ternary oxides.
- The reaction rate between alumina and copper oxide increases with temperature. Therefore infiltrating copper oxide at a lower temperature could be a solution. The infiltration temperature can be lowered by doping the copper oxide, while maintaining a low contact angle on alumina [22].
- To better understand the behavior of the alumina porous structure infiltrated with copper oxide, the diffusion-controlled reaction process can be modeled for copper oxide infiltration in an alumina porous structure.

---

# Annex A

---

## Annex data results

### A-1 Powder bed binder jetting

**Table A-1:** Sample measurements of PBBJ and sintered alumina with BAK20 powder at 1550°C for 24 hours

Sample	l (mm)	w (mm)	h (mm)	volume (cm <sup>3</sup> )	mass (g)	density (g/cm <sup>3</sup> )	relative density (%)
240801 BAK20 nr 1	45.00	4.160	3.460	0.6476	1.421	2.194	55.55
240801 BAK20 nr 2	44.76	4.110	3.220	0.5924	1.341	2.264	57.31
240801 BAK20 nr 3	46.12	4.070	3.190	0.5988	1.386	2.315	58.60
240801 BAK20 nr 4	46.14	4.170	3.150	0.6061	1.412	2.330	58.98
240801 BAK20 nr 5	46.20	4.160	3.160	0.6073	1.420	2.338	59.19
240801 BAK20 nr 6	46.15	4.130	3.210	0.6118	1.409	2.303	58.30
240801 BAK20 nr 7	46.15	4.100	3.160	0.5979	1.391	2.326	58.90
240801 BAK20 nr 8	46.19	4.220	3.300	0.6432	1.456	2.264	57.30
240801 BAK20 nr 9	46.16	4.170	3.150	0.6063	1.415	2.334	59.08
240801 BAK20 nr 10	46.13	4.210	3.140	0.6098	1.432	2.348	59.45
240801 BAK20 nr 11	46.18	4.220	3.170	0.6178	1.424	2.305	58.36
<b>Mean</b>	45.94	4.150	3.199	0.6127	1.410	2.313	58.28
<b>Standard Deviation</b>	0.54	0.043	0.047	0.0171	0.033	0.047	0.99

**Table A-2:** Sample measurements of PBBJ and sintered alumina with BAK10 powder at 1550°C for 24 hours

Sample	l (mm)	w (mm)	h (mm)	Volume (cm <sup>3</sup> )	Mass (g)	Density (g/cm <sup>3</sup> )	Relative Density (%)
241025 BAK10 nr 1	46.070	4.260	3.520	0.6908	1.5988	2.3143	58.5904
241025 BAK10 nr 2	46.070	4.270	3.520	0.6925	1.5734	2.2722	57.5246
241025 BAK10 nr 3	46.060	4.270	3.320	0.6530	1.5213	2.3298	58.9831
241025 BAK10 nr 4	46.030	4.320	3.320	0.6602	1.5528	2.3521	59.5464
241025 BAK10 nr 5	46.080	4.240	3.430	0.6702	1.5704	2.3434	59.3254
241025 BAK10 nr 6	46.050	4.200	3.340	0.6460	1.5197	2.3525	59.5574
241025 BAK10 nr 7	46.090	4.350	3.370	0.6757	1.5810	2.3399	59.2392
241025 BAK10 nr 8	46.030	4.460	3.380	0.6939	1.6027	2.3097	58.4740
241025 BAK10 nr 9	46.050	4.360	3.410	0.6847	1.6269	2.3762	60.1580
241025 BAK10 nr 10	46.060	4.400	3.360	0.6810	1.5956	2.3432	59.3214
241025 BAK10 nr 11	46.040	4.280	3.370	0.6641	1.5521	2.3373	59.1716
<b>Mean</b>	46.056	4.304	3.400	0.6740	1.5740	2.3360	59.1480
<b>Standard Deviation</b>	0.019	0.076	0.070	0.0160	0.0330	0.0280	0.7000

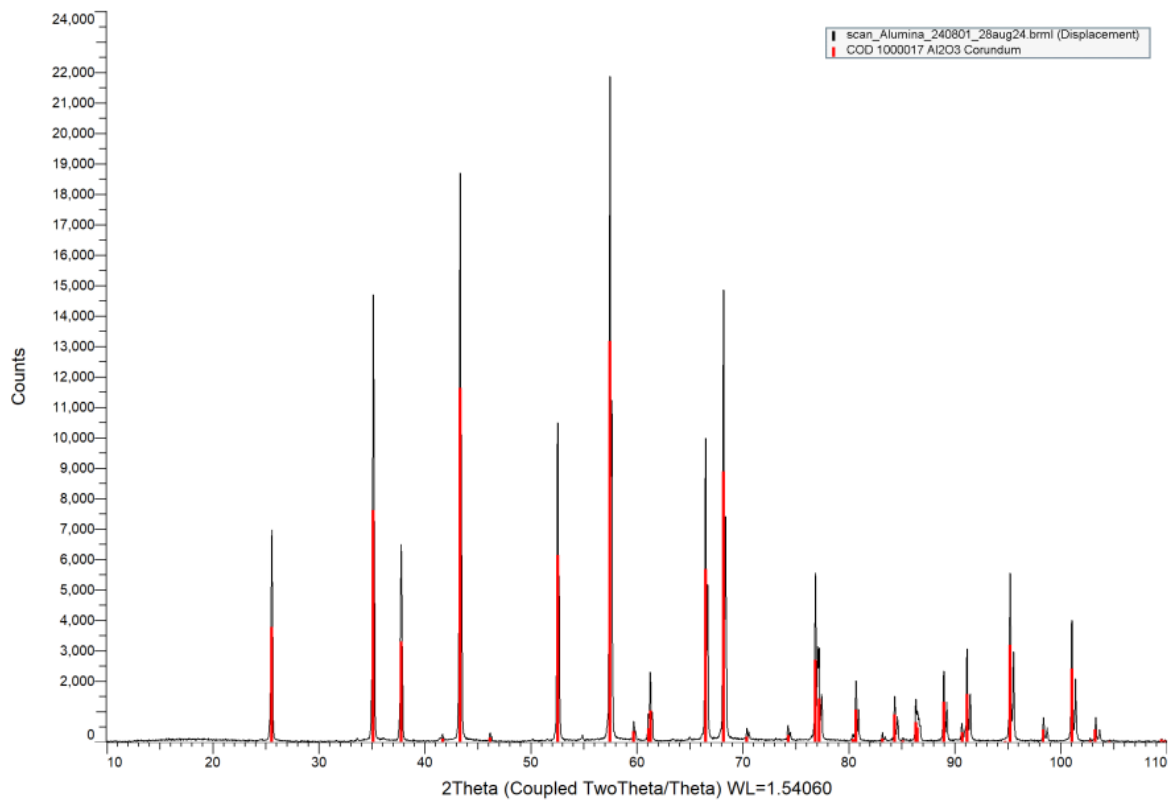


**Figure A-1:** XRD analysis of an alumina bending bar sample fabricated by PBBJ and sintered with BAK20 powder, pulverized into powder

## A-2 Infiltration in oxygen environment

**Table A-3:** Measurements of porous alumina samples fabricated using powder bed binder jetting (PBBJ) with BAK10, followed by infiltration with Cu in an oxygen-rich environment

Sample	l (mm)	w (mm)	h (mm)	volume (cm <sup>3</sup> )	mass (g)	density (g/cm <sup>3</sup> )	relative density (%)
240801 infiltratie Cu ambient @1300 1.5h #A	46.75	4.390	3.500	0.7183	2.767	3.852	84.0
240801 infiltratie Cu ambient @1300 1.5h #B	46.62	4.380	3.350	0.6841	2.628	3.842	83.6
240801 infiltratie Cu ambient @1300 1.5h #C	46.70	4.420	3.320	0.6853	2.685	3.918	85.3
240801 infiltratie Cu ambient @1300 1.5h #D	46.70	4.430	3.340	0.6910	2.702	3.910	85.1
<b>Average</b>	46.69	4.405	3.378	0.6947	2.695	3.881	84.5

**Table A-4:** Measurements of porous alumina samples fabricated using PBBJ with BAK10, followed by infiltration with Cu<sub>2</sub>O in an oxygen-rich environment

Sample	l (mm)	w (mm)	h (mm)	volume (cm <sup>3</sup> )	mass (g)	density (g/cm <sup>3</sup> )	relative density (%)
240801 infiltratie Cu2O ambient @1300 1.5h #A	46.60	4.250	3.350	0.6635	2.588	3.901	84.9
240801 infiltratie Cu2O ambient @1300 1.5h #B	46.57	4.310	3.360	0.6744	2.632	3.903	85.0
240801 infiltratie Cu2O ambient @1300 1.5h #C	46.53	4.360	3.330	0.6756	2.633	3.898	84.9
240801 infiltratie Cu2O ambient @1300 1.5h #D	46.56	4.350	3.370	0.6825	2.648	3.880	84.6
<b>Average</b>	46.57	4.318	3.353	0.6740	2.625	3.896	84.9

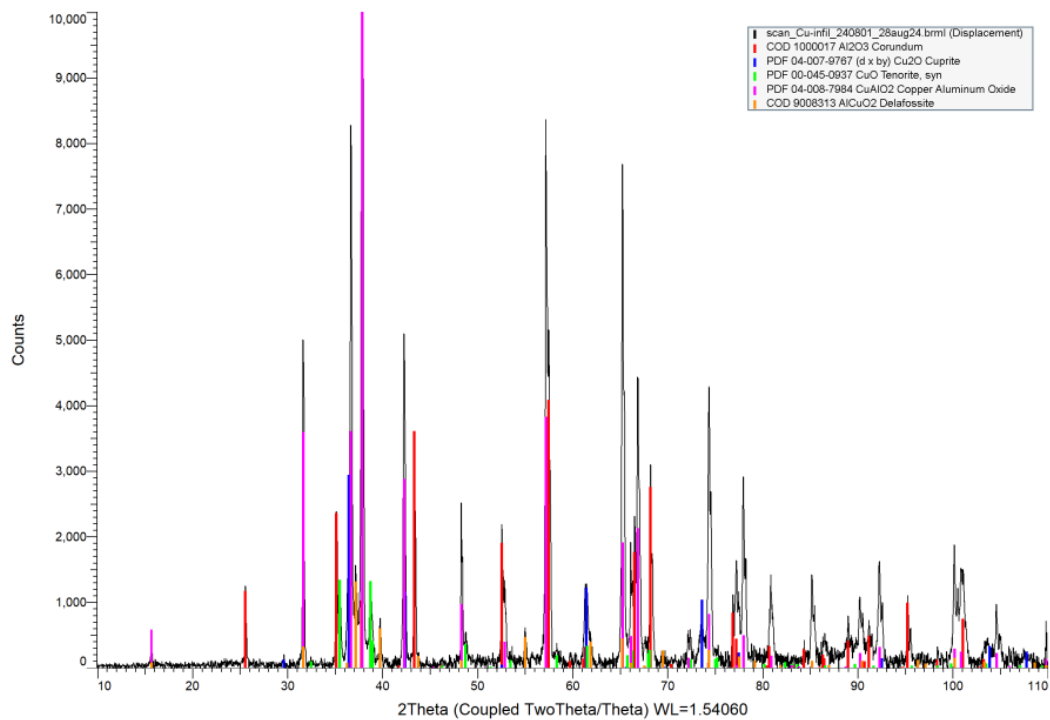


**Figure A-2:** Infiltrated sample with Cu powder in an oxygen rich environment

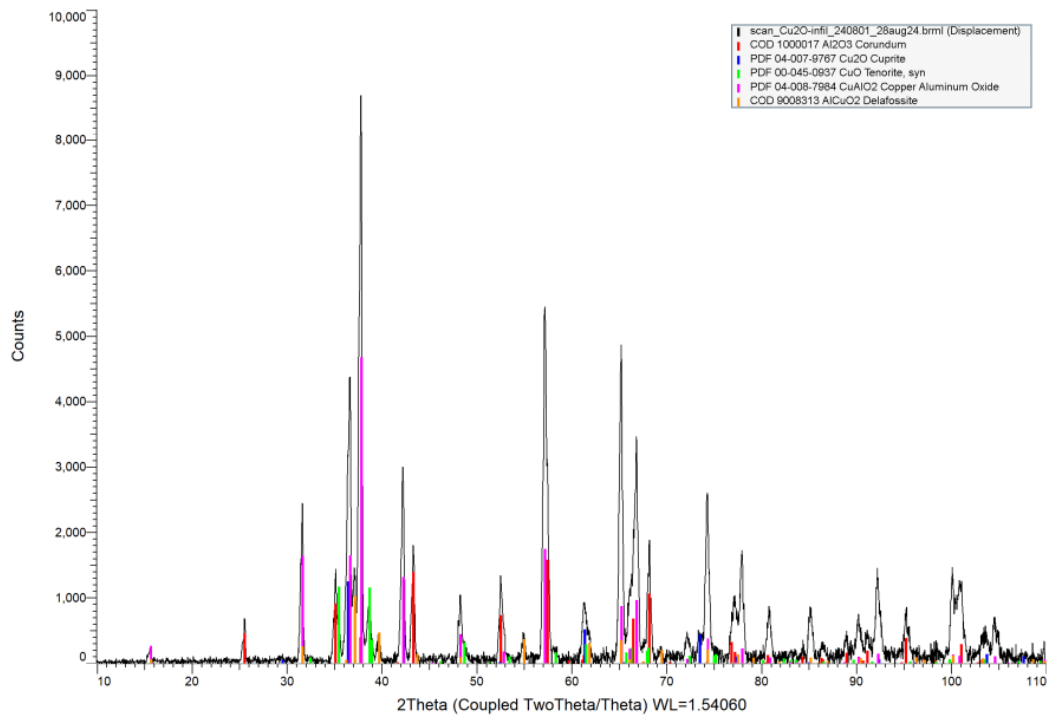


**Figure A-3:** Infiltrated sample with  $\text{Cu}_2\text{O}$  powder in an oxygen rich environment

### A-3 Infiltration in nitrogen environment

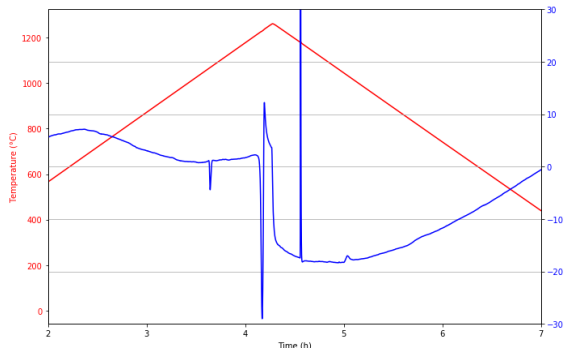


**Figure A-4:** DTA of an equimolar mixture of  $\text{Al}_2\text{O}_3$  and  $\text{Cu}_2\text{O}$ , conducted in a  $\text{N}_2$  environment with a heating rate of 5 K/min

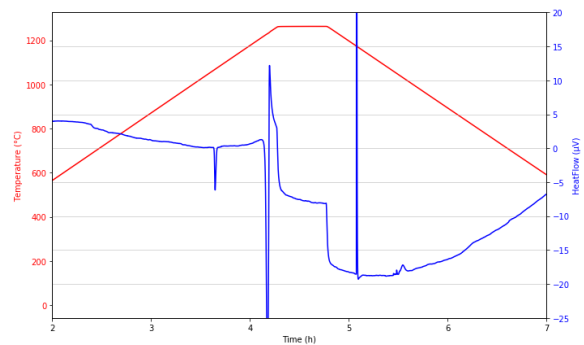


**Figure A-5:** DTA of an equimolar mixture of  $\text{Al}_2\text{O}_3$  and  $\text{Cu}_2\text{O}$ , conducted in a  $\text{N}_2$  environment with a heating rate of 5 K/min. An isotherm is reached for 30 minutes at  $1250^\circ\text{C}$

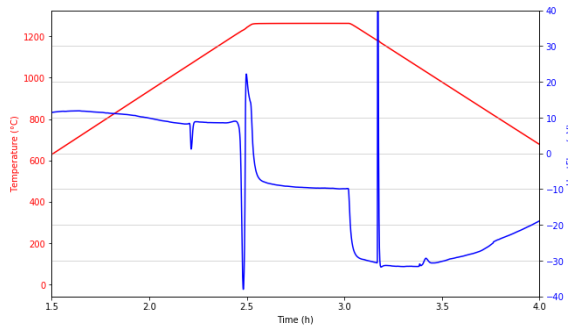


**Figure A-6:** DTA of an equimolar mixture of  $\text{Al}_2\text{O}_3$  and  $\text{Cu}_2\text{O}$ , conducted in a  $\text{N}_2$  environment with a heating rate of 10 K/min. An isotherm is reached for 30 minutes at 1250°C

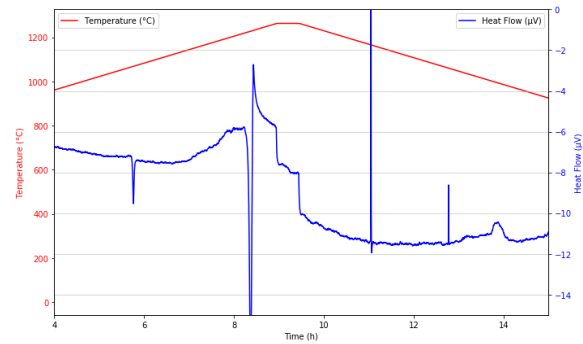


**Figure A-7:** DTA of an equimolar mixture of  $\text{Al}_2\text{O}_3$  and  $\text{Cu}_2\text{O}$ , conducted in a  $\text{N}_2$  environment with a heating rate of 1 K/min. An isotherm is reached for 30 minutes at 1250°C

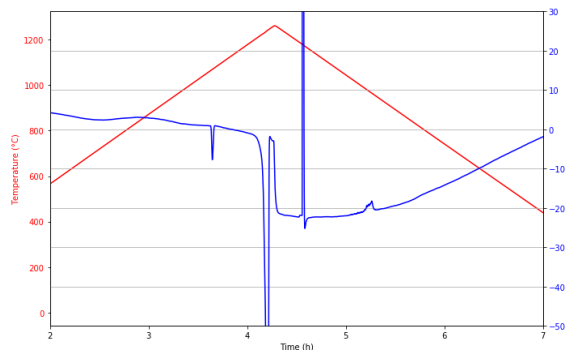


**Figure A-8:** DTA of  $\text{Cu}_2\text{O}$ -only mixture, conducted in a  $\text{N}_2$  environment with a heating rate of 5 K/min. An isotherm is reached for 30 minutes at 1250°C

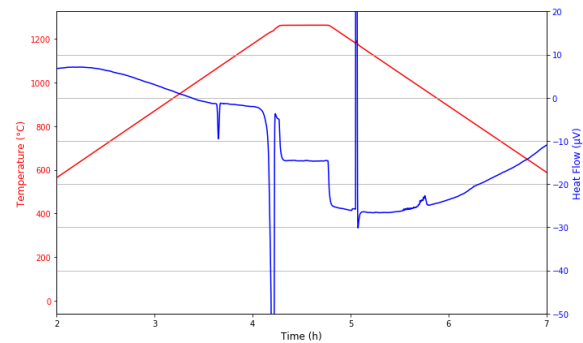


**Figure A-9:** DTA of  $\text{Cu}_2\text{O}$ -only mixture, conducted in a  $\text{N}_2$  environment with a heating rate of 5 K/min

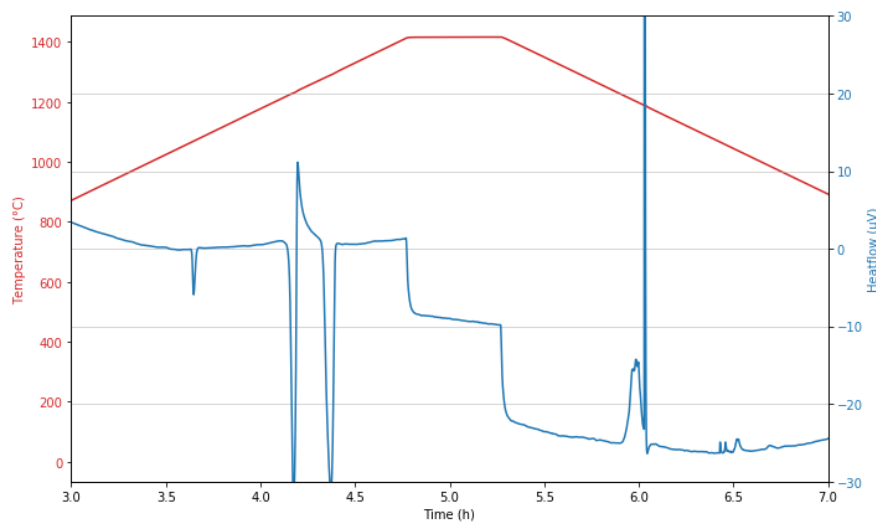


**Figure A-10:** DTA of an equimolar mixture of  $\text{Al}_2\text{O}_3$  and  $\text{Cu}_2\text{O}$ , conducted in a  $\text{N}_2$  environment with a heating rate of 1 K/min. An isotherm is reached for 30 minutes at 1400°C

Sample	Compound	Wt%
Equimolar, 5K/min, 1250 °C, 30 min isotherm	Copper Aluminum Oxide (CuAlO <sub>2</sub> )	34
	Copper (Cu)	1
	Cuprite (Cu <sub>2</sub> O)	1
	Corundum (Al <sub>2</sub> O <sub>3</sub> )	57
	Silicon (si)	7
Equimolar, 1K/min, 1250 °C, 30 min isotherm	Copper Aluminum Oxide (CuAlO <sub>2</sub> )	40
	Copper (Cu)	1
	Cuprite (Cu <sub>2</sub> O)	<1
	Corundum (Al <sub>2</sub> O <sub>3</sub> )	58
	Silicon (si)	<1
Equimolar, 10K/min, 1250 °C, 30 min isotherm	Copper Aluminum Oxide (CuAlO <sub>2</sub> )	37
	Copper (Cu)	1
	Cuprite (Cu <sub>2</sub> O)	2
	Corundum (Al <sub>2</sub> O <sub>3</sub> )	59
	Silicon (si)	<1
Equimolar, 5K/min, 1250 °C, no isotherm	Copper Aluminum Oxide (CuAlO <sub>2</sub> )	33
	Copper (Cu)	1
	Cuprite (Cu <sub>2</sub> O)	2
	Corundum (Al <sub>2</sub> O <sub>3</sub> )	63
	Silicon (si)	1
Cu <sub>2</sub> O-only, 5K /min, 1250 °C, 30 min isotherm	Copper Aluminum Oxide (CuAlO <sub>2</sub> )	6
	Copper (Cu)	3
	Cuprite (Cu <sub>2</sub> O)	9
	Corundum (Al <sub>2</sub> O <sub>3</sub> )	82
	Silicon (si)	1
Equimolar, 5K/min, 1400 °C, 30 min isotherm	Copper Aluminum Oxide (CuAlO <sub>2</sub> )	25
	Copper (Cu)	2
	Cuprite (Cu <sub>2</sub> O)	3
	Corundum (Al <sub>2</sub> O <sub>3</sub> )	68
	Silicon (si)	2

**Table A-5:** Original XRD Rietveld analyse results of the crushed alumina crucibles of the DTA tests

---

# Annex B

---

## Annex peak analysis

In this section, all the relevant peaks in the thermogravimetric analysis (TGA) and differential thermal analysis (DTA) are examined. The peaks are compared with literature and with references (like for example the Cu<sub>2</sub>O-only crucible), to assign certain peaks to reaction. This is done to get a better understanding of the phase transitions that are happening during the thermal cycle in nitrogen. The peaks and the correlated associated reactions can be found in Table B-1.

Peak	Temperature (°C)	Reaction
Peak 1	1069	0.39 wt.% Cu <sub>2</sub> O (s) + 99.61 wt.% Cu (s) → 0.39 wt.% Cu <sub>2</sub> O (l) + 99.61 wt.% Cu (l)
Peak 2	1230	Cu <sub>2</sub> O (s) → Cu <sub>2</sub> O (l)
Peak 3	1235	Cu <sub>2</sub> O (l) + Al <sub>2</sub> O <sub>3</sub> (s) → CuAlO <sub>2</sub> (s)
Peak 4	1175	CuAlO <sub>2</sub> (l) (minor phase) + Cu <sub>2</sub> O (l) (major phase) → CuAlO <sub>2</sub> (s) (minor phase) + Cu <sub>2</sub> O (s) (major phase)
Peak 5.1	1060	0.39 wt.% Cu <sub>2</sub> O (l) + 99.61 wt.% Cu (l) → 0.39 wt.% Cu <sub>2</sub> O (s) + 99.61 wt.% Cu (s)
Peak x	N/A	Instrumental effect

**Table B-1:** Summary of the DTA peaks, including their corresponding peak temperatures and associated reactions

## B-1 Thermogravimetric analysis (TGA)

A TGA test was conducted in a nitrogen environment to monitor mass changes during heating. As expected,  $\text{Cu}_2\text{O}$  does not oxidize in a nitrogen atmosphere. Consequently, the total mass loss was less than 1% of the original equimolar powder mass and is considered negligible.

In Figure 4-12, it can be seen that the TGA of the equimolar mixture and the empty crucible follow a similar pattern. Therefore, this likely indicates an instrumental effect. This instrumental effect is assumed to be the buoyancy effect. The buoyancy effect arises from changes in the density of the surrounding gas as the temperature varies. During heating, the gas density decreases, leading to a reduction in buoyant force and an apparent increase in sample mass. During cooling, the gas density increases, resulting in a greater buoyant force and an apparent decrease in sample mass [46]. Therefore, in the TGA measurement the mass increases during the heating phase and decreases during the cooling phase.

However, the behavior observed around  $330^\circ\text{C}$  remains uncertain, but several potential explanations can be considered. One possibility is the reduction of  $\text{Cu}_2\text{O}$  to  $\text{Cu}$ , which we have observed in the DTA and X-ray diffraction (XRD) (see peak 1). However, this reduction process results in an endothermic reaction [20]. No such endothermic behavior was detected in the DTA. This can be seen in figure 4-14

Another explanation could involve the combustion of residual organics or carbon-product impurities within the sample [46]. These impurities release heat as they decompose. However, latex gloves were used during the set-up of the experiment. This makes this explanation more unlikely.

Water evaporation is unlikely to be a contributing factor, as the temperature had already been held at  $200^\circ\text{C}$  during the isothermal phase. Furthermore, the observed exothermic behavior in the DTA does not align with the endothermic nature of evaporation [51].

This phenomenon remains unresolved but is not viewed as a critical factor in this study. The mass loss is less than a percent and it occurs outside the key temperature range of  $900\text{--}1250^\circ\text{C}$  and, where the formation of ternary oxides is the primary focus.

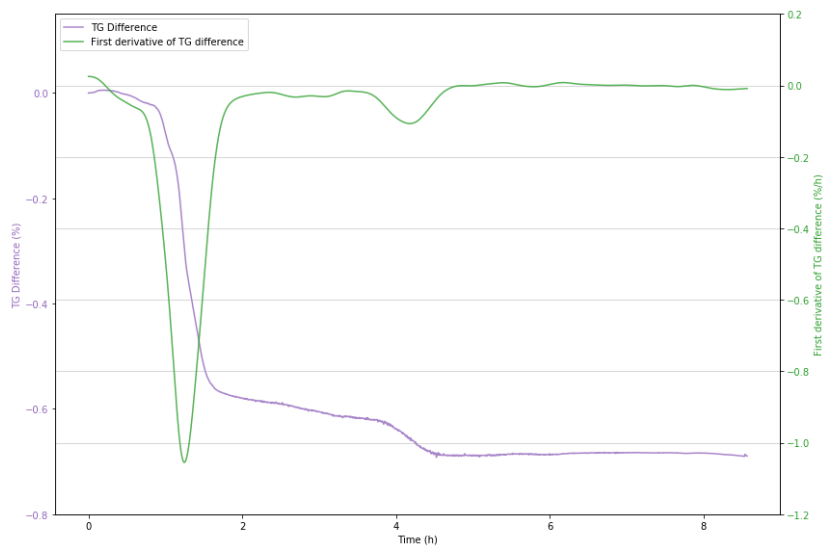


**Figure B-1:** TG Difference showing the weight change in the TGA during the same thermal cycle, comparing the empty crucible to the crucible with the equimolar powder mixture. The first derivative of the weight difference is plotted as well to highlight the points where the differences between the two TG tests are most significant

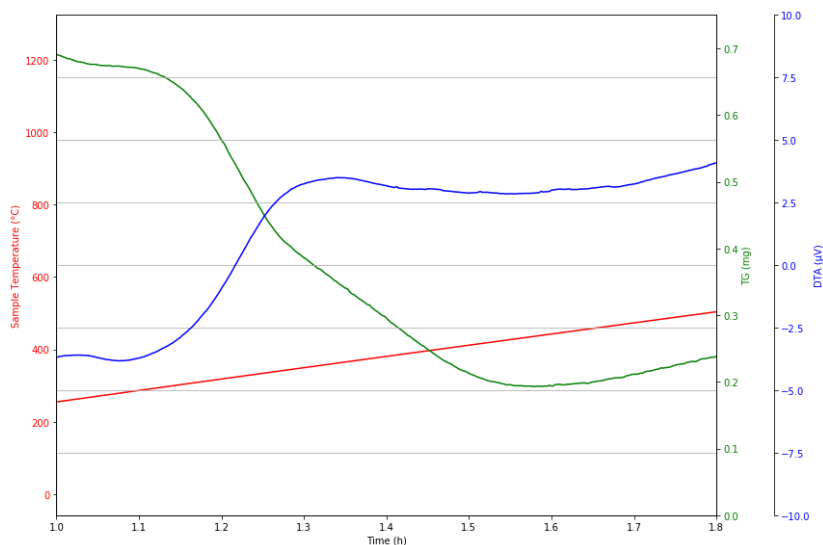


**Figure B-2:** DTA and TGA of the equimolar mixture of  $\text{Al}_2\text{O}_3$  and  $\text{Cu}_2\text{O}$  during the weight loss phenomenon in an  $\text{N}_2$  environment

## B-2 Differential thermal analysis (DTA)

In this section all the peaks are identified and connected with a certain phase transition.

### Peak 1

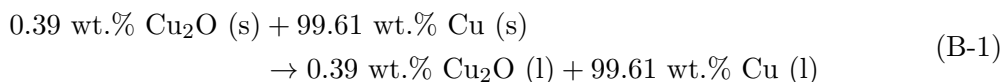
Peak 1 shows a similar heat value (within a  $\pm 10\%$  range) for both the equimolar mixture and the  $\text{Cu}_2\text{O}$ -only mixture (see the normalized values in Table 4-2). This suggests that this

phase transition is not related to the reaction between alumina and copper oxide, but instead occurs solely due to the presence of  $\text{Cu}_2\text{O}$ .

The peak temperature of Peak 1 in the DTA is approximately  $1069^\circ\text{C}$ , which corresponds to the eutectic point of the Cu-O system. The eutectic point for a Cu-O system is at  $1065^\circ\text{C}$  with a composition of 0.39 wt.%  $\text{Cu}_2\text{O}$  and 99.61 wt.% Cu [26, 58]. Therefore, Peak 1 represents the melting of copper in its metallic state with a small amount of oxygen. Initially, no metallic copper was present in the mixture. This copper is likely formed via the partial reduction of  $\text{Cu}_2\text{O}$  to copper during heating in a nitrogen atmosphere with a low oxygen partial pressure (see Figure 2-7). The low oxygen partial pressure is a result of performing the DTA in an  $\text{N}_2$  environment. The reduction of  $\text{Cu}_2\text{O}$  is confirmed by the XRD analysis (see Table 4-6), which detected a small amount of metallic copper (<5%). However, the quantification of the XRD results are assumed to be not as accurate as the mass change observed in the TGA. This mass change in the TGA was <1%.

A slight shift in the peak position is observed, likely due to differences in the sample mass of  $\text{Cu}_2\text{O}$  between the equimolar and  $\text{Cu}_2\text{O}$ -only mixtures within the DTA crucible. A larger amount of copper oxide requires more time to fully melt. This detail, considered negligible, can be seen more clearly in a close-up view of Peak 1 (Figure 4-16).

Based on the analysis above, the reaction of Peak 1 is given by equation B-1.



## Peak 2

Peak 2 is difficult to identify and quantify because it overlaps with Peak 3 in the DTA analysis of the equimolar mixture. However, since Peak 3 does not appear in the  $\text{Cu}_2\text{O}$ -only mixture, Peak 2 is easier to distinguish in the DTA of the  $\text{Cu}_2\text{O}$ -only. The peak temperature for the  $\text{Cu}_2\text{O}$ -only mixture is  $1236^\circ\text{C}$ , which matches the melting temperature of  $\text{Cu}_2\text{O}$  at  $1235^\circ\text{C}$  [33]. This temperature is also identified as the minimal wetting temperature for  $\text{Cu}_2\text{O}$ .

The heat associated with Peak 2 in the  $\text{Cu}_2\text{O}$ -only mixture is 2.4 times higher than that of the equimolar mixture. Two possible explanations are:

- Solid-state reactions may have already occurred between  $\text{Al}_2\text{O}_3$  and  $\text{Cu}_2\text{O}$ , forming  $\text{CuAlO}_2$  (delafossite). This aligns with the literature, which suggests that  $\text{CuAlO}_2$  can start forming at temperatures as low as  $900^\circ\text{C}$  (see Section 2-2-3 [3, 56, 15]). During the formation of  $\text{CuAlO}_2$ ,  $\text{Cu}_2\text{O}$  is consumed and no longer contributes to the endothermic Peak 2. Delafossite has a higher melting point of approximately  $1300^\circ\text{C}$ , so it does not contribute to the endothermic peak [45]. In this research, the melting temperature of delafossite was also determined empirically using DTA and found to be  $1280^\circ\text{C}$  (see Figure A-10).
- Overlap between Peaks 2 and 3 in the equimolar DTA analysis complicates direct comparison. Peak 3 is exothermic, which partially cancels out the heat contribution of the endothermic Peak 2. As a result, it is difficult to quantify Peak 2 for the equimolar mixture. While peak deconvolution could have clarified this, it was not performed due to time constraints.

A peak shift is observed between the equimolar mixture and the Cu<sub>2</sub>O-only mixture, which is likely caused by the overlapping peaks.

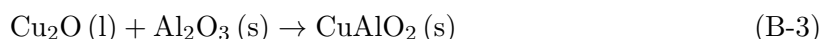
Based on the above analysis, the reaction represented by Peak 2 by equation B-2



### Peak 3

Peak 3 is hard to quantify as it overlaps with peak 2. As stated in the results (section 4-2), the exothermic peak 3 is detected in the equimolar mixture but not in the Cu<sub>2</sub>O-only mixture (See position of peak 3 marked with a green arrow Figure 4-18 and Figure 4-19). This indicates that Peak 3 is related to the reaction between the alumina and copper oxide. This hypothesis is reinforced by section 2-2-3, where it is elaborated that formation enthalpy of delafossite CuAlO<sub>2</sub> is negative, indicating that the reaction is exothermic. It is known from Peak 2 that Cu<sub>2</sub>O is in liquid state, therefore Peak 3 relates to the liquid-solid reaction.

Based on the above analysis, the reaction represented by Peak 3 is given by equation B-3



### Peak 4

Peak 4 is an exothermic peak likely associated with a solidification process. The solidification temperature, around 1180°C, is lower than the melting temperature of 1235°C (observed in Peak 2 during the heating cycle). It is unlikely that this difference is due to thermal lag caused by a temperature gradient between the oven and the sample, as the DTA with a slower heating rate also displayed a peak temperature of 1166°C (see Table 4-5). Furthermore, it is improbable that this represents the solidification temperature of delafossite (CuAlO<sub>2</sub>), as its melting temperature occurs at approximately 1280°C (see Figure A-10).

The temperature of 1180°C could correspond to a eutectic point involving the liquid phases of CuAlO<sub>2</sub> and Cu<sub>2</sub>O. According to the research by T. Ishiguro et al., a CuAlO<sub>2</sub> and Cu<sub>2</sub>O system forms a eutectic mixture [16]. However, their study states that the eutectic point is 1130°C. This eutectic point can also be seen in Figure 2-11. Several factors might explain this difference:

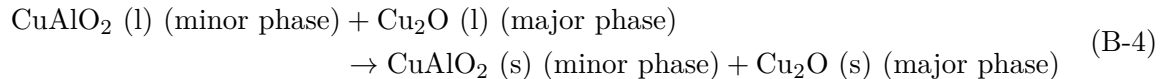
- The system in this study may include some liquid copper, altering the eutectic point and effectively transitioning it from a binary to a ternary system.
- Their measurements were conducted in an oxygen rich environment, while the environment in the DTA in this study is nitrogen.
- The measurement technique used presented in Ishiguro's study might not have been precise. Unfortunately, the details of their method could not be retrieved.

The concentrations of the presumed eutectic composition are unknown. However, it is speculated to be Cu<sub>2</sub>O-dominant. This hypothesis is supported by a comparison of the heat associated with Peak 4 in different DTA, where the heat in the Cu<sub>2</sub>O-only mixture was 4.8

times higher than in the equimolar mixture. This theory is further reinforced by the XRD results in Table 4-6, where the DTA test with the highest heat for Peak 4 correlates with the observed weight percentages in the XRD analysis.

Despite this, the precise composition of the hypothesized eutectic point remains unknown. This remains an open issue for further investigation.

Based on the above analysis, the reaction represented by Peak 4 is given by equation B-4



### Peak 5

Peak 5 actually consists of two distinct peaks. When viewed on a broader scale, they appear to overlap, but closer inspection suggests the presence of two separate events. Peak 5.1, with a peak temperature of 1060°C, is speculated to correspond to the solidification of the eutectic mixture of copper and copper oxide, as previously discussed in relation to Peak 1.

In contrast, Peak 5.2 is less sharp than Peak 5.1 and has a distinct shape. Literature suggests that during the cooling process, an exothermic crystallization of stoichiometric delafossite can occur [55]. This hypothesis is supported by evidence from one of the initial experiments in this study, where crystals were observed on the surface of the sample. This can be seen in Figure B-3.



**Figure B-3:** Preliminary experiment of copper oxide infiltration in an alumina porous body, showing crystal formation on the surface

Despite these findings, two open questions remain: why a crystallization curve was not observed for the equimolar mixture in Figure 4-21, and why an exothermic solidification peak was absent for the Cu<sub>2</sub>O-only copper-oxygen mixture in this particular equimolar mixture.

**Peak x**

Peak x is assumed to result from an instrumental effect caused by changes in the thermal cycle, such as switching from heating to cooling. In every DTA analysis (from Figure A-4 to Figure A-10), the heat flow shift occurs precisely at the thermal cycle transition. When switching from heating to cooling, the heat flow in the oven adjusts to decrease the sample's temperature. This change in heat flow is presumed to be recorded by the DTA. The hypothesis is that the DTA measurement device does not filter out this signal.

This hypothesis is further supported by the observation that the heat flow shift at Peak x increases with higher heating rates. When the heating rate is higher, the heat flow in the oven must also increase to generate a larger temperature gradient ( $\Delta T$ ), which amplifies the signal measured by the DTA. This can be seen in Figure A-6 and Figure A-7.



---

# Bibliography

- [1] Manuel F.R.P. Alves, Claudinei Santos, Caio M.F.A. Cossu, Paulo A. Suzuki, Alfeu S. Ramos, Erika C.T. Ramos, Bruno G. Simba, and Kurt Strecker. Development of dense  $\text{Al}_2\text{O}_3$ - $\text{TiO}_2$  ceramic composites by the glass-infiltration of porous substrates prepared from mechanical alloyed powders. *Ceramics International*, 2020.
- [2] Hiro Amekura, O.A. Plaksin, K. Kono, Yoshihiko Takeda, and Naoki Kishimoto. Production of  $\text{Cu}_2\text{O}$  nanoparticles in  $\text{SiO}_2$  by ion implantation and two-step annealing at different oxygen pressures. *J. Phys. D: Appl. Phys.*, 2006.
- [3] Amol P. Amrute, Zbigniew Łodziana, Cecilia Mondelli, Frank Krumeich, and Javier Pérez-Ramírez. Solid-state chemistry of cuprous delafossites: Synthesis and stability aspects. *Chemistry of Materials*, 2013.
- [4] Mehdi Arjmand, Christopher S. Knee, Henrik Leion, and Tobias Mattisson. Standard enthalpy of formation of  $\text{CuAl}_2\text{O}_4$  revisited. *Chemical Engineering Communications*, 2015.
- [5] M. Chen, B. Zhao, and E. Jak. Viscosity measurements of high “ $\text{Cu}_2\text{O}$ ” containing slags in the “ $\text{Cu}_2\text{O}$ ”- $\text{SiO}_2$ - $\text{Al}_2\text{O}_3$  system. *Pyrometallurgy Research Centre, The University of Queensland*, 2012.
- [6] Mao Chen and Baojun Zhao. Phase equilibrium studies of “ $\text{Cu}_2\text{O}$ ”- $\text{SiO}_2$ - $\text{Al}_2\text{O}_3$  system in equilibrium with metallic copper. *Journal of the American Ceramic Society*, 2013.
- [7] Antonio Contreras Cuevas, Egberto Bedolla Becerril, Melchor Salazar Martínez, and José Lemus Ruiz. Metal matrix composites - wetting and infiltration. *Springer*, 2018.
- [8] Mehran Dadkhah, Jean-Marc Tulliani, Abdollah Saboori, and Luca Iuliano. Additive manufacturing of ceramics: Advances, challenges, and outlook. *Journal of the European Ceramic Society*, 2023.
- [9] Wenchao Du, Xiaorui Ren, Z.J. Pei, and Chao Ma. Ceramic binder jetting additive manufacturing: A literature review on density. *Journal of Manufacturing Science and Engineering*, 2020.

- [10] Reihaneh Etemadi, Bo Wang, Krishna Pillai, Behzad Niroumand, Emad Omrani, and Pradeep Rohatgi. Pressure infiltration processes to synthesis metal matrix composites-a review. *Materials and Manufacturing Processes*, 2017.
- [11] N. Fries and M. Dreyer. An analytic solution of capillary rise restrained by gravity. *Journal of Colloid and Interface Science*, 2008.
- [12] Olivia Frost. Understanding additive manufacturing processes. *Freeman Technology*, 2024.
- [13] Bengt Hallstedt, Daniel Risold, and Ludwig Gauckler. Thermodynamic assessment of the copper-oxygen system. *Journal of Phase Equilibria*, 1994.
- [14] R. HAYNES. Effect of porosity content on the tensile strength of porous materials. *Powder Metallurgy*, 1971.
- [15] Wenting Hu, Felix Donat, Stuart Scott, and John Dennis. The interaction between cuo and al<sub>2</sub>o<sub>3</sub> and the reactivity of copper aluminates below 1000°C and their implication on the use of the cu-al-o system for oxygen storage and production. *RSC Adv.*, 2016.
- [16] T. Ishiguro, A. Kitazawa, N. Mizutani, and M. Kato. Single-crystal growth and crystal structure refinement of CuAlO<sub>2</sub>. *Journal of Solid State Chemistry*, 1981.
- [17] K. T. JACOB and C. B. ALCOCK. Thermodynamics of CuAlO<sub>2</sub> and CuAl<sub>2</sub>O<sub>4</sub> and phase equilibria in the system Cu<sub>2</sub>O-CuO-Al<sub>2</sub>O<sub>3</sub>. *Journal of the American Ceramic Society*, 1975.
- [18] H. Jelitto and G.A. Schneider. A geometric model for the fracture toughness of porous materials. *Acta Materialia*, 2018.
- [19] Koji Kato and Koshi Adachi. Wear of advanced ceramics. *Wear*, 2002.
- [20] Jae Y. Kim, José A. Rodriguez, Jonathan C. Hanson, Anatoly I. Frenkel, and Peter L. Lee. Reduction of CuO and Cu<sub>2</sub>O with H<sub>2</sub>: H embedding and kinetic effects in the formation of suboxides. *Journal of the American Chemical Society*, 2003.
- [21] Jin Yong Kim, John S. Hardy, and K. Scott Weil. Effects of CuO content on the wetting behavior and mechanical properties of a Ag-CuO braze for ceramic joining. *Journal of the American Ceramic Society*, 2005.
- [22] Jin Yong Kim, John S. Hardy, and Scott K. Weil. Effects of CuO content on the wetting behavior and mechanical properties of a Ag-CuO braze for ceramic joining. *Journal of the American Ceramic Society*, 2005.
- [23] F. P. Knudsen. Dependence of mechanical strength of brittle polycrystalline specimens on porosity and grain size. *Journal of the American Ceramic Society*, 1959.
- [24] Pragnya Kunchala and Keerti Kappagantula. 3d printing high density ceramics using binder jetting with nanoparticle densifiers. *Materials & Design*, 2018.
- [25] D.Y. Kwok and A.W. Neumann. Contact angle measurement and contact angle interpretation. *Advances in Colloid and Interface Science*, 1999.

- 
- [26] Shao-Kuan Lee and Wei-Hsing Tuan. Formation of  $\text{Cu}_2\text{O}$  at the  $\text{Cu}/\text{Al}_2\text{O}_3$  interface and its influence on interface strength and thermal conductivity. *International Journal of Applied Ceramic Technology*, 2013.
- [27] Sai Liu, Shanpeng li, and Jianlin Liu. Jurin’s law revisited: Exact meniscus shape and column height. *The European Physical Journal E*, 2018.
- [28] Sree Manu K M, L. Raag, Rajan T.P.D., Manoj Gupta, and Chandrasekhar Pai. Liquid metal infiltration processing of metallic composites: A critical review. *Metallurgical and Materials Transactions B*, 2016.
- [29] J.W. Martin. Composite materials. *Materials for Engineering (Third Edition)*, 2006.
- [30] R. Melcher, S. Martins, N. Travitzky, and P. Greil. Fabrication of  $\text{Al}_2\text{O}_3$ -based composites by indirect 3d-printing. *Materials Letters*, 2006.
- [31] Reinhold Melcher, Nahum Travitzky, Cordt Zollfrank, and Peter Greil. 3d printing of  $\text{Al}_2\text{O}_3/\text{Cu}-\text{O}$  interpenetrating phase composite. *Journal of Materials Science*, 2010.
- [32] Edgar Mendoza Jimenez, Daming Ding, Laisuo Su, Aparna R. Joshi, Aarti Singh, B. Reeja-Jayan, and Jack Beuth. Parametric analysis to quantify process input influence on the printed densities of binder jetted alumina ceramics. *Additive Manufacturing*, 2019.
- [33] Bruno K. Meyer, Angelika Polity, Daniel Reppin, Martin Becker, Philipp Hering, Benedikt Kramm, Peter J. Klar, Thomas Sander, Christian Reindl, Christian Heiliger, Markus Heinemann, Christian Müller, and Carsten Ronning. The physics of copper oxide ( $\text{Cu}_2\text{O}$ ). *Oxide Semiconductors (Semiconductors and Semimetals, Vol. 88)*, 2013.
- [34] Adithya Keshav Mohan. Improving performance of blades in euv lithography machines. *Master thesis, Delft University of Technology*, 2023.
- [35] C. Nexhip, R. Davidson, and S. Sun. Surface tension of  $\text{Cu}-\text{O}$  alloys at 1400 K. *VII International Conference on Molten Slags Fluxes and Salts*, 2004.
- [36] ASML Holding N.V. About asml. <https://www.asml.com/en/company/about-asml>, 2024.
- [37] Jong Mok Ok, Sangmoon Yoon, Andrew Lupini, P. Ganesh, Matthew Chisholm, and Ho Lee. Interfacial stabilization for epitaxial  $\text{Cu}_2\text{O}$  delafossites. *Scientific Reports*, 2020.
- [38] Kiran Y Paranjpe. Alpha, beta and gamma alumina as catalyst. *Pharma Innov, J*, 2017.
- [39] Kristin Persson. Materials data on  $\text{AlCuO}_2$  (sg:194) by materials project. <https://materialsproject.org/>, 2014.
- [40] Kristin Persson. Materials data on  $\text{Cu}_2\text{O}$  (sg:224) by materials project. <https://materialsproject.org/>, 2014.
- [41] Kristin Persson. Materials data on  $\text{CuO}$  (sg:131) by materials project. <https://materialsproject.org/>, 2016.

- [42] Quinton Porter, Mohammadamin Moghadasi, Zhijian Pei, and Chao Ma. Dense and strong ceramic composites via binder jetting and spontaneous infiltration. *Ceramics International*, 2023.
- [43] Andreas Prange and Heinrich Schwenke. Trace element analysis using total-reflection x-ray fluorescence spectrometry. *Advances in X-ray Analysis*, 1991.
- [44] Benny E. Raahauge and Fred S. Williams. Alumina quality, hf removal, dissolution and aluminum purity. *Smelter Grade Alumina from Bauxite: History, Best Practices, and Future Challenges*, 2022.
- [45] Chesta Ruttanapun, Wattana Kosalwat, Chalermopol Rudradawong, Phumin Jindajitawat, Prathan Buranasiri, Daengdesh Naenkieng, Narongchai Boonyopakorn, Adul Harnwungmoung, Warawoot Thowladda, Worakarn Neeyakorn, Chanchana Thanachayanont, Anek Charoenphakdee, and Aree Wichainchai. Reinvestigation thermoelectric properties of cualo2. *Energy Procedia*, 2014.
- [46] Nooshin Saadatkhah, Adrián Carillo Garcia, Sarah Ackermann, Philippe Leclerc, Mohammad Latifi, Said Samih, Gregory S. Patience, and Jamal Chaouki. Experimental methods in chemical engineering: Thermogravimetric analysis—tga. *The Canadian Journal of Chemical Engineering*, 2020.
- [47] Michael Schubert, Nico Leupold, Jörg Exner, Jaroslaw Kita, and Ralf Moos. High-temperature electrical insulation behavior of alumina films prepared at room temperature by aerosol deposition and influence of annealing process and powder impurities. *Journal of Thermal Spray Technology*, 2018.
- [48] Jaroslav Šesták and Peter Simon. Thermal analysis of micro, nano- and non-crystalline materials: Transformation, crystallization, kinetics and thermodynamics. *Thermal analysis of Micro, Nano- and Non-Crystalline Materials*, 2013.
- [49] James F. Shackelford and Robert H. Doremus. Alumina. *Ceramic and Glass Materials: Structure, Properties and Processing*, 2008.
- [50] Hassan Sharifi, Alireza Khavandi, Mehdi Divandari, and H M.I. Effect of magnesium and nickel coatings on the wetting behavior of alumina toughened zirconia by molten al-mg alloy. *International Journal of Minerals, Metallurgy, and Materials*, 2012.
- [51] G Gnanamani Simiyon and Ansha Elizabeth Mammen. A simple demonstration to show the exothermic nature of condensation and endothermic nature of evaporation. *Resonance: Journal of Science Education*, 2022.
- [52] Mukesh Kumar Singh and Annika Singh. Thermogravimetric analyzer. *Characterization of Polymers and Fibres*, 2022.
- [53] American Ceramic Society. Alumina as a ceramic material: Comp. *American Ceramic Society special publication*, 1970.
- [54] Ansys GRANTA EduPack software. Ansys, inc. *Cambridge, UK*, 2021.

- 
- [55] Dmitry Sukhomlinov, Fiseha Tesfaye, Niko Hellstén, Daniel Lindberg, and Pekka Taskinen. Thermodynamic stability of solid phases in the system cu–o–al<sub>2</sub>o<sub>3</sub> by means of the emf and dsc-tga techniques. *Journal of Solid State Electrochemistry*, 2018.
- [56] David W. Susnitzky and C. Barry Carter. The formation of copper aluminate by solid-state reaction. *Journal of Materials Research*, 1991.
- [57] N.A. Travitzky and A. Shlayen. Microstructure and mechanical properties of al<sub>2</sub>o<sub>3</sub>/cu-o composites fabricated by pressureless infiltration technique. *Department of Solid Mechanics, Materials and Structures, Tel-Aviv University*, 1997.
- [58] Kevin P. Trumble. Prediction of a critical temperature for aluminate formation in alumina/copper–oxygen eutectic bonding. *Journal of the American Ceramic Society*, 1999.
- [59] M. H. Van De Voorde. High temperature corrosion of silicon nitrides. *The Physics and Chemistry of Carbides, Nitrides and Borides*, 1990.
- [60] B. Wunderlich. Thermal analysis. *Encyclopedia of Materials: Science and Technology*, 2001.
- [61] Zhengyu Yang, Qiong Jin, Jianfeng Ma, Yiping Tong, Xiaofei Wang, Ruoxi Du, and Siqian Wang. Glass infiltration of gelcast zirconia-toughened alumina ceramics for dental restoration. *Ceramics International*, 2012.
- [62] B.V. Zhmud, F. Tiberg, and K. Hallstenson. Dynamics of capillary rise. *Journal of Colloid and Interface Science*, 2000.
- [63] Mohsen Ziaee and Nathan Crane. Binder jetting: A review of process, materials, and methods. *Additive Manufacturing*, 2019.



---

# Glossary

## List of Acronyms

<b>XRD</b>	X-ray diffraction
<b>PBBJ</b>	powder bed binder jetting
<b>SEM</b>	scanning electron microscope
<b>EDS</b>	Energy-dispersive X-ray spectroscopy
<b>TGA</b>	thermogravimetric analysis
<b>DTA</b>	differential thermal analysis
<b>EUV</b>	extreme ultraviolet
<b>BJP</b>	binder jet printer

